1. Report No. RailTEAM UNLV-1	2. Government Accession No.	3. Recipient's Catalog No.
4. Title and Subtitle Mobile 3D Printing of Rail Track Surface for Rapid Repairment		5. Report Date September 2024
		6. Performing Organization Code:
7. Author(s) Ershad Mortazavian, Arman Ali Mohammadi, Zhiyong Wang, Hualiang (Harry) Teng https://orcid.org/0000-0003-0351-4667		8. Performing Organization Report No. UNLV-1
9. Performing Organization Name and Address Department of Civil and Environmental Engineering University of Nevada, Las Vegas 4505 S. Maryland Pkwy. Las Vegas, NV 89154		10. Work Unit No. 11. Contract or Grant No. 69A3551747132
12. Sponsoring Agency Name and Address Office of Research, Development and Technology (RD&T) US Department of Transportation 1200 New Jersey Avenue, SE Washington, DC 20590		13. Type of Report and Period 14. Sponsoring Agency Code
15. Supplementary Notes		

16. Abstract

The scope of this study is to utilize metal additive manufacturing (AM) technologies to repair worn rails that are used in the U.S. railway transportation system. Submerged arc welding (SAW) and laser powder deposition (LPD) have been selected as two potential AM approaches for rail repair. Various deposition steels such as rutile E71T-1C and Lincore 40-S wire for the SAW process, and 304L stainless steel, 410L stainless steel, Stellite 6, and Stellite 21 in the powder form for the LPD process have been chosen to be deposited on the surface of the railhead. A finite element (FE) model is developed and later fine-tuned in which the thorough process of the AM rail repair is simulated through an element-birth-and-kill method and all of the involved interactions including thermal interactions, mechanical evolutions, and kinetics of phase transformation are defined and given to the model. The FE model development is simultaneously followed by similar experimental lab investigations to verify the model outcomes and hence, validate the developed FE model.

This study attempts to modify the mechanical and metallurgical properties of the repaired rail through different approaches, i.e., deposition material alteration, preheating, post heat treatment, AM method alteration, and tool path alteration. Regarding the mechanical properties, distribution of hardness and residual stresses are measured via Rockwell hardness test and X-ray diffraction (XRD) stress measurement, respectively. Evaluation of the distribution of micro-pores, micro-cracks, and metallurgical phases is carried out through scanning electron microscope (SEM), optical microscope (OM), and XRD analysis. The tensile/compressive yield and shear strength of the repaired rail are assessed via 3-point bending and tensile tests, respectively. Initial efforts are performed through experimental lab measurements, and further efforts for various deposition materials and AM process parameters are conducted through the validated FE model and numerous lab tests. One set of 3D printing configurations for heavy rail (136-lb/yd) received yield strength exceeding the AREMA standards in the lab test, and tensile strength slightly below the standards. Three sets of 3D printing configurations for light rails (75-lb/yd) obtained good results (exceeding the AREMA standards) for both yield strength and tensile strength. However, 3D printing leads to high hardness and low elongation to rails, which requires post heat treatment for property adjustment.

17. Key Words Worn rail repair, Submerged arc welding, laser powder deposition	18. Distribution Statement No restrictions. This document is available to the public through the National Technical Information Service, Springfield, VA 22161. http://www.ntis.gov		
19. Security Classif. (of this report) Unclassified	20. Security Classif. (of this page) Unclassified	21. No. of Pages 192	22. Price

Form DOT F 1700.7 (8-72) **Reproduction of completed page authorized**

USDOT Tier 1
University Transportation Center
on Improving Rail Transportation
Infrastructure Sustainability and Durability

Final Report UNLV-1

MOBILE 3D PRINTING OF RAIL TRACK SURFACE FOR RAPID REPAIRMENT

by

Arman Ali Mohammadi, Graduate Student

Ershad Mortazavian, Graduate Student,

Zhiyong Wang, Ph.D., Associate Professor
Department of Mechanical Engineering

and

Hualiang (Harry) Teng, Ph.D., Professor
Department of Civil and Environmental Engineering and Construction
University of Nevada Las Vegas

September 2024

Grant Number: 69A3551747132

DISCLAIMER

The contents of this report reflect the views of the authors, who are responsible for the facts and the accuracy of the information presented herein. This document is disseminated in the interest of information exchange. The report is funded, partially or entirely, by a grant from the U.S. Department of Transportation's University Transportation Centers Program. However, the U.S. Government assumes no liability for the contents or use thereof.

ABSTRACT

This study reports on mobile 3D printing of rail track surface for rapid repairment. The frequent replacement of worn rails on tracks brings an immense economic burden on the railroad industry, and also causes significant interruptions to railroad operation. Restoration of worn rails via additive manufacturing, i.e., 3D printing, can considerably reduce the associated maintenance costs. The scope of this study is to utilize metal additive manufacturing (AM) technologies to repair worn rails that are used in the U.S. railway transportation system (e.g. 75-lb/yd light transit rails, or 136-lb/yd heavy freight rails). More specifically, this study aims to understand the interactive mechanisms between the deposited materials and the high-carbon rail steel to identify and alleviate the effect of the associated drawbacks, i.e., residual thermal stresses, micro pores, micro cracks, and martensite nucleation, on the resulting mechanical and metallurgical properties of the repaired rail.

Submerged arc welding (SAW) and laser powder deposition (LPD) have been selected as two potential AM approaches for rail repair. Various deposition steels such as rutile E71T-1C and Lincore 40-S wire for the SAW process, and 304L stainless steel, 410L stainless steel, Stellite 6, and Stellite 21 in the powder form for the LPD process have been chosen to be deposited on the surface of the railhead.

A finite element (FE) model is developed and later fine-tuned in which the thorough process of the AM rail repair is simulated through an element-birth-and-kill method and all of the involved interactions including thermal interactions, mechanical evolutions, and kinetics of phase transformation are defined and given to the model. The FE model development is simultaneously followed by similar experimental lab investigations to verify the model outcomes and hence, validate the developed FE model.

This study attempts to modify the mechanical and metallurgical properties of the repaired rail through different approaches, i.e., deposition material alteration, preheating, post heat treatment, AM method alteration, and tool path alteration. Regarding the mechanical properties, distribution of hardness and residual stresses are measured via Rockwell hardness test and X-ray diffraction (XRD) stress measurement, respectively. Evaluation of the distribution of micro-pores, micro-cracks, and metallurgical phases is carried out through scanning electron microscope (SEM), optical microscope (OM), and XRD analysis. The tensile/compressive yield and shear strength of the repaired rail are assessed via 3-point bending and tensile tests, respectively. Initial efforts are performed through experimental lab measurements, and further efforts for various deposition materials and AM process parameters are conducted through the validated FE model and numerous lab tests.

One set of 3D printing configurations for heavy rail (136-lb/yd) received yield strength exceeding the AREMA standards in the lab test, and tensile strength slightly below the standards. Three sets of 3D printing configurations for light rails (75-lb/yd) obtained good results (exceeding the AREMA standards) for both yield strength and tensile strength. However, 3D printing leads to high hardness and low elongation to rails, which requires post heat treatment for property adjustment.

CONTENTS

LIST OF FIGURES

LIST OF TABLES

1. CHAPTER 1 INTRODUCTION

1.2. Background and Motivation

It is more than a decade that additive manufacturing (AM), i.e., 3D printing, is introduced as a viable technique for repairing damaged surfaces of metallic components [8,9]. There are various available AM methods such as submerged arc welding (SAW), gas metal arc welding (GMAW), plasma arc welding (PAW), laser powder deposition (LPD), and selective laser sintering (SLS). These AM techniques can be generally categorized into two groups: laser-based and arc-based. On one hand, there is an extensive agreement on laser-based methods because of their lower limitations regarding metallurgical consistency and a wider range of available deposition materials. On the other hand, arc-based techniques are quite popular because of their much faster scanning speed and deposition rate than the laser-based processes; which is a very important factor in case of mass production [10].

Among the available laser-based methods, while SLS is indeed practical for manufacturing metallic tools from the scratch, LPD (i.e., laser cladding) is the appropriate technique for repairing/restoring an already-manufactured steel component. In the matter of arc-based approaches, SAW has the highest quality and productivity along with the easiest applicability and is the most appropriate method for high-thickness welding [11,12].

In railroad industry, incorporation of AM for repairing worn rails has become the focal point of most of the studies attributed to railway maintenance during the recent years. This research stream was initiated by Kral et al. [13] in 2004, and ever since a growing amount of studies are investigating different aspects of this idea. Deterioration of rails typically occurs as a result of the rail-wheel interactions, resulting in detrimental damages such as wear and rolling contact fatigue [14,15]. In the following, the backgrounds of utilization of SAW and LPD as potential repair tools for repairing impaired steels are presented separately.

1.2.1. Repair via submerged arc welding (SAW)

Arc-based weld surfacing is generally an imperative process in hard-facing and cladding for the maintenance and repair of tools in order to extend their operating life under wear and corrosion conditions [16]. A compelling enhancement in wear and fatigue performance of submerged arc surfaced components is demonstrated in numerous studies. Grum et al. [17] accomplished an experimental investigation on surfacing Ni-Co-Mo alloys on a parent structural steel using SAW method. The results indicated admirable hardness and fine dendritic microstructure in the surface layers. In another study [10], they compared the SAW process with laser process for surface repairing of a maraging steel using homemade alloys as the cladding materials, where the results are compared based on the micro-structural, micro-chemical, and micro-hardness properties. Researchers in [18–22] conducted a regression analysis according to a set of lab results obtained through their tests on submerged arc surfaced metal substrates. They subsequently developed a model regarding the available regression using different methods such as neural networks and factorial design. The specified model presented a correlation between process inputs such as voltage, nozzle-to-plate distance, traveling speed, wire feed rate, and the process responses including dilution dimensions, reinforcement, and penetration. The models are viable in finding the optimum SAW process parameters for a specific surfacing application. Wang et al. [23, 24]

explored surface repair of an H13 steel via SAW technology. They used homemade flux-cored wires composed of deoxidizer and alloys along with a commercial wire. They examined the microstructure, hardness, and dry sliding wear and illustrated that the added layer has superior properties compared to the parent H13 steel.

All of the aforementioned studies are devoted to analysis of the SAW process for surface repairing of components in use in different industries like aerospace and agriculture. In railway application, Lee et al. [25] assessed the lifetime of a UIC60 rail that is protectively coated via overlay arc welding. They developed an FE model to predict residual stress distribution for different welding depths to figure out the optimum welding geometry. Jun et al. [26] conducted a consecutive analysis of failure and crack growth on an arc-weld-repaired UIC60 rail to find out the effect of residual stresses on these parameters. They also simulated the arc-weld-surfacing process using FE method in which a semi-elliptical crack was assumed to be initiated at the weld/heat-affected zone boundary in order to simulate the fatigue crack growth. Feng et al. [27] analyzed the pros and cons of on-line welding and post heat treatment of standard rails in China. In Thailand, Srikarun [28] also investigated abrasive wear performance of R260 rails that are repaired by shield metal arc welding (SMAW). Repairing of damaged surface of UIC-54 rails used in Malaysia railway network using SMAW is investigated by SaifulAkmal and Wahab [29]. A numerical model investigating the rolling contact fatigue performance and material defects of a weld-repaired rail is developed by Kabo et al. [30] in Sweden. While these featured studies are devoted to the investigation of arc welding method as a rail repair technique, any study specifically devoted to the submerged arc welding (SAW) as a potential rail repair approach is missing in the open literature. The major difference between SAW and other arc welding processes is that the coverage of the weld joint by flux particles first prevents contamination intrusion and oxidation in the final weld structure, and second minimizes the heat loss during the welding process which increases the travel speed and, subsequently, the productivity rate. It also helps increasing bonding strength between weld beads by developing a secure fusion boundary between welds. Besides, the available literature solely focused on the standard rails used in the railway networks in China, Thailand, Malaysia, and Sweden; no study has yet focused on weld-repairing American standard rails such as 75-lb ASCE and 136RE.

1.2.2. Repair via laser powder deposition (LPD)

Investigation of LPD-repairing of various impaired steel tools such as AISI-SAE 4140H [31], Fe-Mn-Si-Cr-Ni alloys [32], and CoCr1.5FeNiNb0.5 coatings [33] can be found in the open literature. Specifically speaking of industrial application of the LPD-repairing technique, Shepeleva et al. [34] presented a way to increase the wear resistance of the contact surfaces of gas turbine engine blades' shroud shelves through laser cladding. In aerospace industry, Sexton et al. [35] investigated repairing of nickel-based alloys by depositing two different deposition materials on five various substrate materials. Assessment of LPD for repairing high-strength AISI 4340 steels in aeronautical structures is undertaken by Sun et al. [36].

In railway industry, there are several studies where different aspects of LPD application for rail repair are investigated experimentally and numerically. A European project named INFRA-STAR has solely focused on European R260 rails and developed a twin-disk test setup for RCF test to evaluate the wear performance of the deposition materials [37-41]. A numerical simulation of the

twin-disk system was then conducted by Ringsberg et al. in 2005 [42] to investigate laser cladding as a potential preventative approach for R260 rails, and the results were validated based on the reported measurements by INFRA-STAR experiments. A similar experimental investigation on laser cladded R260 rails is undertaken by Clare et al. [43,44] where different candidate deposition alloys are investigated based on the output properties. Further recent studies on European R260 and R200 rails in which LPD is utilized as a preventative maintenance technique by cladding a single layer of premium steel on the rail surface to enhance its fatigue and wear life are carried out by Lewis et al. [45], Narayanan et al. [46], and Lu et al. [47]. In Korea, assessment of wear characteristics of LPD-coated KS60 Korean rails is conducted by Seo et al. [41]. They tried depositing a layer of different alloys to attain the lowest achievable wear rate. Exploration of the laser cladded U71Mn and U75V standard Chinese rails regarding their wear and fatigue characteristics is performed by Wenjian Wang et al. [49-51], Fu et al. [52], Guo et al. [53], Zhu et al. [54], Ding et al. [55], Zhao et al. [56], Xia et al. [57], and Xinlin Wang et al. [58]. Meng et al. investigated further laser-based approaches, i.e., laser-induction hybrid cladding (LIHC) [59-62] and laser dispersed quenching [63], as a replacement for the regular LPD in consideration of surface coating the U71Mn Chinese rails. They figured out that LIHC can yield to better strength and fracture properties, and is also able to eliminate sites of crack initiation and martensite nucleation in the deposited materials. An investigation on the wear and rolling contact fatigue of the C-class wheel steels and standard Chinese rails through different hardness ratio and creepages is carried out by Hu et al. [64]. Shariff et al. [65] explored the effect of laser cladding on sliding wear resistance of standard India's T-12 rail steel under two different conditions, i.e., first, laser hardening without any deposition, and second, laser melting by depositing one layer of hardened steel. Aladesanmi et al. [66] tried depositing various mixtures of Titanium ceramics and Titanium boride powders on the standard African rail surface and compared the wear and fatigue performance of different mixture ratios. The impact of different LPD process parameters and different deposition materials on the resulting mechanical, metallurgical, and tribological properties of the laser cladded standard Australian hypereutectoid rails is studied by a research group in Monash University [67-72].

Almost all studies thus far have primarily examined laser cladding as a preventative means by surface coating the railhead using a single clad layer or, at most, double clad layers. Every deposition layer has a solid-state transformation and cooling rate that is highly reliant on the bed temperature, where the bed may be the rail or the formerly deposited layer. Also, adding multiple deposition layers will induce frequent reheating cycles to the lower layers, while a single deposition layer will not experience such reheating cycle because no layer is deposited on top of it. Therefore, a thorough repairing of a worn rail by adding multiple deposition layers on the railhead is a quite different scenario from depositing one or two layers only for the preventative purposes. Although LPD is acknowledged as one of the most advanced AM processes, there is still a great chance of developing undesired microstructures and material properties through this procedure. Local solidification parameters and solid-state transformation during cooling of the deposition layers are instances of those parameters that affect the resulting microstructure and materials properties. As the deposition layers are sequentially added in a consecutive manner during LPD, forming every new layer induces a new thermal cycle to the previously deposited layers, resulting in a new solid-state transformation. Therefore, analysis of the concluding microstructure distribution and material properties of the deposited part needs a detailed consideration of the effects of LPD processing parameters and tool path on the thermal history of

every single point of the deposition layers. Hence, a comprehensive theoretical and experimental intuition of all of the involved physical interactions is necessary to optimize the process. Numerical simulation is the most affordable means to analyze the physical interactions during the LPD process and finally find the optimum parameters for a typical LPD rail repair. Development of an optimum process to repair standard U.S. rails needs a thorough assessment of mechanical and metallurgical properties of the repaired rail. Therefore, one of the major motivations of this study is to develop a validated FE model that simulates AM repairing of a rail. This model will provide a reliable backbone for further investigations on different AM process parameters to find the most optimized way for rail repair. In summary, the primary contributions of this study can be listed as follows:

- Literature review showed that all of the studies focused on surfacing the rails with a single or, at most, a couple of deposited layers majorly as a preventative approach to reduce the wear rate and increase the fatigue life of the rail rather than fully repairing the rail. As it was mentioned earlier, investigation of the mechanical and metallurgical properties of a multi-layer deposition structure is a complete different scenario than investigating a single deposition layer because of the different heat accumulation history. This is the first study that explores fully repairing a rail with multiple deposition layers.

- This is the first presented FE model as a beneficial tool for studying various process parameters to figure out the optimized condition for complete repairing of a worn rail via AM. Although Lee et al. [25] and Jun et al. [26] simulated the overlay arc welding process for protective coating of a UIC60 rail and Ringsberg et al. [42] numerically investigated the residual stress distribution in a laser-coated R260 rail with a single clad layer of Co-Cr alloy for preventative maintenance approach, i.e., not for full-repair approach, no numerical model has been developed so far aiming investigation of a fully repaired rail with multiple deposition layers added on top.

- All of the studies available in the open literature investigated the operation of LPD for repairing standard rail grades in Europe, Korea, China, India, Africa, and Australia. There is no study yet focusing on the application of AM for repairing standard rails used in the United States railway system. Therefore, this is the first study stream which focuses on repairing rail grades complying with the standards of the American associations (e.g. AREMA, ASCE, ARA, etc.).

References for Chapter 1

[1] E. Mortazavian, Z. Wang, H. Teng, Effect of heat treatment on microstructure and hardness of a worn rail repaired using laser powder deposition, Int. J. Transp. Sci. Technol. 11(2) (2022) 406-422. https://doi.org/10.1016/j.ijtst.2021.05.004.

[2] E. Mortazavian, Z. Wang, H. Teng, Finite element investigation of residual stresses during laser powder deposition process as an innovative technique to repair worn rails, Proc. Inst. Mech. Eng. F J. Rail Rapid Transit (2022). https://doi.org/10.1177/09544097221089410.

[3] E. Mortazavian, Z. Wang, H. Teng, Measurement of residual stresses in laser 3D printed train rail using X-ray diffraction technique, IMECE2021-69822 (2022) V02AT02A005. https://doi.org/10.1115/IMECE2021-69822.

[4] E. Mortazavian, Z. Wang, H. Teng, Finite element investigation of thermal-kinetic-mechanical evolutions during laser powder deposition as an innovative technique for rail repair, Int. J. Adv. Manuf. Technol. 118 (2022) 319-342. https://doi.org/10.1007/s00170-021-07873-y.

[5] E. Mortazavian, Z. Wang, H. Teng, Repair of light rail track through restoration of the worn part of the railhead using submerged arc welding process, Int. J. Adv. Manuf. Technol. 107 (2020) 3315-3332. https://doi.org/10.1007/s00170-020-05208-x.

[6] E. Mortazavian, Z. Wang, H. Teng, Thermal-kinetic-mechanical modeling of laser powder deposition process for rail repair, IMECE2019-10758 (2020) V02AT02A052. https://doi.org/10.1115/IMECE2019-10758.

[7] E. Mortazavian, Z. Wang, H. Teng, Thermal-mechanical study of 3D printing technology for rail repair, IMECE2018-86315 (2019) V002T02A052. https://doi.org/10.1115/IMECE2018-86315.

[8] A.A. Siddiqui, A.K. Dubey, Recent trends in laser cladding and surface alloying, Opt. Laser Technol. 134 (2021) 106619. https://doi.org/10.1016/j.optlastec.2020.106619.

[9] L. Zhu, P. Xue, Q. Lan, G. Meng, Y. Ren, Z. Yang, P. Xu, Z. Liu, Recent research and development status of laser cladding: A review, Opt. Laser Technol. 138 (2021) 106915. https://doi.org/10.1016/j.optlastec.2021.106915.

[10] J. Grum, J.M. Slabe, A comparison of tool–repair methods using CO2 laser surfacing and arc surfacing, Appl. Surf. Sci. 208 (2003) 424–431. https://doi.org/10.1016/S0169-4332(02)01427-7.

[11] S. Bharathi, A. Arul, M. Moshi, S.R. Sundara Bharathi, R. Rajeshkumar, R. Kumar, Factors influencing submerged arc welding on stainless steel—a review, APRN J. Eng. Appl. Sci. 11(2) (2016) ISSN: 1819-6608.

[12] P.T. Houldcroft, Submerged-arc welding, Abington Publishing (1989) UK. ISBN: 1855730022.

[13] R.F. Kral, S.A. Mayhill, M.Q. Johnson, M.E. Rovnyak, D.J. Coomer, Method of repairing a rail, US Patent (2004) US7520415B2.

[14] D.F. Cannon, K.O. Edel, S.L. Grassie, K. Sawley, Rail defects: an overview, Fatigue Fract. Eng. Mater. Struct. 26(10) (2003) 865–86. https://doi.org/10.1046/j.1460-2695.2003.00693.x.

[15] R. Masoudi Nejad, M. Shariati, K. Farhangdoost, Effect of wear on rolling contact fatigue crack growth in rails, Tribol. Int. 94 (2016) 118-125. https://doi.org/10.1016/j.triboint.2015.08.035.

[16] R.S. Parmar, Welding processes and technology, Khanna Publishers, New Delhi (2003) ISBN: 9788174091260, 8174091262.

[17] J. Grum, R. Kejžar, J.M. Slabe, Submerged arc surfacing of Ni–Co–Mo alloys similar to maraging steels on a structural steel, J. Mater. Process. Technol. 155–156 (2004) 2011–2018. https://doi.org/10.1016/J.JMATPROTEC.2004.04.214.
[18] N. Murugan, R.S. Parmar, S.K. Sud, Effect of submerged arc process variables on dilution and bead geometry in single wire surfacing, J. Mater. Process. Technol. 37(1–4) (1993) 767–780. https://doi.org/10.1016/0924-0136(93)90135-S.
[19] H.L. Tsai, Y.S. Tarng, C.M. Tseng, Optimisation of submerged arc welding process parameters in hardfacing, Int. J. Adv. Manuf. Technol. 12(6) (1996) 402–406. https://doi.org/10.1007/BF01186928.
[20] J. Grum, J.M. Slabe, The use of factorial design and response surface methodology for fast determination of optimal heat treatment conditions of different Ni–Co–Mo surfaced layers, J. Mater. Process. Technol. 155–156 (2004) 2026–2032. https://doi.org/10.1016/J.JMATPROTEC.2004.04.220.
[21] V.V. Peremitko, Wear-resistant arc surfacing over the layer of alloying charge, Pat. Weld. J. (2014). https://doi.org/10.15407/tpwj2014.08.09.
[22] V.N. Matviyenko, L.K. Leschinsky, V.A. Mazur, Heating and melting of the parent metal in submerged-arc surfacing with a composite strip electrode, Weld Int. 29(4) (2015) 291–295. https://doi.org/10.1080/09507116.2014.921375.
[23] X. Wang, J. Wang, Z. Gao, D.H. Xia, W. Hu, Fabrication of graded surfacing layer for the repair of failed H13 mandrel using submerged arc welding technology, J. Mater. Process. Technol. 262 (2018) 182–188. https://doi.org/10.1016/J.JMATPROTEC.2018.06.040.
[24] X. Wang, J. Wang, Z. Gao, D.H. Xia, W. Hu, Tempering effects on the microstructure and properties of submerged arc surfacing layers of H13 steel, J. Mater. Process. Technol. 269 (2019) 26–34. https://doi.org/10.1016/J.JMATPROTEC.2019.01.024.
[25] S.H. Lee, S.H. Kim, Y.S. Chang, H.K. Jun, Fatigue life assessment of railway rail subjected to welding residual and contact stresses, J. Mech. Sci. Technol. 28 (2014) 4483–4491. https://doi.org/10.1007/s12206-014-1016-3.
[26] H.K. Jun, J.W. Seo, I.S. Jeon, S.H. Lee, Y.S. Chang, Fracture and fatigue crack growth analyses on a weld-repaired railway rail, Eng. Fail. Anal. 59 (2016) 478–492. https://doi.org/10.1016/j.engfailanal.2015.11.014.
[27] Q. Feng, H. Song, Analysis on the operation methods of rail welding and postweld heat treatment in the track change overhaul of existing railway lines, J. Phys.: Conf. Ser. 2152 (2022) 012018. https://doi.org/10.1088/1742-6596/2152/1/012018.
[28] B. Srikarun, S. Petchsang, P. Muangjunburee, Study of abrasive wear of railway welding steel repair, grade R260, Princess of Naradhiwas University Journal 13 (1) (2021) 209–255. https://li01.tci-thaijo.org/index.php/pnujr/article/view/241123.
[29] M.N. SaifulAkmal, M.N. Wahab, Characterization of UIC-54 rail head surface welded by hardfacing using flux-cored steel wire, In: M.N. Osman Zahid et al. (eds), Recent trends in manufacturing and materials towards industry 4.0, Lecture notes in mechanical engineering (2021). https://doi.org/10.1007/978-981-15-9505-9_68.
[30] E. Kabo, A. Ekberg, M. Maglio, Rolling contact fatigue assessment of repair rail welds, Wear 436–437 (2019) 203030. https://doi.org/10.1016/j.wear.2019.203030.
[31] C. Molina, A. Araujo, K. Bell, P.F. Mendez, M. Chapetti, Fatigue life of laser additive manufacturing repaired steel component, Eng. Fract. Mech. 241 (2021) 107417. https://doi.org/10.1016/j.engfracmech.2020.107417.
[32] J. Tian, P. Xu, Q. Liu, Effects of stress-induced solid phase transformations on residual

stress in laser cladding a Fe-Mn-Si-Cr-Ni alloy coating, Mater. Des. 193 (2020) 108824. https://doi.org/10.1016/j.matdes.2020.108824.
[33] M. Ma, W. Xiong, Y. Lian, D. Han, C. Zhao, J. Zhang, Modeling and optimization for laser cladding via multi-objective quantum-behaved particle swarm optimization algorithm, Surf. Coat. Technol. 381 (2020) 125129. https://doi.org/10.1016/j.surfcoat.2019.125129.
[34] L. Shepeleva, B. Medres, W.D. Kaplan, M. Bamberger, A. Weisheit, Laser cladding of turbine blades, Surf. Coat. Technol. 125 (2000) 45–48. https://doi.org/10.1016/S0257-8972(99)00603-9.
[35] L. Sexton, S. Lavin, G. Byrne, A. Kennedy, Laser cladding of aerospace materials, J. Mater. Process. Technol. 122(1) (2002) 63–68. https://doi.org/10.1016/S0924-0136(01)01121-9.
[36] S.D. Sun, Q. Liu, M. Brandt, V. Luzin, R. Cottam, M. Janardhana, G. Clark, Effect of laser clad repair on the fatigue behaviour of ultra-high strength aisi 4340 steel, Mater. Sci. Eng. A 606 (2014) 46–57. https://doi.org/10.1016/j.msea.2014.03.077.
[37] E.J.M. Hiensch, F.J. Franklin, J.C.O. Nielsen, J.W. Ringsberg, G.J. Weeda, A. Kapoor, B.L. Josefson, Prevention of RCF damage in curved track through development of the INFRA-STAR two-material rail, Fatigue Fract. Eng. Mater. Struct. 26(10) (2003) 1007–1017. https://doi.org/10.1046/j.1460-2695.2003.00663.x.
[38] F.J. Franklin, G.J. Weeda, A. Kapoor, E.J.M. Hiensch, Rolling contact fatigue and wear behaviour of the Infrastar two-material rail, Wear 258(7–8) (2005) 1048–1054. https://doi.org/10.1016/J.Wear.2004.03.054.
[39] M. Hiensch, P.O. Larsson, O. Nilsson, D. Levy, A. Kapoor, F. Franklin, J. Nielsen, J.W. Ringsberg, J.B. Lennart, Two-material rail development: field test results regarding rolling contact fatigue and squeal noise behavior, Wear 258(7–8) (2005) 964–972. https://doi.org/10.1016/J.Wear2004.03.067.
[40] S.R. Lewis, R. Lewis, D.I. Fletcher, Assessment of laser cladding as an option for repairing/enhancing rails, Wear 330–31 (2015) 581–591. https://doi.org/10.1016/J.WEAR.2015.02.027.
[41] S.R. Lewis, S. Fretwell-Smith, P.S. Goodwin, L. Smith, R. Lewis, M. Aslam, D.I. Fletcher, K. Murray, R. Lambert, Improving rail wear and RCF performance using laser cladding, Wear 366–367 (2016) 268–278. https://doi.org/10.1016/J.Wear.2016.05.011.
[42] J.W. Ringsberg, A. Skyttebol, B.L. Josefson, Investigation of the rolling contact fatigue resistance of laser cladded twin-disc specimens: FE simulation of laser cladding, grinding and a twin-disc test, Int. J. Fatigue 27(6) (2005) 702–714. https://doi.org/10.1016/J.IJFATIGUE.2004.10.006.
[43] A.T. Clare, O. Oyelola, J. Folkes, P.K. Farayibi, Laser cladding for railway repair and preventative maintenance, J. Laser Appl. 24(3) (2012) 032004. https://doi.org/10.2351/1.4710578.
[44] A.T. Clare, O. Oyelola, T.E. Abioye, P.K. Farayibi, Laser cladding of rail steel with Co–Cr, Surf. Eng. 29(10) (2013) 731–736. https://doi.org/10.1179/1743294412Y.0000000075.
[45] S.R. Lewis, R. Lewis, P.S. Goodwin, S. Fretwell-Smith, D.I. Fletcher, K. Murray, J. Jaiswal, Full-scale testing of laser clad railway track; case study – testing for wear, bend fatigue and insulated block joint lipping integrity, Wear 376–377 (2017) 1930–1937. https://doi.org/10.1016/j.wear.2017.02.023.
[46] A. Narayanan, M. Mostafavi, T. Pirling, S. Kabra, S.R. Lewis, M.J. Pavier, M.J. Peel, Residual stress in laser cladded rail, Tribol. Int. 140 (2019) 105844.

https://doi.org/10.1016/j.triboint.2019.105844.
[47] P. Lu, S.R. Lewis, S. Fretwell-Smith, D.L. Engelberg, D.I. Fletcher, R. Lewis, Laser cladding of rail; the effects of depositing material on lower rail grades, Wear 438–439 (2019) 203045. https://doi.org/10.1016/j.wear.2019.203045.
[48] J.W. Seo, J.C. Kim, S.J. Kwon, H.K. Jun, Effects of laser cladding for repairing and improving wear of rails, Int. J. Prec. Eng. Manuf. 20 (2019) 1207–1217. https://doi.org/10.1007/s12541-019-00115-y.
[49] W.J. Wang, J. Hu, J. Guo, Q.Y. Liu, M.H. Zhu, Effect of laser cladding on wear and damage behaviors of heavy-haul wheel/rail materials, Wear 311(1–2) (2014) 130–136. https://doi.org/10.1016/J.WEAR.2014.01.011.
[50] W.J. Wang, Z.K. Fu, J. Guo, Y.Q. Zhang, Q.Y. Liu, M.H. Zhu, Investigation on wear resistance and fatigue damage of laser cladding coating on wheel and rail materials under the oil lubrication condition, Tribol. Trans. 59(5) (2016) 810–817. https://doi.org/10.1080/10402004.2015.1107926.
[51] W.J. Wang, R. Lewis, B. Yang, L.C. Guo, Q.Y. Liu, M.H. Zhu, Wear and damage transitions of wheel and rail materials under various contact conditions, Wear 362–363 (2016) 146–152. https://doi.org/10.1016/J.Wear.2016.05.021.
[52] Z.K. Fu, H.H. Ding, W.J. Wang, Q.Y. Liu, J. Guo, M.H. Zhu, Investigation on microstructure and wear characteristic of laser cladding Fe-based alloy on wheel/rail materials, Wear 330–331 (2015) 592–599. https://doi.org/10.1016/J.Wear.2015.02.053.
[53] H. Guo, Q. Wang, W.J. Wang, J. Guo, Q. Liu, M. Zhu, Investigation on wear and damage performance of laser cladding co-based alloy on single wheel or rail material, Wear 328–329 (2015) 329–337. https://doi.org/10.1016/j.wear.2015.03.002.
[54] Y. Zhu, Y. Yang, X. Mu, W.J. Wang, Z. Yao, H. Yang, Study on wear and rcf performance of repaired damage railway wheels: assessing laser cladding to repair local defects on wheels, Wear 430–431 (2019) 126–136. https://doi.org/10.1016/j.wear.2019.04.028.
[55] H. Ding, J. Dai, T. Dai, Y. Sun, T. Lu, M. Li, X. Jia, D. Huang, Effect of preheating/post-isothermal treatment temperature on microstructures and properties of cladding on U75V rail prepared by plasma cladding method, Surf. Coat. Technol. 399 (2020) 126122. https://doi.org/10.1016/j.surfcoat.2020.126122.
[56] J. Zhao, H. Miao, Q. Kan, P. Fu, L. Ding, G. Kang, P. Wang, Numerical investigation on the rolling contact wear and fatigue of laser dispersed quenched U71Mn rail, Int. J. Fatigue 143 (2021) 106010. https://doi.org/10.1016/j.ijfatigue.2020.106010.
[57] Z. Xia, L. Chen, S. Huang, J. Xu, L. Wang, S. Zhang, Effect of solid and annular laser heat sources on thermal cycle and solid phase transformation in rail steel manufactured by laser directed energy deposition, J. Laser Appl. 33 (2021) 012049. https://doi.org/10.2351/7.0000253.
[58] X. Wang, L. Lei, H. Yu, A review on microstructural features and mechanical properties of wheels/rails cladded by laser cladding, Micromachines 12(2) (2021) 152. https://doi.org/10.3390/mi12020152.
[59] L. Meng, W. Zhao, K. Hou, D. Kou, Z. Yuan, X. Zhang, J. Xu, Q. Hu, D. Wang, X. Zeng, A comparison of microstructure and mechanical properties of laser cladding and laser-induction hybrid cladding coatings on full-scale rail, Mater. Sci. Eng. A 748 (2019) 1–15. https://doi.org/10.1016/j.msea.2019.01.068.
[60] L. Meng, X. Zeng, K. Hou, Q. Hu, D. Wang, Effect of laser cladding and laser-induction hybrid cladding coatings on the bending properties and fracture behavior of rails, Surf.

Coat. Technol. 374 (2019) 1038–1050. https://doi.org/10.1016/j.surfcoat.2019.06.051.
[61] L. Meng, B. Zhu, Q. Hu, X. Zeng, D. Wang, Laser-induction hybrid cladding of different coatings on rail surface: Microstructure, wear properties and contact fatigue behaviors, Appl. Surf. Sci. 566 (2021) 150678. https://doi.org/10.1016/j.apsusc.2021.150678.
[62] L. Meng, B. Zhu, R. Yan, X. Zeng, Q. Hu, D. Wang, Effect of induction post-heating temperature on the morphology, microstructure and mechanical performance of the heat affected zone in laser-induction hybrid cladding of full-scale rail, J. Mater. Res. Technol. 13 (2021) 1431-1440. https://doi.org/10.1016/j.jmrt.2021.05.053.
[63] L. Meng, C. Xian, B. Zhu, R. Yan, Q. Hu, X. Zeng, D. Wang, Comparison on the microstructure, bending properties and tribological behaviors of rail materials treated by laser dispersed quenching and induction assisted laser dispersed quenching, Surf. Coat. Technol. 410 (2021) 126936. https://doi.org/10.1016/j.surfcoat.2021.126936.
[64] Y. Hu, L. Zhou, H.H. Ding, G.X. Tan, R. Lewis, Q.Y. Liu, J. Guo, W.J. Wang, Investigation on wear and rolling contact fatigue of wheel-rail materials under various wheel/rail hardness ratio and creepage conditions, Tribol. Int. 143 (2020) 106091. https://doi.org/10.1016/j.triboint.2019.106091.
[65] S.M. Shariff, T.K. Pal, G. Padmanabham, S.V. Joshi, Sliding wear behaviour of laser surface modified pearlitic rail steel, Surf. Eng. 26(3) (2010) 199–208. https://doi.org/10.1179/174329409X455458.
[66] V.I. Aladesanmi, O.S. Fatoba, E.T. Akinlabi, Laser cladded Ti + TiB2 on steel rail microstructural effect, Proc. Manuf. 33 (2019) 709-716. https://doi.org/10.1016/j.promfg.2019.04.089.
[67] Q. Lai, R. Abrahams, W. Yan, C. Qiu, P. Mutton, A. Paradowska, M. Soodi, Investigation of a novel functionally graded material for the repair of premium hypereutectoid rails using laser cladding technology, Compos. Part B Eng. 130 (2017) 174–191. https://doi.org/10.1016/j.compositesb.2017.07.089.
[68] Q. Lai, R. Abrahams, W. Yan, C. Qiu, P. Mutton, A. Paradowska, X. Fang, M. Soodi, X. Wu, Effects of preheating and carbon dilution on material characteristics of laser-cladded hypereutectoid rail steels, Mater. Sci. Eng. A 712 (2018) 548–563. https://doi.org/10.1016/J.MSEA.2017.12.003.
[69] T. Roy, Q. Lai, R. Abrahams, P. Mutton, A. Paradowska, M. Soodi, W. Yan, Effect of deposition material and heat treatment on wear and rolling contact fatigue of laser cladded rails, Wear 412–413 (2018) 69–81. https://doi.org/10.1016/J.WEAR.2018.07.001.
[70] Q. Lai, R. Abrahams, W. Yan, C. Qiu, P. Mutton, A. Paradowska, M. Soodi, X. Wu, Influences of depositing materials, processing parameters and heating conditions on material characteristics of laser-cladded hypereutectoid rails, J. Mater. Process. Technol. 263 (2019) 1–20. https://doi.org/10.1016/j.jmatprotec.2018.07.035.
[71] T. Roy, R. Abrahams, A. Paradowska, Q. Lai, P. Mutton, M. Soodi, P. Fasihi, W. Yan, Evaluation of the mechanical properties of laser cladded hypereutectoid steel rails, Wear 432–433 (2019) 202930. https://doi.org/10.1016/j.wear.2019.202930.
[72] T. Roy, A. Paradowska, R. Abrahams, M. Law, P. Mutton, M. Soodi, W. Yan, Residual stress in laser cladded heavy-haul rails investigated by neutron diffraction, J. Mater. Process. Technol. 278 (2020) 116511. https://doi.org/10.1016/j.jmatprotec.2019.116511.

2. CHAPTER 2 MATERIALS AND EXPERIMENTAL METHODS

As it was mentioned earlier, two AM processes are employed in this research for rail repair purposes: SAW and LPD. However, due to the inconsistency in numerous involved parameters such as scanning speed, wire/powder feeding rate, deposition materials, temperature, cooling rate, tool path, etc. neither SAW nor LPD will deliver a consistent and desired microstructural and mechanical properties to the repaired rail.

This study aims to achieve a repaired rail with the most desired mechanical and microstructural properties through modifying the SAW/LPD-repair process parameters and also conducting some pre- and post-processes on the rail.

The under-investigation properties for evaluation of the repaired rail are hardness, flexural tensile/compressive strength, yield strength, tensile strength, residual stress, microstructural phase distribution, and distribution of micropores and microcracks. There are four case studies to explore: SAW-repaired light rail (i.e., 75-lb/yd rail), SAW-repaired heavy rail (i.e., 136-lb/yd rail), LPD-repaired light rail, and LPD-repaired heavy rail. Fig. 1 shows photos of the typical worn and repaired light/heavy rails.

In the following, Sec. 2.1 presents materials composition of each of the light and heavy rails and also the utilized deposition materials for each of the SAW and LPD processes. Summarized descriptions about the SAW and LPD processes along with the incorporated tool path are given in Sec. 2.2. Regarding sample preparation and different experimental test methods, Sec. 2.3 provides detailed explanation.

(a)

(b)

(c) (d)

Fig. 2.1 (a) worn light rail, (b) repaired light rail, (c) worn heavy rail, and (d) repaired heavy rail.

2.1. Materials

2.1.1. Rail

For light rail case study, a 75-lb/yd worn rail having both the tangential and side wear is used as the sample (Fig. 1a). This rail is a grade-880 C-Mn rail steel following the standards of the American Railway Engineering and Maintenance-of-way Association (AREMA) and is mostly employed for light transit systems [1]. The chemical composition of the rail substrate is determined by chemical analysis and given in Table 1. To resemble a real on-site rail-repair procedure, which is a steady-state heat flow along the continuous longitudinal direction of rail, the available length for the sample should be at least 100 mm [2]. Therefore, a 150-mm cut of the worn rail is utilized in the AM-repair process.

In case of heavy rail, the case study is a 136-lb/yd, i.e. 136RE, worn rail which is typically used in the U.S. heavy-haul railway transportation system [1]. A 150-mm cut of the worn rail, as shown in Fig. 1c, is used as the AM substrate. Based on the AREMA standards, this is an intermediate-strength, low-alloy rail steel of which the chemical composition is presented in Table 1.

The required mechanical properties of the light and heavy rails according to the AREMA standards are given in Table 2.

Table 1 Chemical composition of the to-be-repaired rail steels (wt.%).

Material	Fe	C	Cr	Mn	Si	Ni	P	S
Light rail	Bal.	0.71	-	1.04	0.21	-	0.022	0.013
Heavy rail	Bal.	0.80	0.03	0.23	0.04	0.14	0.01	0.01

Table 2 Required mechanical properties for the light and heavy rails

Material	Yield strength (MPa)	Tensile strength (MPa)	Vickers hardness number (HV)	Elongation (%)
Light rail	460	830	222	10
Heavy rail	511	980	318	10

2.1.2. Deposition

For SAW-repairing of the light rail, a rutile E71T-1C wire with a diameter of 1.2 mm is adopted. This low-alloy wire is a conventional C-Mn steel weld that has a close chemical composition to the light rail substrate, which allows a chance of a uniform microstructure of the repaired light rail. Table 3 presents the chemical composition of commercial stock material of E71T-1C steel weld wire. A composite MgO-CaF2-Al2O3-SiO2 agglomerated commercial welding flux is used for the SAW-repairing process of the light rail of which the chemical composition is presented in Table 4, entitled as Light-SAW Flux. Concerning the heavy rail, since the head of the heavy-haul rail requires a much higher hardness, strength, and frictional wear resistance, an 1/8-in Lincore 40-S hard facing submerged arc wire is utilized because of its distinguished rolling and sliding wear properties. This wire is specifically compatible for carbon steel and appropriate for depositing up to 5 layers. Table 3 gives the chemical composition of this utilized SAW wire. The neutral Lincolnweld 801 submerged arc flux is used as the recommended and compatible flux, of which the chemical composition is demonstrated in Table 4, entitled as Heavy-SAW Flux. It is also worth noting that prior to the weld process, the rusts and macro-contaminants on the railhead are removed using sandblasting, and the surface is cleaned thereafter using acetone to remove any remaining micro-contaminant. This cleaning process allows for establishing the best bonding condition.

Table 3 Chemical composition of the utilized SAW wires (wt.%).

Material	Fe	C	Cr	Mn	Si	Ni	O	N	P	S	Cu	Mo	Al	Ti
E71T-1C	Bal.	0.18	–	1.2	0.8	0.40	0.03	0.030	0.025	0.025	–	–	0.5	0.05
Lincore 40-S	Bal.	0.12	0.50	2.75	3.30	–	–	–	–	–	–	0.85	–	–

Table 4 Chemical composition of the agglomerated flux used for the SAW-repairing process (wt.%).

Flux	SiO_2	CO_2	Al_2O_3	CrO	MgO	MoO_3	CaO	CaF_2	MnO	TiO_2	Na_2O	Fe_2O_3
Light-SAW	10.7	–	17.3	–	31.7	–	6.6	24.1	1.1	0.86	0.78	1.9
Heavy-SAW	10.0	21.2	–	8.9	–	18.4	–	–	14.2	–	–	22.7

The initial try for LPD-repairing of both the light and heavy rails is conducted using 304L stainless steel deposition powder, with particle diameter of 45-104 μm, because of its high strength, high corrosion resistance, and great laser compatibility [3]. The chemical composition of 304L can be found in Table 5.

Table 5 Chemical composition of the utilized LPD steel powders (wt.%).

Material	Co	Fe	C	Cr	Mn	Mo	Si	Ni	P	S	W
304L	-	Bal.	0.03	19.0	2.00	-	1.00	10.5	0.045	0.03	-

2.2. Additive manufacturing (AM) repair mechanism

2.2.1. Submerged arc welding (SAW)

A distinctive feature of a SAW process is associated with the flux particles; they cover and shield the arc in a way that the wire and the arc are entirely submerged in flux stream. Consequently, unlike most of the common open welding processes, the SAW process is almost free of any extreme heat radiation, which leads to a pretty clean weld. The other substantial advantage of flux coverage is increasing energy transfer efficiency up to more than 90%, as it blocks any radiation loss, convection loss, or energy scattering from wire to the substrate. The specified increased efficiency contributes to a high deposition rate and a favorable weld reliability.

Fig. 2 shows a schematic form of a SAW structure. The wire as the filler material is applied to the substrate surface along with the flux grains that are flown through a hopper. As Fig. 2 shows, the arc is burnt in the covering envelop and the melt pool is solidified on the rail substrate. At the lower layer of flux particle flow, i.e., the top of the envelop, molten flux is formed that is solidified thereafter and develops a thin coating on the weld. This developed coating is called slag and has to be removed afterwards. The SAW process for rail repair in the current work is carried out with an open-circuit welding voltage of 25~36 V, welding current of approximately 150 A, wire feed rate of 21 mm/s, and a travel speed of 23 mm/s.

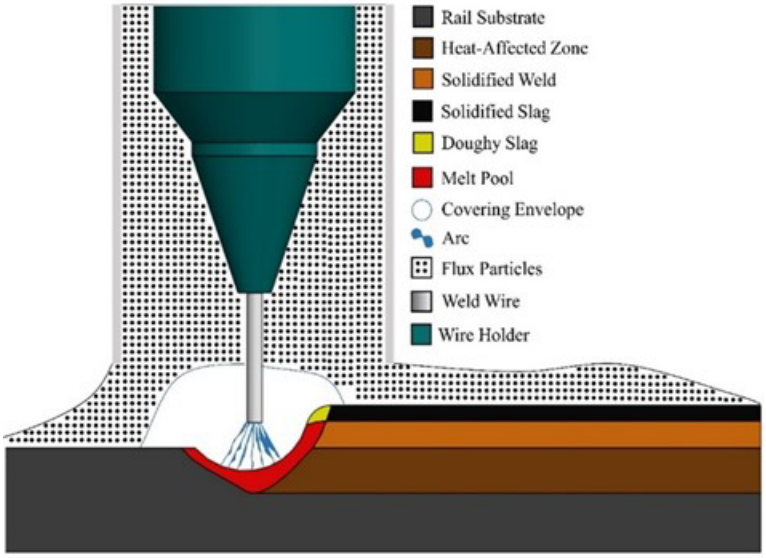

Fig. 2.2 Schematic illustration of a SAW setup.

2.2.2. Laser powder deposition (LPD)

The general function of an LPD process is to develop a melt pool on the substrate surface using laser beam and then blow the powder particles to the developed melt pool by carrier gas. The driven powder particles start to melt once they enter the laser beam threshold. There are two typical LPD setups: off-axis setup, where the powder nozzle is positioned at an angle in relation to the optical laser beam; and coaxial setup, where the powder nozzle is banded around the optical laser beam and both of them, as an integral unit, are positioned perpendicular to the substrate. In coaxial setup, the direction of deposition and tilt of the substrate will not affect the final quality, which is the prevailing advantage of coaxial setup over the off-axis [4]. Therefore, a coaxial LPD setup is used in this research (Fig. 3), which is equipped with a 5-axis computer numerical controlled (CNC) table that shifts, tilts, and rotates. The rail is clamped to the CNC table as the substrate. The coaxial nozzle has a 9 MP Metco powder feeder and a 4 kW IPG fiber laser gun. There is an 11 mm of stand-off distance between the laser beam and railhead surface, which results in a 5 mm laser strike diameter onto the surface. The other LPD parameters include 1.8 kW of laser power, 2 cm^3/min powder feeding rate, and 6 slpm flow rate of the carrier gas (Argon shielding gas).

2.2.3. Tool path

Fig. 4 gives a graphical illustration of the tool path. Due to the rail side wear, the transversal section of the rail does not represent a symmetrical geometry. Therefore, in order to carry out a flat and smooth nozzle travel during depositing every single row and consequently, to avoid continuous elevation changes, the deposition process is conducted along the longitudinal, i.e., x, direction. In the LPD process, the laser scanning speed is 1000 mm/min and the idle time between the deposition of two consecutive deposition rows is 9 s. The SAW process is carried out with an open-circuit welding voltage of 25 ~ 36 V, welding current of approximately 150 A, wire feed rate of 21 mm/s, and a travel speed of 23 mm/s. There is a 50% overlap for two adjacent deposition rows. The deposition layers are built upon one another along the +y direction. The total number of required deposition layers for a complete repair and the required duration for a full repair depend on the repairing process (SAW or LPD), rail size (light or heavy), and depth of wear. For instance, SAW-repairing of the light rail takes a total number of 6 welding layers across the entire build, with 10 to 15 welding passes per layer. LPD-repairing of a 150-mm light rail approximately takes 65 minutes, where a total number of 9 layers are deposited across the entire build. Also, each deposition layer is consisted of 15 to 20 rows. Both the LPD- and SAW-repaired heavy rails contain a total of 5 deposition layers.

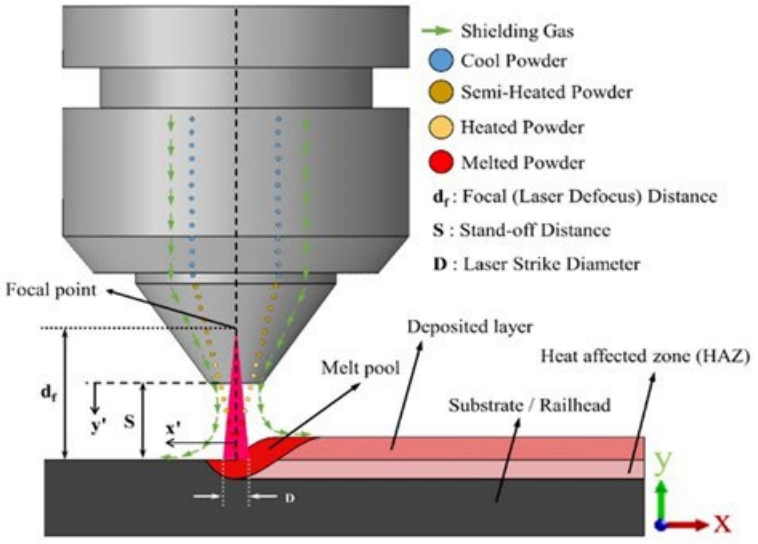

Fig. 2.3 Schematic illustration of an LPD setup.

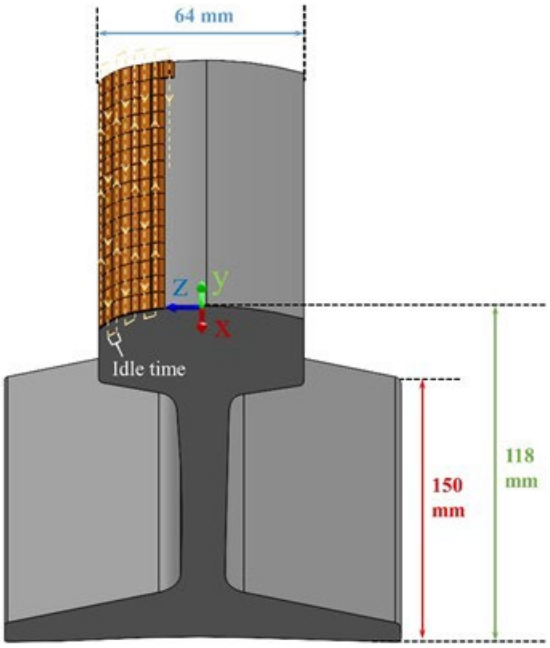

Fig. 2.4 Graphical illustration of the AM tool path. Every single layer is deposited along +/- x direction, and the layers are built upon one another along +y direction.

2.3. Sample preparation

A slice from the head of the repaired rails is used as the specimen for experimental examinations including hardness test, microstructure analysis, residual stress measurement, and flexural and shear strength evaluation. For example, Fig. 5 shows the procedure of specimen extraction from

the LPD-repaired heavy rail.

The sliced sample is first used for the hardness test. Referring to the active standards provided by ASTM E-18 [5] for a mild carbon steel, Rockwell hardness test is executed on B scale using a LECO hardness tester. On this scale, the applied minor and major indentation loads are 10 kgf and 90 kgf, respectively. In case of SAW-repaired heavy rails, where the deposited material is a high-carbon steel, C scale Rockwell hardness is carried out, for which 10 kgf and 150 kgf loads are applied as the minor and major loads, respectively.

(a) (b) (c)

Fig. 2.5 (a) the LPD-repaired rail, (b) a slice cut from the head of the repaired rail (the boundaries between deposition layers are shown as black dashed lines), and (c) the extracted specimen from the slice cut.

Afterwards, the specimen is polished to 1 μm roughness by pasting diamond on SiC papers. An HCl-based etchant, containing 100 ml HCl, 100 ml ethanol, and 5 g ethylene glycol, is used to etch the sample in order to unveil the micro grains and also to remove the externally induced residual stresses on the specimen surface as a result of the mechanical polishing. The etched specimen is then cleaned in an ultrasonic bath to get prepared for microstructure characterization. A Leica DM750 M is employed for optical microscope (OM) investigation. As a complementary to exploring the microstructure morphology, a scanning electron microscope (SEM) analysis is also performed using a JEOL 7001F FEG. An Oxford ISIS electron-dispersive X-ray spectroscopy (EDS) detector, coupled with the SEM, is utilized to analyze the chemical composition variation from welded/deposited materials to the rail substrate.

For residual stress evaluation, an X-ray diffraction (XRD) stress measurement is done by means of a Bruker D8 Discovery X-Ray diffractometer. This apparatus is equipped with a CuKα radiation source with constant wavelength of 1.5406 Å and the running parameters of 40 kV and 40 mA for X-ray tube. The sampled area is controlled through a 1-mm pinhole collimator.

Based on the study by Ghasri-Khouzani et al. [6], an X-ray beam, originated from a CuKα source and aimed to a steel surface, has an average penetration depth of 5 μm. Accordingly, to mitigate the surface roughness and to ensure that there are no surface spikes taller than 5 μm to interrupt the X-ray beams, pasted diamond suspensions on SiC papers are used to polish the specimen down to 1 μm. A thickness of 750 μm is removed from the sample surface as a result of polishing.

To remove the relaxed residual stresses on the polished sample surface as a result of cutting and polishing, the sample is etched. The typical etched sample can be seen in Fig. 5c. Each course of 30-second etching removes around 50 μm of the sample thickness. This course of etching is repeated over and over until the XRD-measured stress on the surface is stabilized, which subsequently indicates that all the externally-induced residual stresses are fully removed. The related graphs of this step of testing validation will be presented and discussed later on. The common locations where residual stress is measured using XRD are shown in Fig. 5c as numbered white spots on the etched sample, except for the spot 1 that is shown in red. Spot 1 is the location at which the stress is frequently measured at each step of sample preparation, i.e., before polishing, after polishing, and after each course of etching, to make sure that the existing factors of error, i.e., surface roughness and externally-induced residual stresses, are completely eliminated. Once the sample is etched enough that the measured stress at spot 1 is stabilized, stress at the other spots is measured.

In order to improve the hardness and microstructural properties of the repaired rails, the specimens are heat treated afterwards. A post-process quenching is performed on the SAW-repaired light rail, where a sliced etched sample is heated up to 1100°C, above the austenization temperature of the weld materials, in an FO110CR muffle furnace and soaked for 40 min to ensure homogeneous transformation across the entire specimen. The furnace is then shut off and the furnace was left open to let the red signs of heat disappear. After that, the heated sample is cooled down immediately by submerging into water and quenching to room temperature. The as-quenched (AQ) specimen was milled and polished again according to the same procedure described earlier to prepare for microstructure analysis and hardness test. In case of the LPD-repaired light rail, where 304L stainless steel is used as the deposition material, although quenching generally is recommended as the best available heat treatment method to enhance the hardness and strength properties of steel, for stainless steels the quenching should be followed by a second-step heat treatment to dissolve the grain-boundary precipitated carbides, thereby avoiding any sensitization or excessive brittleness. Accordingly, in line with the results presented by Essoussi et al. [7], the post-processing heat treatment used for the LPD-repaired light rail consists of two steps, i.e., 1) a solution treatment for 1 hour at 1150°C followed by water quenching and 2) isothermal tempering at 350°C for 30 minutes followed by cooling in still air. Therefore, the as-built specimen was placed into an FO110CR muffle furnace that was heated up to 1150°C. After 1 hour of soaking into 1150°C, the specimen was removed from the furnace and immediately quenched into the water. Then, the quenched sample was placed again into the furnace, but this time for 30 minutes long and at 350°C. It was then removed from the furnace and put outside in the still air to be cooled down naturally. Finding and conducting the most appropriate post-heat-treatment method for the repaired heavy rails is under investigation at this time.

Three-point bending test is accomplished for two sets of specimen.

The thin specimen is used to assess the static flexural tensile/compressive strength of the weld, i.e., deposited, materials. The typical location from where the thin specimen is extracted is illustrated in Fig. 6a. The dimensions of a typical thin bending sample are given in Fig. 6b, where all the dimensions are in millimeters. It is also shown in Fig. 6b that the distance between the supports for 3-point bending test is 76 mm. This distance is chosen large enough to make sure that the thin sample will fail due to bending, and not due to shear, to let us evaluate the flexural strength of the materials rather than their shear strength.

The thick specimen is for evaluating the static shear strength, i.e., bonding strength, between the rail and the deposited weld. Therefore, the thick specimen is extracted from the rail-weld interface region, as shown in Fig. 6c. The dimensions of the extracted thick specimen can be found in Fig. 6d. As it is evident in Fig. 6d, the 5-mm-thick specimen is tried to be extracted in a way that it contains almost equal fraction of the weld and rail materials, i.e., 2.5 mm thickness from the weld area and 2.5 mm thickness from the rail zone. Another visible fact in Fig. 6d is that the support distance is chosen small enough, i.e., 30 mm, to ensure that the specimen fails as a result of shear and not bending. This helps us to assess the shear strength at the rail-weld interface. More details about the effect of support distance on the failure mode are given in the results in Chapter 8.

For instantaneous and precise recording of displacements along both directions, moiré diffraction method is used. The samples are considered to fail at a 50% load drop from the maximum reached load, i.e., failure load. The failure load is used for calculating the bending strength. The fracture surfaces of the failed samples are then examined using SEM to analyze and discuss failure modes.

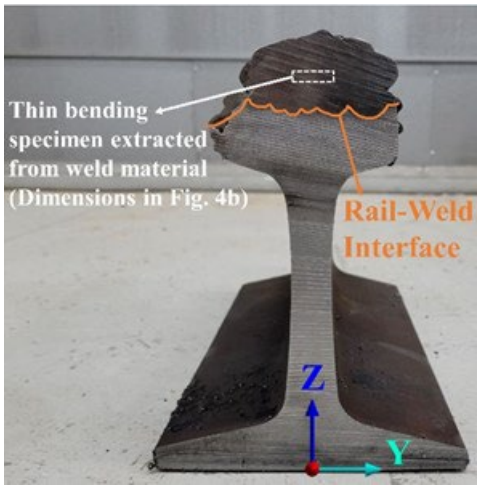

(a)

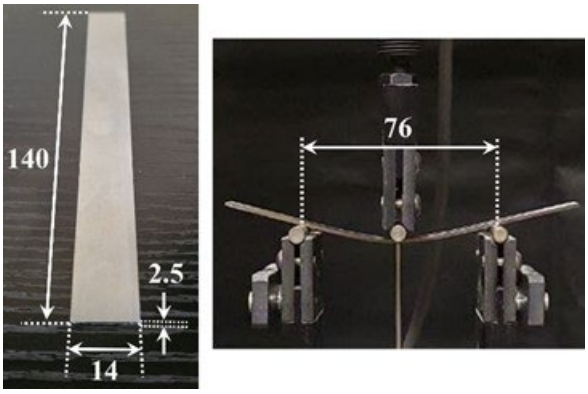

(b)

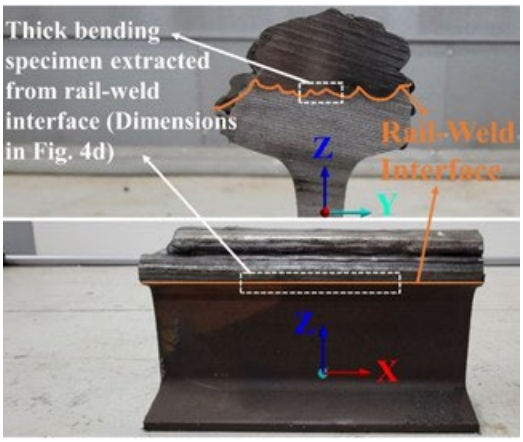

(c)

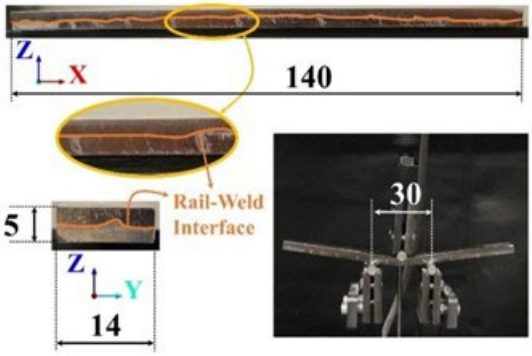

(d)

Fig. 2.6 (a) Locations of extracting thin bending specimen from weld materials for flexural tensile/compressive strength evaluation, (b) typical thin bending specimen dimensions, (c) location of extracting thick bending specimen for shear strength evaluation at the rail-weld interface, and (d) typical thick bending specimen dimensions (all dimensions are in millimeters)

References for Chapter 2

[1] M.P. Hughes-Cromwick, M. Dickens, Public Transportation Fact Book. 71st edition, American Public Transportation Association, Washington, DC (2020). https://www.apta.com/wp-content/uploads/APTA-2020-Fact-Book.pdf.

[2] Q. Lai, R. Abrahams, W. Yan, C. Qiu, P. Mutton, A. Paradowska, X. Fang, M. Soodi, X. Wu, Effects of preheating and carbon dilution on material characteristics of laser-cladded hypereutectoid rail steels, Mater. Sci. Eng. A 712 (2018) 548–563. https://doi.org/10.1016/J.MSEA.2017.12.003.

[3] X.Y. Wang, D.Y. Li, Mechanical, electrochemical and tribological properties of nanocrystalline surface of 304 stainless steel, Wear 255(7–12) (2003) 836–845. https://doi.org/10.1016/S0043-1648(03)00055-3.

[4] M. Dias da Silva, K. Partes, T. Seefeld, F. Vollertsen, Comparison of coaxial and off-axis nozzle configurations in one step process laser cladding on aluminum substratem J. Mater. Process. Technol. 212(11) (2012) 2514–2519. https://doi.org/10.1016/j.jmatprotec.2012.06.011.

[5] ASTM E18-15, Standard test methods for Rockwell hardness of metallic materials, ASTM international (2015). https://doi.org/10.1520/E0018-15.

[6] M. Ghasri-Khouzani, H. Peng, R. Rogge, R. Attardo, P. Ostiguy, J. Neidig, R. Billo, D. Hoelzle, M.R. Shankar, Experimental measurement of residual stress and distortion in additively manufactured stainless steel components with various dimensions, Mater. Sci. Eng. A 707 (2017) 689-700. https://doi.org/10.1016/j.msea.2017.09.108.

[7] H. Essoussi, S. Elmouhri, S. Ettaqi, E. Essadiqi, Heat treatment effect on mechanical properties of AISI 304 austenitic stainless steel, Proc. Manuf. 32 (2019) 883–888. https://doi.org/10.1016/j.promfg.2019.02.298.

3. CHAPTER 3 MICROSTRUCTURAL ANALYSIS OF THE REPAIRED RAIL

3.1. Light rail

3.1.1. SAW-repaired light rail

Fig. 1 illustrates optical microscope (OM) micrographs of the cross section of the as-built (AB) metallographic specimen extracted from the SAW-repaired heavy rail. The sample extraction procedure was fully described in Sec. 2.3. According to Fig. 1a, the SAW-repaired specimen is partitioned into three zones: (1) weld zone (WZ), which represents the added weld materials on top of the railhead; (2) heat-affected zone (HAZ), the fusion zone connecting WZ to the rail; and (3) rail zone that is the worn rail substrate. The WZ, as shown in Fig. 1b, is subdivided into three zones with varying microstructure distribution along the depth of the WZ cross section. Fig. 1c corresponds to the WZ1—the top portion of the WZ; WZ2 is the middle portion of the WZ that is illustrated in Fig. 1d, and Fig. 1e shows WZ3—the lower part of the WZ that is adjacent to the HAZ. The OM micrographs of the HAZ and rail are also presented in Figs. 1f and 1g, respectively. Figs. 1h and 1i stand for the WZ/HAZ and the HAZ/rail fusion boundary, respectively, where the mentioned fusion boundary is shown in dashed red line. Subsequently, scanning electron microscope (SEM) micrographs of WZ1, WZ2, WZ3, HAZ, and rail are given in Figs. 2c to 2g, respectively. Table 1 lists chemical composition of different zones of the AB specimen.

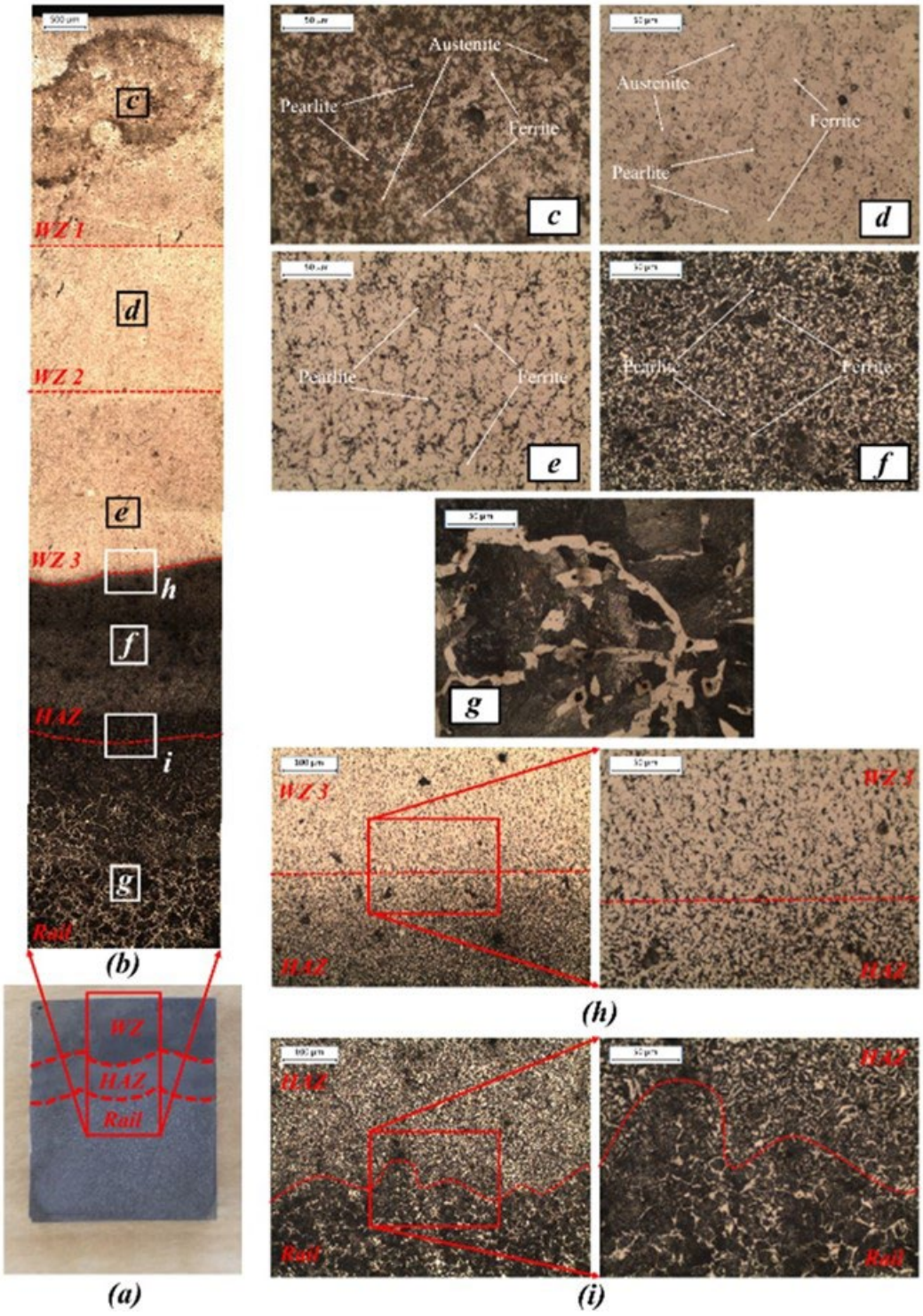

Fig. 3.1 (a) a chopped piece from the metallographic as-built (AB) specimen; (b) Optical macrograph covering weld zone (WZ), heat-affected zone (HAZ), and rail zone; OM micrographs of (c) WZ1, (d) WZ2, (e) WZ3, (f) HAZ, (g) rail, (h) WZ/HAZ fusion boundary, and (i) HAZ/rail fusion boundary are also illustrated.

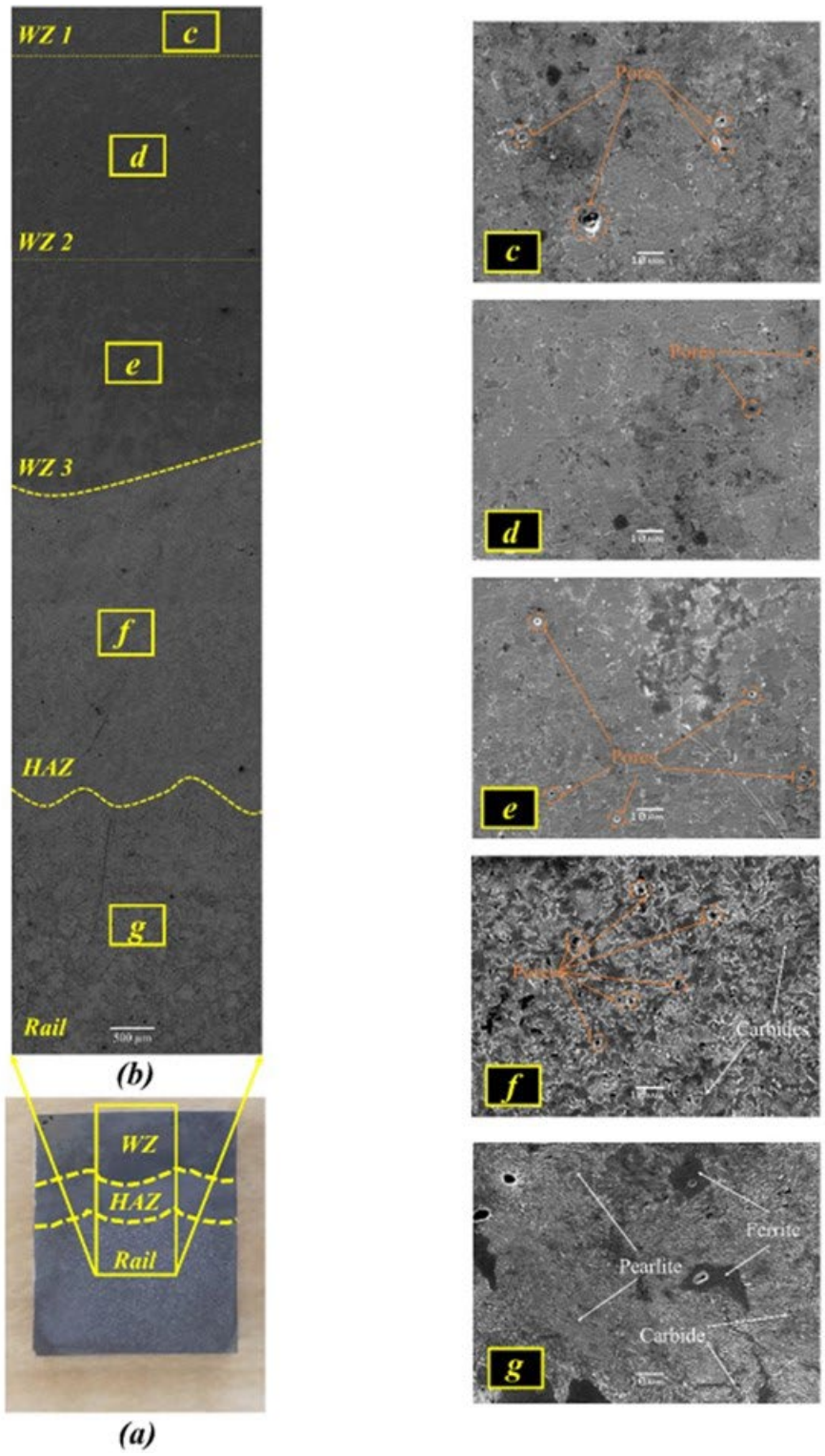

Fig. 3.2 (a) a chopped piece from the metallographic specimen of the as-built (AB) specimen; (b) Optical macrograph covering weld zone (WZ), heat-affected zone (HAZ), and rail zone; SEM micrographs of (c) WZ1, (d) WZ2, (e) WZ3, (f) HAZ, and (g) rail are also illustrated.

Table 6 Chemical composition of different zones of the as-built (AB) SAW-repaired light rail specimen (wt.%).

Zone	Fe	C	Mn	Si	Al	Ti	O	N	P	S
WZ 1	Bal.	0.056 ±0.002	1.30 ±0.24	0.46 ±0.13	0.082 ±0.003	0.0040 ±0.0001	0.018 ±0.003	0.0094 ±0.0007	0.0092 ±0.0001	0.011 ±0.008
WZ 2	Bal.	0.052 ±0.003	1.18 ±0.19	0.52 ±0.13	0.23 ±0.01	0.0048 ±0.0003	0.012 ±0.001	0.0081 ±0.0007	0.011 ±0.004	0.010 ±0.008
WZ 3	Bal.	0.055 ±0.003	1.04 ±0.24	0.54 ±0.10	0.120 ±0.006	0.0039 ±0.0003	0.032 ±0.005	0.0030 ±0.0009	0.010 ±0.002	0.012 ±0.007
HAZ	Bal.	0.255 ±0.012	1.10 ±0.19	0.35 ±0.10	0.023 ±0.009	0.00032 ±0.00001	0.0093 ±0.0006	0.0001 ±0.00005	0.018 ±0.002	0.031 ±0.001
Rail	Bal.	0.790 ±0.053	1.14 ±0.28	0.230 ±0.023	-	-	-	-	0.043 ±0.022	0.035 ±0.020

The dendritic pearlite microstructure of the rail substrate is displayed in Figs. 1(g) and 2(g). The corresponding microstructure contains coarse trails of acicular ferritic colonies and a considerable number of fine carbides that are spread throughout the partially and fully pearlitic matrix. The existing acicular ferrite along the grain-boundary pearlite is known as Widmanstätten ferrite [1]. Therefore, the rail substrate microstructure is generally consisted of pearlite, blended with ferrite and carbide.

According to quasi-binary Fe-Al diagram in Fig. 3, for the low-aluminum weld wire used in this study—which contains approximately 0.5 wt.% of aluminum—the microstructure of the WZ is found to be majorly consisted of α-ferrite and the mixture of α-ferrite and cementite (i.e., pearlite) at room temperature [2]. Ferrite and pearlite are distinctive in Fig. 1, as they appeared in light-etched and dark-etched grain structure, respectively. Referring to Table 1, the trend of aluminum content concentration shows that it increases from WZ1 to WZ2 and then decreases towards WZ3. Li et al. [3] showed that the surfacing weld layer becomes more pore-sensitive as the aluminum content decreases. Thus, the presence of low aluminum content (< 1.45 wt%) in steel welds along with the resided aluminum oxide from flux particles contribute to formation of non-metallic inclusions containing Al_2O_3 and AlN, which are the fundamental motivation of pore formation. In spite of the detrimental consequence of pore development in low-aluminum steel welds that can subsequently lead to cleavage fracture and cracks, the nucleation of ferrite is the beneficial effect of such inclusions. The ferrite aggregation is directly correlated with aluminum content, whereas the pearlite amount is adversely correlated. Therefore, it can be seen that as the aluminum content increases from WZ1 to WZ2 (see Table 1), the size and concentration of pores is decreased from WZ1 (Fig. 2c) to WZ2 (Fig. 2d), while decreasing aluminum content from WZ2 (Fig. 2d) to WZ3 (Fig. 2e) leads to an increase in pore size and concentration.

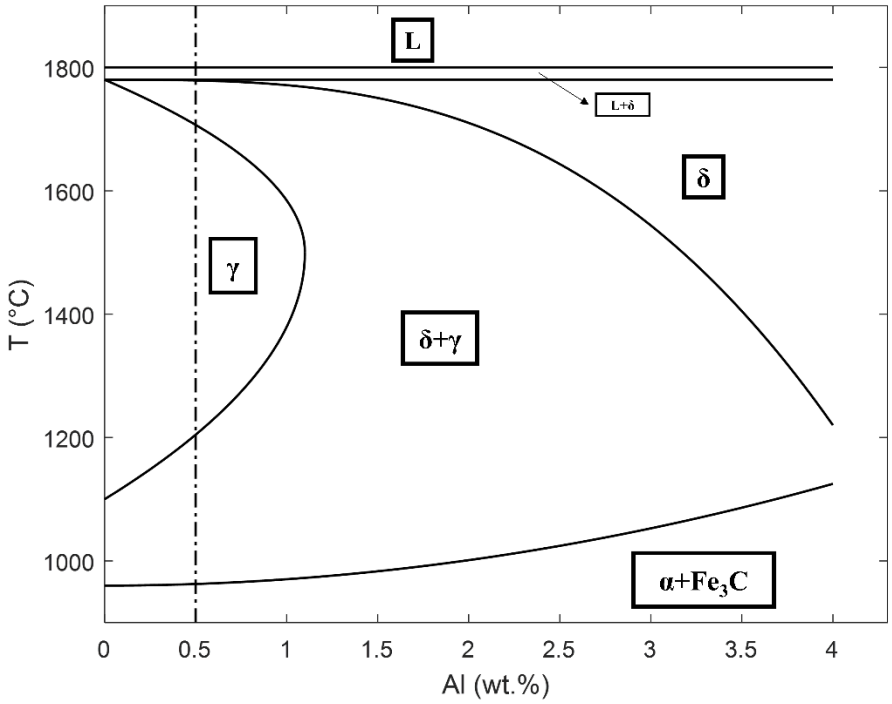

Fig. 3.3 Fe-Al quasi-binary phase diagram for the low-aluminum (0.5 wt.% of Al content) E71T-1C weld wire used for SAW-repair process [2]; δ: δ-ferrite, α: α-ferrite, γ: austenite, and Fe3C: cementite.

An analogy between WZ1 (Fig. 2c) and WZ3 (Fig. 2e) also shows the coarser pore size in WZ1 as a result of lower aluminum content in this zone rather than WZ3 (Table 1). The preceding decrease-increase trend of pore concentration is also distinctive in Fig. 1b. With regard to microstructure distribution, OM morphologies in Fig. 1 show a fine equiaxed grain structure with uniform distribution in weld zone. Nevertheless, the low aluminum content in WZ1 (Table 1) has resulted in a high portion of pearlite, a moderate fraction of grain-boundary ferrite, and a minor amount of austenite in this zone (Fig. 1c). The presence of residual austenite can be caused by the high cooling rate at the top portion of the WZ, where the arc as the heat source is rapidly removed after finishing the SAW process; hence, as shown in the phase diagram in Fig. 3, a tiny fraction of austenite may remain in the weld microstructure as a result of fast cooling to room temperature. The WZ2 is predominantly consisted of ferrite and austenite that are evenly spread all over the zone, along with a sparse fraction of pearlite (Fig. 1d) in virtue of the ascending trend of aluminum content from WZ1 to WZ2 (see Table 1). The pearlite fraction aggregates in WZ3 compared to WZ2 according to Figs. 1e and 1d, respectively, although it still has lower fraction rather than that in WZ1 (Fig. 1c). Further, as Fig. 1e shows, there are no signs of austenite in WZ3, the lowest zone that is cooled down more gradually rather than the upper zone as it remains exposed to the heat source for a longer time during depositing the upper zones in the SAW process; hence, there have been enough time for austenite to be fully transformed to ferrite and not resided in the microstructure. There may be a deficient amount of fine carbide particles dispersed in the WZ that may not be visible at the provided magnifications. Hence, the primary phases that developed the WZ microstructure are ferrite, pearlite, residual austenite, and a descending amount of carbide that can probably lead to high hardness in this region.

Shen et al. [4] studied the microstructure transformation along with mechanical properties of different surfacing materials before and after processing. According to their findings, a combination of the substrate and surfacing zone builds up the HAZ microstructure. Likewise, the HAZ microstructure in the current sample is a mixing of the microstructure of WZ3 and rail, the abutting zones. It can be observed from Figs. 1h and 1i that moving from WZ3 and rail substrate to the HAZ and trespassing the depicted fusion boundary, the grain size and fraction of various phases are evolved significantly. As Fig. 1h shows, approaching from WZ3 downwards to the HAZ, pearlite concentration increases and a ferrite segregation occurs which then diffuses among pearlite grains. Conversely, a close look at Fig. 1i shows a grain refined zone in HAZ adjacent to the coarsened grain zone of the rail substrate, where the pearlite phase has been segregated gradually from the rail zone upwards to the HAZ and then dispersed throughout the ferrite matrix. In this way, as it is evident in Fig. 1f, the HAZ is consisted of a uniform fine-grained non-dendritic microstructure of ferrite and pearlite. Fig. 2f shows that carbides are also developed all over the HAZ. The corresponding fine and uniform microstructure promises a great hardness and satisfactory mechanical properties and, subsequently, a durable bonding between rail and weld materials. However, it can be seen in Fig. 2f that a great amount of micro pores is breached throughout the HAZ, which can be the basic sites of crack initiation and propagation and consequently material rupture. Such a condensed concentration of micro pores at HAZ can be described as a result of fluctuation of liquid particles at the fusion zone during welding and also various cooling rates in different locations that can finally result in forming defects. Besides, the C-Mn rail substrate is a high carbon steel, which makes it a low-grade substrate in the matter of weldability. As a result, submerged arc surfacing process on such a high carbon steel may lead to pore and crack development at the fusion zone that can be mitigated through heat treatment process later on.

Mori et al. [5] figured out that the present titanium during welding takes part in the de-oxidation process and develops fine titanium-coated oxides that help inter-granular nucleation of ferrites. In addition, Fleck et al. [6] reported that the oxygen element in welding process contributes in establishing fine oxides that attach to the austenite and pearlite grain boundaries and release more space for nucleation of ferrite. Table 1, moving from WZ3 towards HAZ, exhibits losses in titanium and oxygen, the helpful elements for nucleation of ferrite, according to the previous studies mentioned earlier. This descending trend in titanium and oxygen correlates the decreasing in ferrite volume fraction from WZ3 to HAZ, as shown in Fig. 1h. Fleck et al. [6] demonstrated the effect of oxygen in decreasing grain boundary of ferrite that ultimately tends to finer lath size and higher density of ferrite. Also Table 1, moving from rail zone to HAZ, shows an amount of oxygen intrusion, which resulted in refined lath size of ferrite phase, the fact that can be observed in Fig. 1i as well. The carbon dilution phenomenon, which leads to penetration of carbon from high-carbon rail substrate through to the HAZ, causes a sudden rise in carbon percentage in HAZ compared to WZ (Table 1). This abrupt increase in carbon fraction is the basic argument of carbide volume fraction growth in HAZ over against the WZ. It can be seen in Table 1 that the content of manganese, as an austenite-forming element, is decreased gradually from WZ1 to WZ3, just like gradual descending of austenite fraction through the same path, from WZ1 (Fig. 1c) to WZ3 (Fig. 1e). On the other hand, increasing ferrite-forming silicon element helps the ferrite aggregation in the path from WZ1 to WZ3, as shown from Figs. 1c to 1e. According to Fonstein [7], the ferrite-forming elements, like silicon here, are beneficial for boosting mechanical properties like hardness

and cracking resistance. The analysis of the effect of chemical composition on the formation rate of ferrite, pearlite, and austenite phases has shown the influence of alloying element proportion on microstructure phase morphology. It was demonstrated that inclusion of aluminum oxide causes creation of detrimental micro pores, although it can slightly help ferrite formation. It could also be inferred how the loss of austenite-forming elements and inclusion of ferrite-forming elements can substantially improve nucleation of ferrite that conclusively benefits the hardenability and yield strength of the material.

In the next step, the AB specimen is quenched following the procedure described in Sec. 2.3. The optical and scanning electron microstructure of the as-quenched (AQ) specimen are shown in Figs. 4 and 5, respectively. Comparing the AQ sample (Fig. 4a) with the AB (Fig. 1a), the HAZ is vanished in the AQ specimen and is no longer distinguishable with the naked eye. It can be construed that the residing elements in HAZ have been dispersed throughout the sample during the quenching process. The general macrograph of the AQ sample in Fig. 4b shows that the weld zone has been transformed into a dark-colored, fine-grained structure, and the HAZ/rail boundary is not as clear as what it was in the AB case. Table 2 shows the resulting chemical composition of different zones of the AQ sample.

Comparing Figs. 1g and 4g, the rail zone has been transformed from a pearlitic microstructure into a bainitic microstructure. Bainitic ferrite plates consisting of retained austenite and untempered martensite appeared in dark-colored islands, and bainite in light color with finer grain structure are observable in the rail zone in Fig. 4g. Although austenite and untempered martensite are not distinguishable in Fig. 4g, they are distinct as medium-dark-colored and deep-dark-colored areas, respectively, in the SEM morphologies in Fig. 5g. Also, moderate amounts of precipitated carbides are dispersed throughout the ferritic matrix. This bainitic microstructure for a heat-treated rail steel comprising carbides inside ferrite laths is classified as lower bainite by Singh et al. [8].

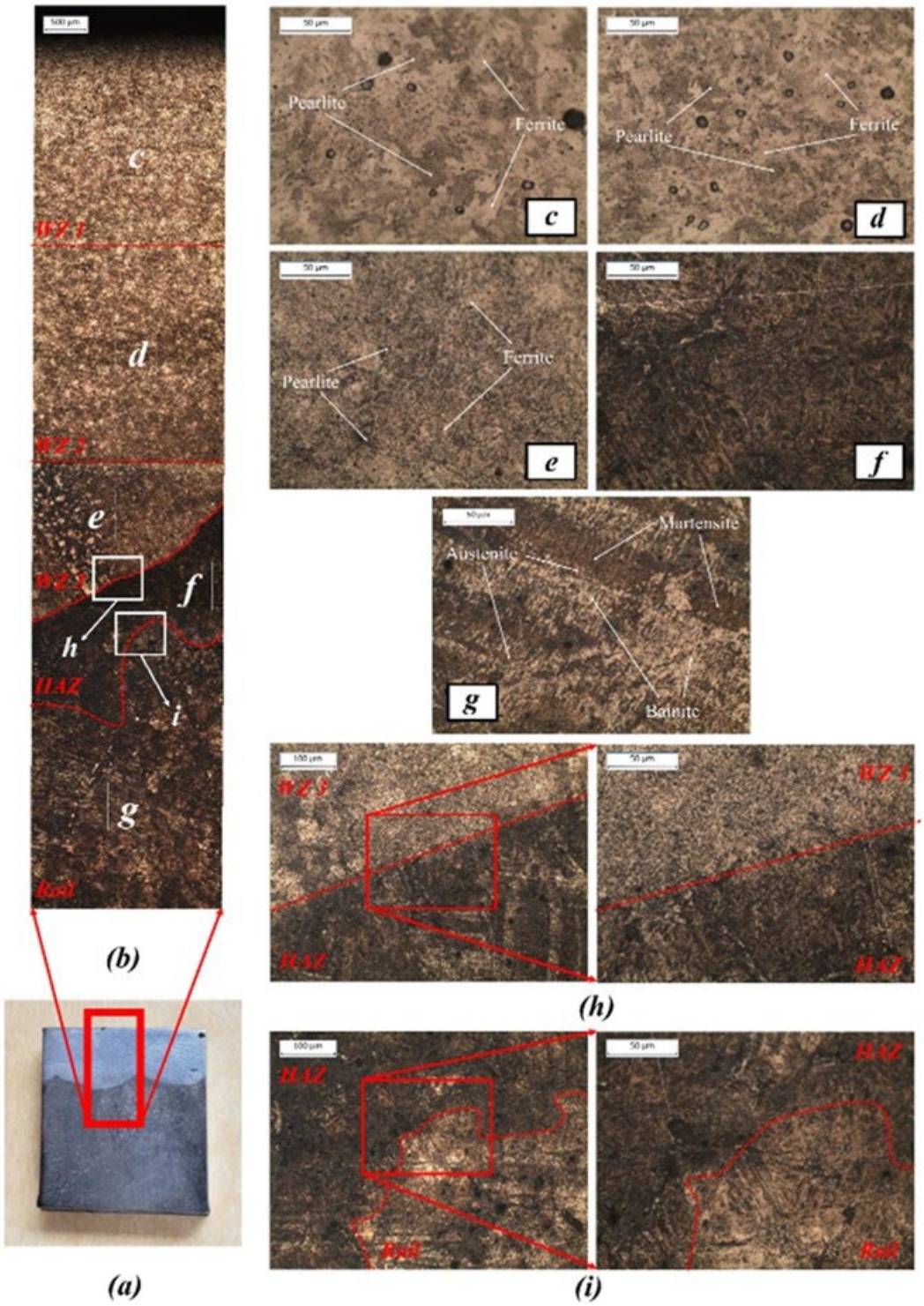

Fig. 3.4 (a) a chopped piece from the metallographic as-quenched (AQ) specimen; (b) Optical macrograph covering weld zone (WZ), heat-affected zone (HAZ), and rail zone; OM micrographs of (c) WZ1, (d) WZ2, (e) WZ3, (f) HAZ, (g) rail, (h) WZ/HAZ fusion boundary, and (i) HAZ/rail fusion boundary are also illustrated.

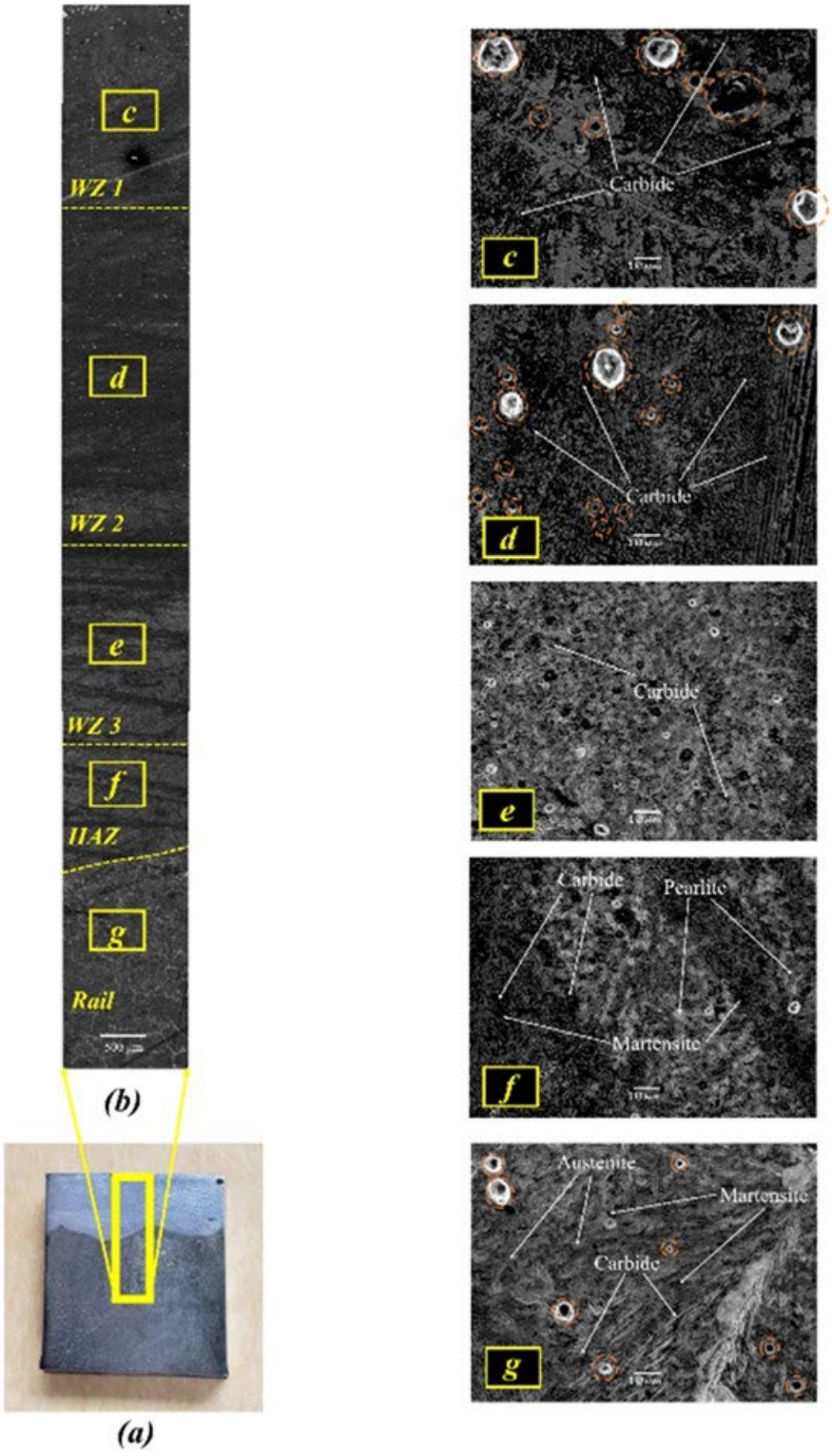

Fig. 3.5 (a) a chopped piece from the metallographic as-quenched (AQ) specimen; (b) Optical macrograph covering weld zone (WZ), heat-affected zone (HAZ), and rail zone; SEM micrographs of (c) WZ1, (d) WZ2, (e) WZ3, (f) HAZ, and (g) rail are also illustrated.

Table 7 Chemical composition of different zones of the as-quenched (AQ) SAW-repaired light rail specimen (wt.%).

Zone	Fe	C	Mn	Si	Al	Ti	O	N	P	S
WZ 1	Bal.	0.140 ±0.030	0.166 ±0.010	0.057 ±0.005	0.012 ±0.001	0.0005 ±0.0001	0.953 ±0.080	0.0016 ±0.0009	0.0004 ±0.0002	0.0005 ±0.0002
WZ 2	Bal.	0.120 ±0.020	0.548 ±0.039	0.066 ±0.005	0.033 ±0.003	0.0006 ±0.0001	0.895 ±0.052	0.0014 ±0.0008	0.0010 ±0.0001	0.0005 ±0.0002
WZ 3	Bal.	0.180 ±0.030	0.230 ±0.022	0.086 ±0.005	0.017 ±0.003	0.0004 ±0.0001	1.010 ±0.075	0.0005 ±0.0002	0.0009 ±0.0001	0.0005 ±0.0001
HAZ	Bal.	0.310 ±0.020	0.403 ±0.076	0.010 ±0.004	0.0090 ±0.0003	0.000040 ±0.000006	0.830 ±0.080	-	0.0023 ±0.0001	0.0044 ±0.0007
Rail	Bal.	0.320 ±0.016	0.110 ±0.019	0.065 ±0.007	-	-	0.796 ±0.033	-	0.012 ±0.005	0.010 ±0.005

The presence of coarse pores, which are located with dashed orange circles in Fig. 5g, can be attributed to dissolution of CO_2, due to the exposure to water phase and subsequently intrusion of H_2CO_3 and $FeCO_3$ that leads to formation of porous microstructure with precipitated cementite lamellae (Fe_3C) along pore boundaries [9]. The high wt.% of oxygen in rail zone that is shown in Table 2 confirms the chain of oxidation procedure during water quenching.

With regard to the weld zone, Figs. 4c and 4d shows that WZ1 and WZ2 have become almost identical in microstructure topography, in a way that they can be assigned with one integral zone. Since the AB sample has been heated up to 1100 °C, according to the quasi-binary diagram in Fig. 3, the sample has been partially austenized and no primary austenite has been initiated during the heat treatment process. Accordingly, no retained austenite is visible in microstructure of WZ1 and WZ2 shown in Fig. 4c and 4d. The dominant visible element in WZ1 and WZ2 microstructure is the carbide precipitations that are visible all over the region (see Figs. 5c and 5d). Based on Santofimia et al. [10], carbide precipitations are the lands of sinking carbon that draw the carbons in and do not let them to participate in austenite stabilization, which again explains why austenite is absent in the upper two weld zones. The high density of carbide particles as carbon inhalation lands has considerably led to an increase in carbon weight percentage in these zones as shown in Table 2 for WZ1 and WZ2. The volume fraction of pearlite, which appeared in dark-etched color, has been increased in the AQ sample for the upper weld zones, especially for WZ2, which, along with the carbides, can substantially help increasing hardness in these zones. It is noted, however, that density and size of the pores in WZ1 and WZ2 in the AQ sample increase, which can be associated with the immense oxygen infiltration in this area. This aggression of oxygen helps commencing Al_2O_3 inclusion that is the main reason of pore creation in microstructures; it can be observed by comparing Figs. 2c and 2d with Figs. 5c and 5d. The same pearlite, ferrite, and carbide are the fundamental elements of WZ3, but with exceptionally finer grain structure (Fig. 4e), which can potentially guarantee great hardness values in this region. According to Table 2, WZ3 presents the highest wt.% of oxygen, which, according to the assertion of Fleck et al. [6], describes the fine-grain structure of the WZ3. The percentage of pearlite in this section has also been markedly increased compared to the AB sample, before quenching. Such growth in pearlitic microstructure can be explained based on the Fe-Al quasi-binary diagram in Fig. 3. At the time that the sample is heated up to 1100 °C, the primary phases consisting weld materials are austenite and δ-ferrite. If the sample would cool down gradually, there was enough time for microstructures to be fully transferred to α-ferrite and cementite. However, as the sample is immediately water-quenched, there will not be enough time for the complete transformation, and hence, a portion of austenite

and δ-ferrite will be resided in the microstructure. Due to the presence of carbides, as discussed earlier, there are not enough carbon to stabilize the residual austenite, and thus, the unstable austenite transfers either to α-ferrite or δ-ferrite. On the other hand, due to a great amount of carbon penetration in weld zone, according to the chemical analysis in Table 2, nucleation of cementite (Fe_3C) starts to grow dramatically, which, with the presence of the ferrite, nucleates more pearlite.

The deep dark etching of the HAZ has made the microstructure slightly invisible. According to the SEM micrograph in Fig. 5f, the HAZ seems to be dominantly consisted of untempered martensite and pearlite. On one hand, Fig. 4h, from WZ3 towards the HAZ, shows that the light-colored island has disappeared and the dark-colored region, which is pearlite, has remained. On the other hand, moving upward from rail zone to HAZ in Fig. 4i, the bainite phase that is light-etched vanishes and the dark-etched area of austenite and untempered martensite remains. Based on the study by Shen et al. [4], this observation confirms the presence of martensite and pearlite in HAZ, and also the numerous carbides that are detectable in the HAZ in Fig. 5f.

3.1.2. LPD-repaired light rail

Fig. 6 shows the OM morphology of the as-built (AB) specimen. Based on Fig. 6a, the AB sample technically can be divided into three zones, i.e., the deposition zone (DZ), the heat-affected zone (HAZ), and the rail zone. Figs. 6c and 6d show magnified micrographs of the rail and the HAZ, respectively. Figs. 6e to 6j show the enlarged OM micrographs of the first to sixth deposition layers. Fig. 7 shows the corresponding SEM micrographs of the different zones. Table 3 provides the chemical compositions of the different zones of the AB specimen.

The authentic microstructure of the C-Mn rail steel is thin lamellar pearlite. Accordingly, as shown in Fig. 6c, the rail material primarily is constituted of dendritic pearlite with random lamellae orientation and pro-eutectoid ferrite. The SEM micrograph in Fig. 7c shows that there are abundant carbides distributed throughout the pearlitic matrix. Hence, the microstructure of the rail zone in the AB specimen typically is composed of a pearlitic-ferritic microstructure that contains thoroughly-dispersed fine carbides.

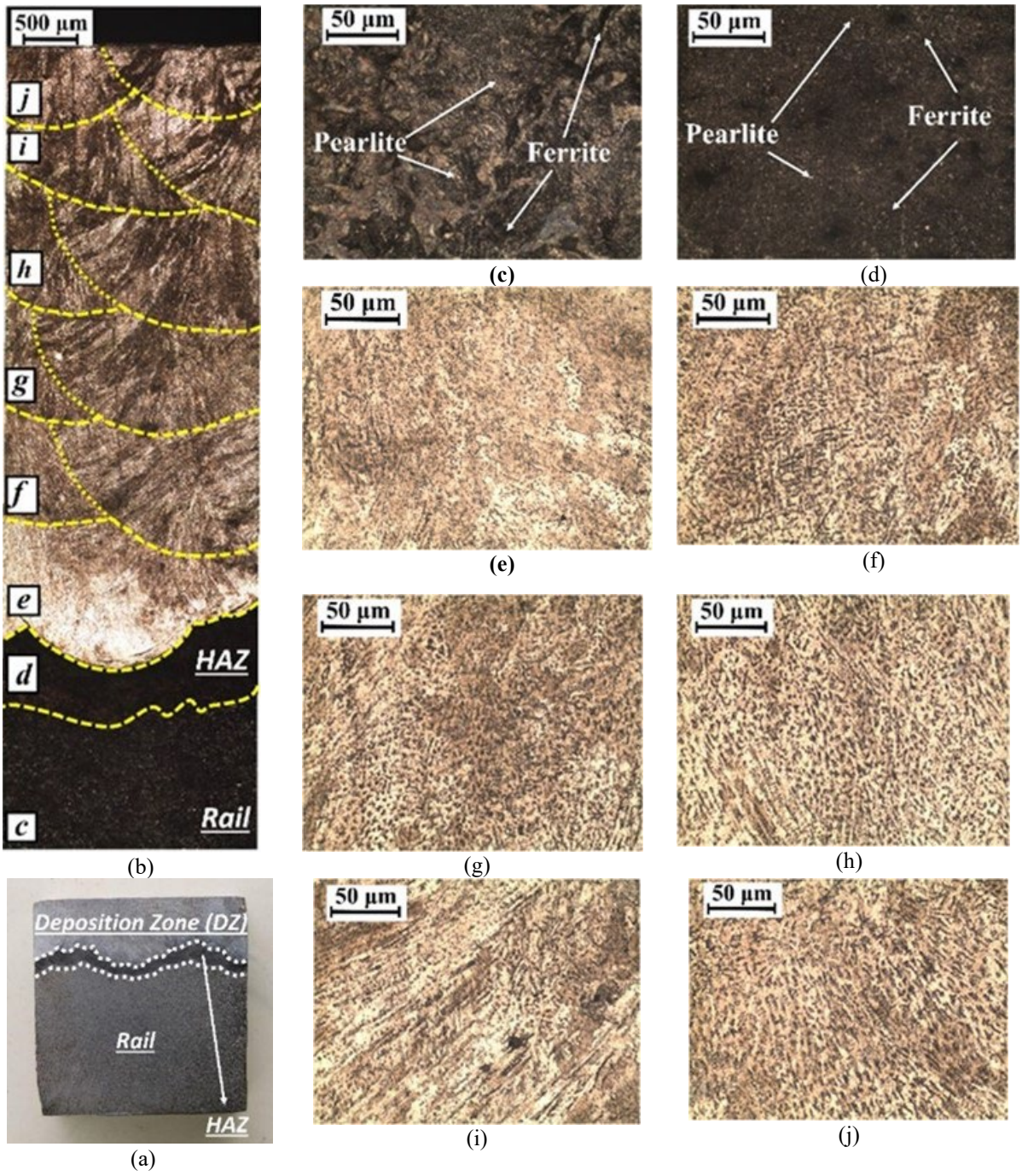

Fig. 3.6 (a) The metallographic sample chopped from the AB specimen; (b) A comprehensive OM macrograph covering DZ, HAZ, and rail; (c) OM micrograph of the rail and (d) HAZ; OM micrographs of DZ are separated layer-wise in (e), (f), (g), (h), (i), and (j), representing first, second, third, fourth, fifth, and sixth deposition layers, respectively.

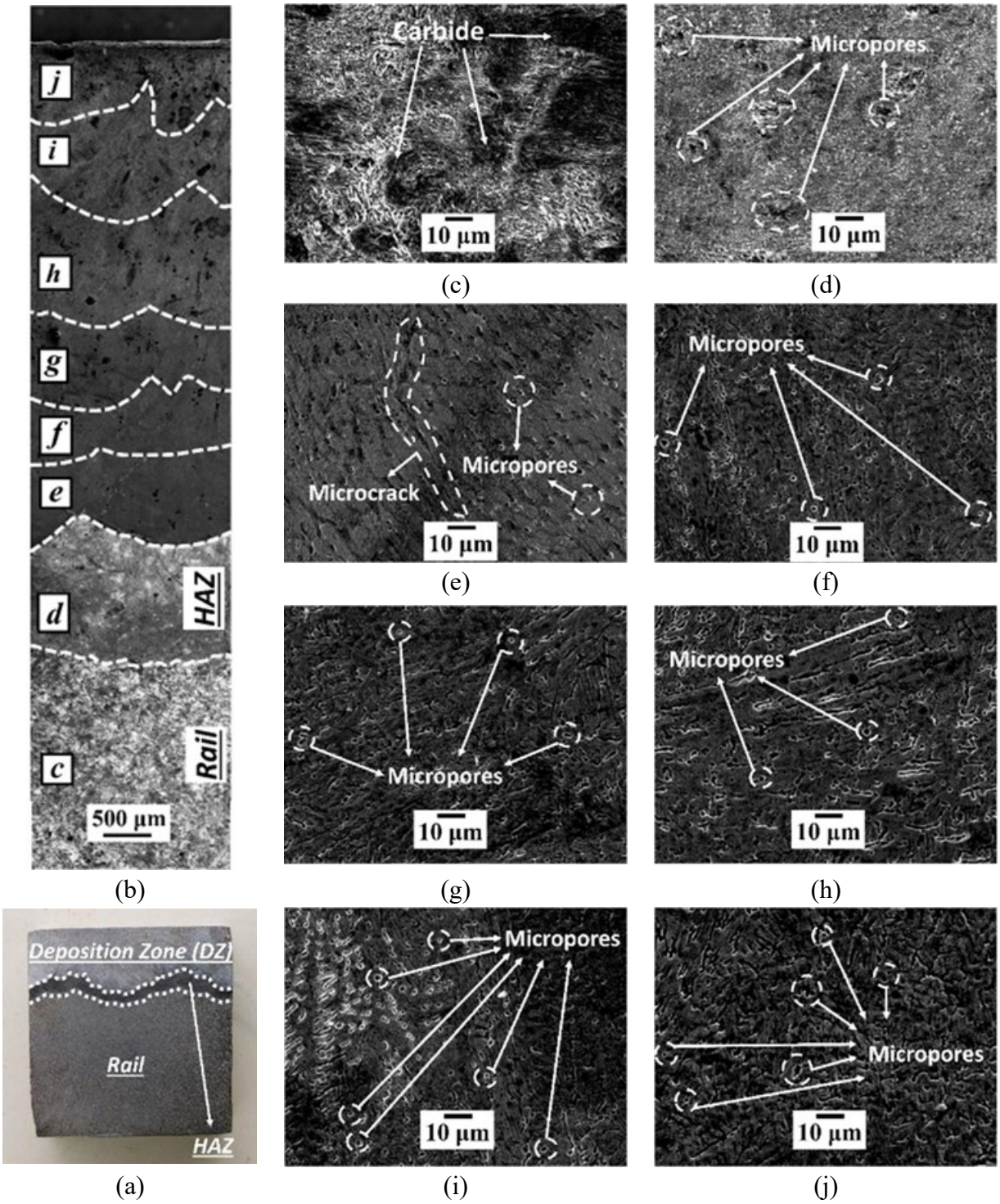

Fig. 3.7 (a) The metallographic sample chopped from the AB specimen; (b) A comprehensive SEM macrograph covering DZ, HAZ, and rail; (c) SEM micrograph of the rail and (d) HAZ; SEM micrographs of DZ are separated layer-wise in (e), (f), (g), (h), (i), and (j), representing first, second, third, fourth, fifth, and sixth deposition layers, respectively.

Table 8 Chemical composition of the as-built (AB) LPD-repaired light rail specimen at different zones (wt.%).

Material	Fe	C	Cr	Mn	Si	Ni	O	N	P	S	Cu	Mo
DZ-6*	Bal.	0.0179 ±0.0021	16.47 ±1.32	1.86 ±0.17	0.20 ±0.05	8.84 ±0.57	0.0136 ±0.0029	0.079 ±0.001	0.009 ±0.0006	0.007 ±0.0002	0.036 ±0.003	0.039 ±0.60
DZ-5	Bal.	0.0113 ±0.0014	16.01 ±1.18	1.79 ±0.15	0.19 ±0.03	8.12 ±0.54	0.0103 ±0.0027	0.078 ±0.001	0.010 ±0.006	0.007 ±0.24	0.027 ±0.002	0.042 ±0.005
DZ-4	Bal.	0.0079 ±0.0008	17.82 ±1.44	1.50 ±0.11	0.25 ±0.05	7.21 ±0.56	0.0176 ±0.0026	0.082 ±0.004	0.008 ±0.0009	0.008 ±0.0003	0.048 ±0.001	0.041 ±0.006
DZ-3	Bal.	0.0073 ±0.0005	17.67 ±1.24	1.46 ±0.17	0.28 ±0.01	7.19 ±0.63	0.0101 ±0.0031	0.080 ±0.007	0.009 ±0.0005	0.008 ±0.0005	0.031 ±0.001	0.042 ±0.004
DZ-2	Bal.	0.0061 ±0.0005	17.24 ±1.05	1.43 ±0.16	0.30 ±0.03	7.22 ±0.52	0.0147 ±0.0027	0.079 ±0.003	0.009 ±0.0001	0.006 ±0.0008	0.043 ±0.003	0.045 ±0.001
DZ-1	Bal.	0.0040 ±0.0003	15.29 ±1.12	1.50 ±0.16	0.36 ±0.05	8.09 ±0.49	0.0147 ±0.0026	0.084 ±0.003	0.012 ±0.007	0.009 ±0.0003	0.031 ±0.001	0.033 ±0.006
HAZ	Bal.	0.270 ±0.051	9.94 ±0.17	1.16 ±0.18	0.27 ±0.07	0.062 ±0.001	0.0016 ±0.0008	0.00074 ±0.00004	0.011 ±0.007	0.007 ±0.0005	0.0014 ±0.0001	0.0010 ±0.0003
Rail	Bal.	0.790 ±0.053	-	1.14 ±0.28	0.230 ±0.023	-	-	-	0.043 ±0.022	0.035 ±0.020	-	-

* DZ – 6 means "deposition zone – sixth deposited layer". Same description applies to the other terms listed in this Table with the same format.

To render a crack-resistant structure for a welded/deposited alloy, a microstructure consisting of 5 to 10 vol.% of δ-ferrite must be developed. To attain this goal, the ratio of ferrite stabilizers (Cr, Si, Mo) to austenite stabilizers (Ni, C, Mn, N) must be fine-tuned. Fu et al. [11] identified the solidification trend of 304L as a ferritic-austenitic mode, which is demonstrated specifically as a dash-dot vertical line in the Fe-Cr-Ni pseudobinary phase diagram in Fig. 8. Referring to Fig. 6e, the primary austenitic microstructure of the first deposited layer (DZ-1) has three regions in the matter of the color spectrum, i.e., dark-etched, light-etched, and semi-dark-etched. The light-etched austenite is essentially surrounded by the dark-etched area that represents vermicular delta ferrite. At the time of the deposition of DZ-1, the rail initially was at the ambient temperature, so DZ-1 underwent rapid cooling due to the low bed temperature. As a result, referring to Fig. 8, cooling through the δ+γ domain, i.e., from the ferrite solvus temperature, $T_{d\text{-}solvus}$, to the austenite solvus temperature, $T_{\gamma\text{-}solvus}$, occurs so rapidly that the diffusion of Cr and Ni was eliminated. Thus, the hypothesis is that fast cooling below $T_{\gamma\text{-}solvus}$ causes a massive δ→γ transformation, and, as a consequence, δ-ferrite becomes supersaturated compared to austenite [12]. Hence, the semi-dark network in Fig. 6e resolutely offers the part of δ-ferrite that is transformed to austenite via the massive δ→γ transformation process during the first step of fast cooling. Referring to Fig. 8, a critical note to mention is that, after prolonged exposure of δ-ferrite to temperatures around 600°C, it is transformed to the brittle sigma phase [13,14]. The DZ-1 has been periodically exposed to newly-induced thermal cycles when the subsequent layers were deposited, and this has kept this layer at elevated temperatures long enough to allow the δ→σ transformation. Thus, one can say that part of the semi-dark region, i.e., the part that is nearer to the dark-etched retained ferrite cellular boundaries, indeed is representing the sigma phase. The SEM micrograph of the DZ-1 in Fig. 7e shows several micropores dispersed all over the structure, and there also are signs that microcracks have developed. The gas that is entrapped in the melt pool during LPD is the main cause of the formation of near-spherical micropores. Suutala and Moisio [15] showed the extent to which the cracking sensitivity of conventionally-welded, stainless steel alloys depend on their chemical compositions, specifically the total weight percentage (wt.%) of sulfur and phosphorus (P+S). Later, Pacary et al. [16] established an improved version of the Suutala diagram specifically

for laser welding. Based on their findings, cracking begins in the microstructure of a laser-deposited 304L austenitic stainless steel only when (P+S) ≥ 0.018. Table 3 shows that the total wt.% of P + S for DZ-1 is greater than 0.018.

Fig. 6f shows a primary δ-ferrite microstructure for DZ-2. Since the deposition bed of DZ-2 was the high-temperature DZ-1, it has experienced a much slower cooling rate than DZ-1. Hence, no massive δ→γ transformation has occurred during the deposition of DZ-2, which is the reason the semi-dark area has been diminished in this layer (Fig. 6f) compared to DZ-1 (Fig. 6e). The ferrites in Fig. 6f appeared mostly to be in the shape of thin, dark lines that have been laid at the cores of the subgrains. These lines represent the Cr-enriched and Ni-depleted composition, and they are shaped during the early transient stages of the initial solidification. Table 3 also shows that, when moving from DZ-1 to DZ-2, the wt.% of ferrite-stabilizing chromium is increased, while wt.% values of both the austenite-stabilizing nickel and manganese are decreased. In Fig. 7f, signs of micropores are detectable in DZ-2, but there are no distinguishable symptoms of microcracks in this layer. Table 3 indicates that P+S in DZ-2 is less than 0.018 wt.%, which describes the absence of microcracks in this region.

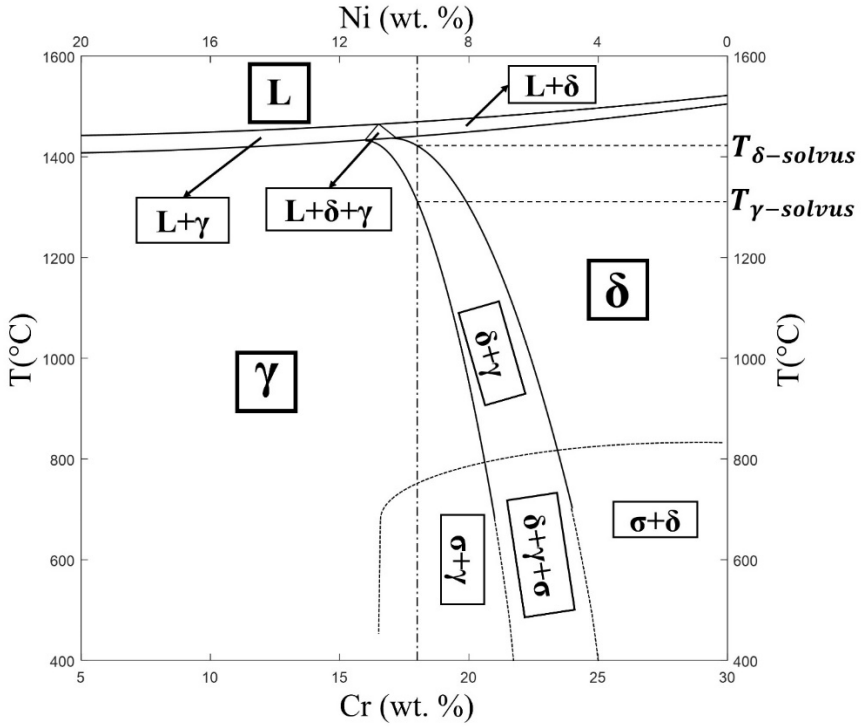

Fig. 3.8 Phase diagram of the Fe-Cr-Ni pseudobinary system for 304L (70 wt.% Fe) used in powder form for the LPD repair process. L: liquid; δ: δ-ferrite; γ: austenite; σ: sigma.

Comparing the microstructures of DZ-2 and DZ-3 in Figs. 6f and 6g, respectively, show that they have almost the same phase distribution. Comparing the chemical compositions of DZ-2 and DZ-3 in Table 3 indicates that the wt.% of the ferritizers (Cr, Si, Mo) and the wt.% of the austenizers (Ni, Mn, C, N) are almost equal in these two layers. This provides a strong rationale for the identical microstructures of DZ-2 and DZ-3. This analogy describes that DZ-2 and DZ-3

experienced the same thermal history, i.e., both were deposited on a hot substrate and then exposed to multiple cycles of heating and cooling due to the deposition of the upper layers.

These same reasons explain the microstructural similarity of DZ-4 (Fig. 6h) and DZ-3 (Fig. 6g). The SEM micrographs of DZ-3 and DZ-4 in Figs. 7g and 7h, respectively, show practically the same micropores and microcracks based on size and accumulation, which can be explained by noting that the total P+S wt.% for both layers is less than 0.018, as recorded in Table 3.

Moving from DZ-4 (Fig. 6h) to DZ-5 (Fig. 6i), the general microstructure switches to primary austenite. Fig. 6i resembles a light-etched austenitic matrix that is mixed with a dark-etched ferritic network that is appeared as acicular/lath-like ferrite. An insignificant, semi-dark, supersaturated δ-ferrite also is observable in DZ-5. This layer was not cooled as fast as DZ-1, because of higher bed temperature, but it was cooled faster than DZ-2, DZ-3, and DZ-4 because it has been reheated only once, while the lower layers have been reheated at least twice. Hence, DZ-5 has experienced a moderate cooling rate, i.e., a rate that allowed adequate time for the complete δ→γ transformation. However, this time interval was too short to allow for the development of brittle sigma, but it was not short enough to cause a great extent of massive δ→γ transformation. Accordingly, the final microstructure is primarily austenite, but there is still a slight fraction of the semi-dark, supersaturated δ-ferrite. Table 3 also shows that the wt.% of Ni and Mn, the most powerful austenizers, is increased dramatically in DZ-5 compared to the former layers. Although the other austenizer, N, is decreased in DZ-5, it is not as much of a determinant as Ni and Mn to be able to downgrade the austenite in this layer. Exploring ferritizers in Table 3 states that Si and Cr, as the most powerful ferrite promoters, are decreased markedly in DZ-5 rather than in the previous layers, which again describes the logic of the primary austenite microstructure in this zone. A sensible increase in the concentration of micropores in DZ-5 in comparison with the former layers is evident in Fig. 7i. The porosity level of the laser-cladded materials is inversely correlated with the laser power. Despite the constant laser power used to deposit all six layers, the lower layers are exposed to laser power multiple times during the deposition of the upper layers, even though the subsequent exposures were not as powerful as the first exposure. Therefore, a fraction of the micropores that developed in every deposited layer has disappeared due to their being reheated. Thus, it is logical that DZ-5, which is reheated only once, has more micropores than the lower layers that are reheated several times.

Based on the observations in Fig. 6j, DZ-6 is composed of a fine-grained microstructure in which the austenite and vermicular δ-ferrite have almost the same weight. However, the results in Table 3 indicate that moving from the austenitic DZ-5 to DZ-6, the wt.% values of all of the austenizers, i.e., nickel, manganese, carbon, and nitrogen, have increased, while the ferritizers, including chromium, silicon, and molybdenum, have either increased only slightly, stayed nearly the same, or decreased. Hence, first, since the increment of the austenizers weighs more than that of the ferritizers, and, second, because this new region, i.e., DZ-6, is being compared with an austenitic region, i.e., DZ-5, it is concluded that the DZ-6 region primarily consists of austenite. Also, the semi-dark, supersaturated δ-ferrite is reappeared in massive quantities in this region, and the reason this occurred is attributed to this layer's faster cooling rate. The finally deposited layer, i.e., DZ-6, was not reheated and, in addition, its top surface was exposed to free air stream that helped enormously to cool it down faster. However, in contrast to what was discussed for DZ-1 as a result of reheating, since DZ-6 has not been reheated, there was not enough time for the transformation

of δ-ferrite to the sigma phase. Thus, there is little chance that the semi-dark region in DZ-6 contains any significant amount of the brittle sigma phase. As shown in Fig. 7j, the DZ-6 layer has a massive distribution of micropores due to the lack of reheating. The final noteworthy observation about DZ-5 and DZ-6 is the lack of microcracks in their microstructures (Figs. 7i and 7j), which occurred for the same reason that the wt.% of P+S in these two regions is still below 0.018 (Table 3). Generally, the DZ microstructure is composed of austenite, δ-ferrite, and sigma. DZ-1, DZ-5, and DZ-6 are primary austenite, and DZ-2, DZ-3, and DZ-4 are primary ferrite. The volume fraction of the brittle sigma phase decreases from DZ-1, which has the maximum fraction, to DZ-4, which has the minimum fraction among the first four deposition layers. DZ-5 and DZ-6 contain no sigma. The only layer that contains microcracks is DZ-1. Also, the size and density of the micropores generally increase from DZ-1 up to DZ-6.

The microstructure and mechanical properties of the HAZ always are a mixture of the two adjacent zones. Going from the rail (Fig. 6c) to the HAZ (Fig. 6d), ferrite segregation occurs and a great fraction of pearlite disappears, i.e., the minor fraction of the retained fine-grain, non-dendritic pearlite is diffused into the ferritic network. Due to the adjusted laser power, that can keep the substrate and the developed melt pool in the doughy state and not let it trespass into the diluted state, massive amounts of the deposition materials cannot penetrate through to the substrate materials. Therefore, the HAZ has been, to a great extent, immune from the intrusion of the micrograins of the deposited materials. Thus, the HAZ (Fig. 6d) has inherited only the ferrite phase from DZ-1 (Fig. 6e), which is the only phase that exists in common between rail and DZ-1. Therefore, in Fig. 6d, a uniform primary ferrite microstructure of HAZ is visible in which the fine, non-dendritic pearlite particles are distributed throughout the entire ferritic matrix. Such a consistent microstructure with a ferritic background can yield a satisfactory level of hardness and strength at the rail-deposition joint. Even so, based on the SEM observations in Fig. 7d, this region has an enormous density of coarse micropores, which are the most detrimental sites because they result in the initiation of cracks, eventually resulting in the material rupture. The oscillation of the melted powder particles at the fusion field during the LPD process and the variable local cooling rate lead to the formation of various defects that result in large numbers of micropores in the final microstructure. The other reason for the augmentation of the micropores in HAZ can be attributed to the nature of the C-Mn rail which, due to the high percentage of carbon, typically is poor-weldable steel to act as a substrate. Hence, LPD on this high-carbon steel will breach micropores at the substrate-deposition interface. Also, the chemical composition of the HAZ in Table 3 shows that the total wt.% of P+S in this region is almost equal to 0.018; this fact makes this zone vulnerable to crack initiation, even though no cracks are visible yet in SEM (Fig. 7d). However, the good thing about the HAZ is the dominancy of ferrite, which is a great benefit for increasing the crack resistance and yield strength of the material. Since the HAZ is the bridge between the rail and DZ, this area has to be the pioneer regarding hardness, yield strength, and crack resistance among all three zones to prevent any chance of cracking and delamination. Hence, it seems necessary to heat-treat the AB rail in order to alleviate the micropores and increase the immunity of the final product. In this way, the AB LPD-repaired light rail sample is heat treated following the instructions given in Sec. 2.3. The heat-treated (HT) specimen is analyzed in the following.

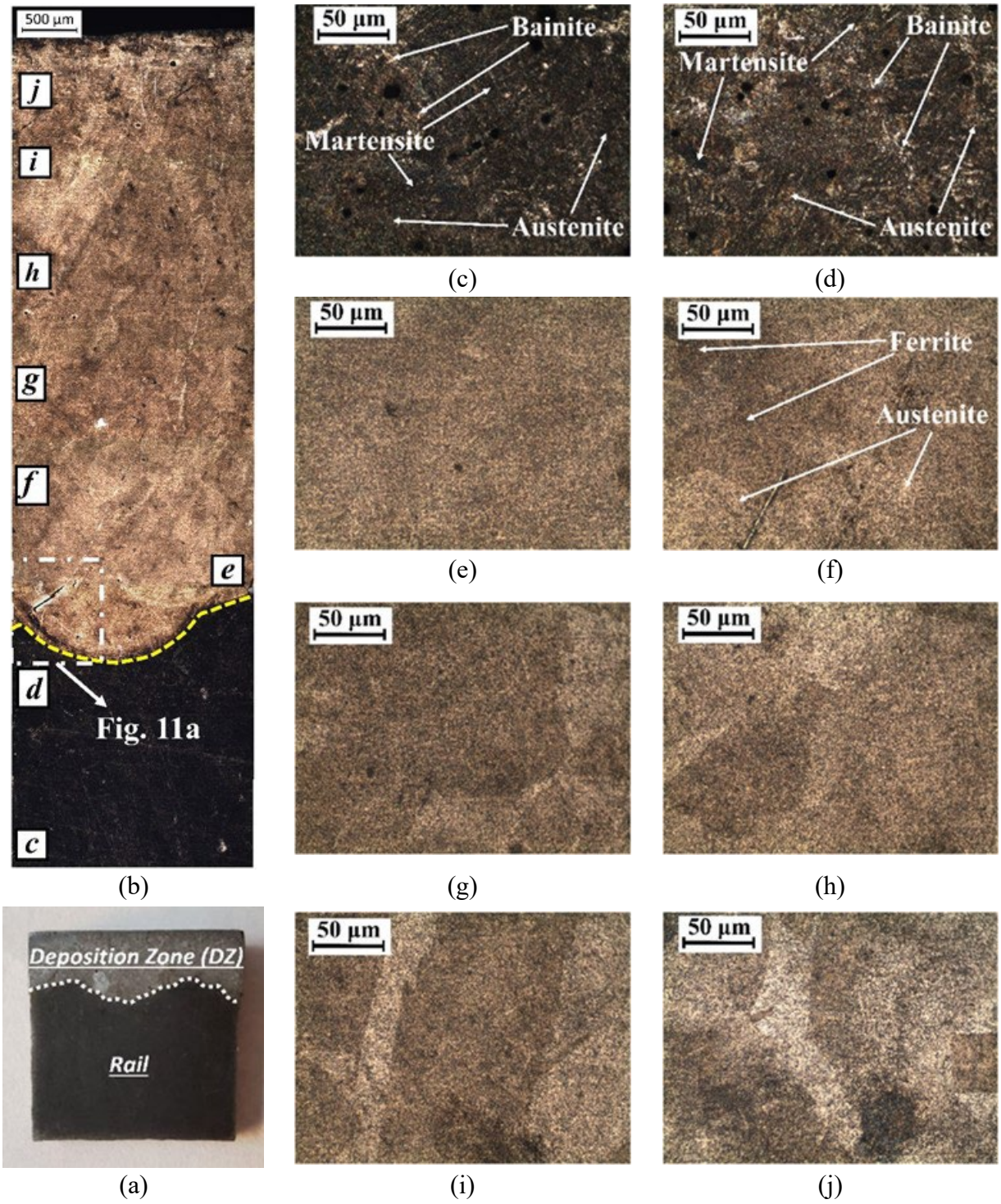

Fig. 3.9 (a) The metallographic sample chopped from the heat-treated (HT) specimen; (b) A comprehensive OM macrograph covering DZ and rail; (c) OM micrograph of rail and (d) HAZ; due to the disappearance of the interlayer boundaries at the DZ, OM micrographs are taken from the same corresponding locations in Fig. 7 at the (e) first, (f) second, (g) third, (h) fourth, (i) fifth, and (j) sixth deposition layers.

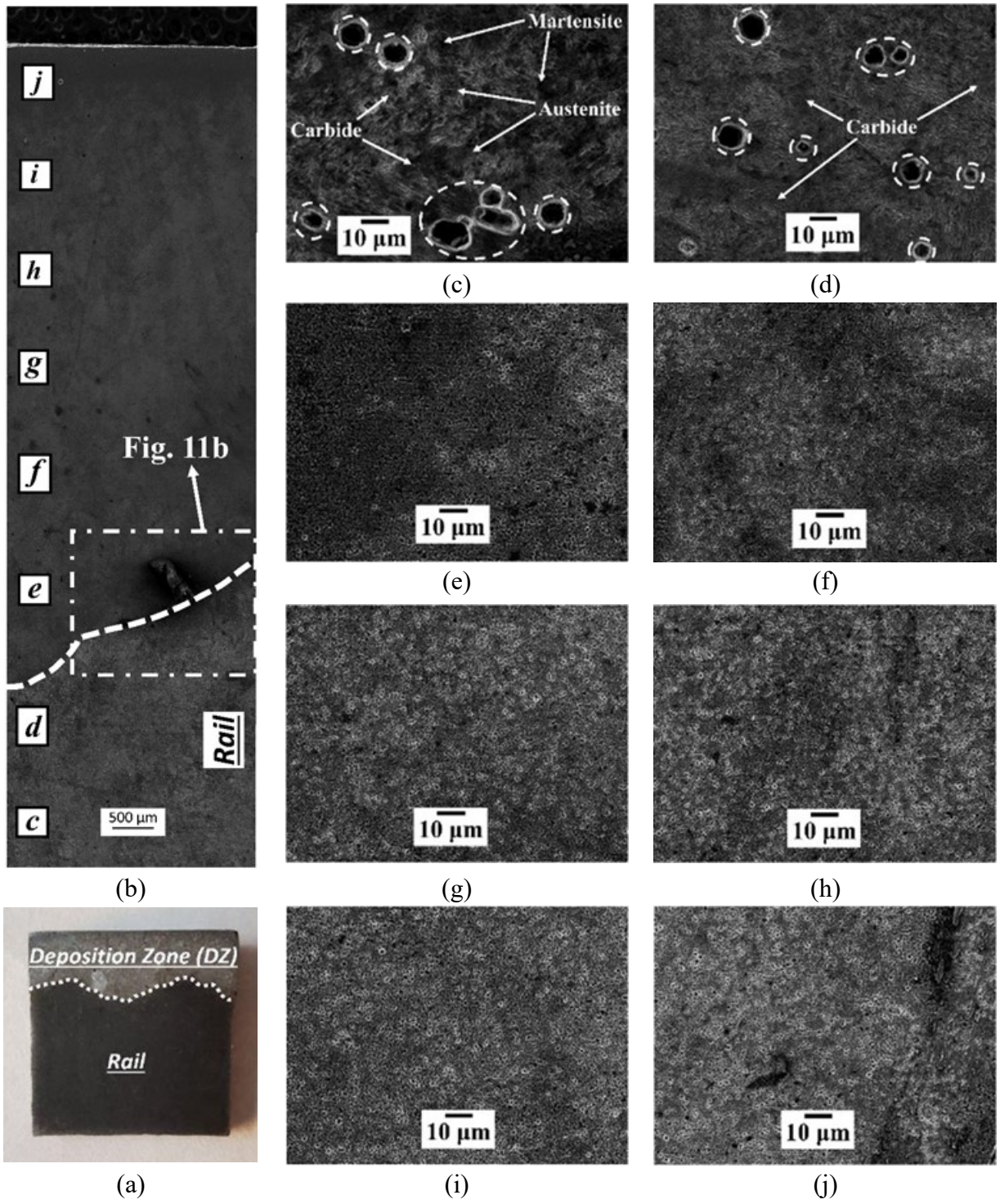

Fig. 3.10 (a) The metallographic sample chopped from the heat-treated (HT) specimen; (b) A comprehensive SEM macrograph covering DZ and rail; (c) SEM micrograph of rail and (d) HAZ; due to the disappearance of the interlayer boundaries at the DZ, OM micrographs are taken from the same corresponding locations in Fig. 8 at the (e) first, (f) second, (g) third, (h) fourth, (i) fifth, and (j) sixth deposition layers.

Table 9 Chemical composition of the heat-treated (HT) LPD-repaired light rail specimen at different zones (wt.%).

Material	Fe	C	Cr	Mn	Si	Ni	O	N	P	S	Cu	Mo
DZ-6*	Bal.	0.019 ±0.002	9.74 ±0.23	1.46 ±0.22	0.19 ±0.04	7.62 ±0.59	0.72 ±0.05	0.082 ±0.003	0.0004 ±0.0002	0.0002 ±0.0001	0.042 ±0.004	0.043 ±0.005
DZ-5	Bal.	0.023 ±0.002	7.49 ±0.35	1.54 ±0.24	0.27 ±0.03	8.22 ±0.66	0.80 ±0.04	0.071 ±0.006	0.0004 ±0.0001	0.0005 ±0.0002	0.009 ±0.001	0.036 ±0.001
DZ-4	Bal.	0.015 ±0.004	10.08 ±1.16	1.48 ±0.22	0.21 ±0.01	7.25 ±0.56	0.67 ±0.07	0.078 ±0.005	0.0009 ±0.0001	0.0012 ±0.0005	0.015 ±0.001	0.039 ±0.003
DZ-3	Bal.	0.008 ±0.001	8.01 ±0.17	0.98 ±0.07	0.23 ±0.01	7.15 ±0.56	0.89 ±0.05	0.062 ±0.008	0.0017 ±0.0003	0.0023 ±0.0003	0.025 ±0.005	0.042 ±0.001
DZ-2	Bal.	0.080 ±0.003	10.94 ±1.19	1.16 ±0.22	0.31 ±0.02	6.80 ±0.56	0.78 ±0.05	0.043 ±0.001	0.0091 ±0.0008	0.0125 ±0.0013	0.083 ±0.007	0.036 ±0.007
DZ-1	Bal.	0.073 ±0.001	10.26 ±1.98	1.10 ±0.21	0.32 ±0.04	5.40 ±0.47	0.97 ±0.07	0.051 ±0.006	0.0102 ±0.0011	0.0140 ±0.0031	0.011 ±0.005	0.012 ±0.007
HAZ	Bal.	0.294 ±0.045	3.24 ±0.10	0.57 ±0.17	0.13 ±0.09	0.22 ±0.02	1.28 ±0.80	0.0032 ±0.0002	0.017 ±0.001	0.020 ±0.003	0.0028 ±0.0004	0.0082 ±0.0003
Rail	Bal.	0.305 ±0.053	0.92 ±0.23	0.138 ±0.017	0.057 ±0.001	-	1.35 ±0.24	-	0.015 ±0.009	0.011 ±0.007	-	-

* DZ – 6 means "deposition zone – sixth deposited layer". Same description applies to the other terms listed in this Table with the same format.

Figs. 9 and 10 give OM and SEM morphologies of the HT specimen, respectively, and its chemical distribution is given in Table 4.

Regarding the rail zone, its pearlitic microstructure before heat treatment (Fig. 6c) is switched to a bainitic microstructure (Fig. 9c). The dominant bainitic ferrite plates appear as dark islands and contain untempered martensite along with retained austenite. The minor portion of the light-color, fine-grain bainite also is observable in the rail zone in Fig. 9c. SEM capture from the HT rail zone in Fig. 10c gives a clearer vision of the bainitic ferrite plates, where martensite and austenite are shown as full-dark and semi-dark areas, respectively. The SEM also shows a mild agglomeration of precipitated carbides that are distributed evenly in the entire ferritic network. The bainitic microstructure of the HT rail that contains ferrite laths with interdendritic carbides is categorized as lower bainite. It also is quite obvious the extent to which the rail zone is suffering from the established coarse micropores as they are dash-encircled in Fig. 10c. The aggregation of micropores after water quenching is due chiefly to the dissolution of CO_2, which occurs as a result of water exposure and, consequently, the intrusion of H_2CO_3 and $FeCO_3$. The dissolute CO_2 forms a porous structure where the cementite lamellae, Fe_3C, is precipitated along the boundaries of the micropores [17]. The intrusion of a high wt.% of oxygen into the rail zone (Table 4) attests the described oxidation chain during heat treatment.

One of the featured homogenizing effects of heat treatment can be seen in the DZ of the HT sample, where there is almost no microstructural inconsistency among different deposition layers (Fig. 9b) compared to that of the AB specimen (Fig. 6b). The fusion boundaries between the deposition layers have been disappeared entirely, and, after heat treatment, the DZ becomes an integral zone. The residual thermal stresses that are generated in the AB specimen during the LPD heating-cooling cycles will act as the motive force for recrystallization during heat treatment. This phenomenon results in relieving the stress thereby reducing the grain boundary interfacial free energy. As a result, the low-angle boundaries of the AB specimen are switched to high-angle boundaries in the HT sample, which makes them almost parallel to the interlayer crystallographic

orientation, which eliminates the existing misorientation at the fusion boundaries. Thus, due to the lack of interlayer boundaries in the HT sample to help discern the different deposition layers, the OM and SEM micrographs in Figs. 9 and 10 are captured at the same corresponding locations in Figs. 6 and 7 to track the microstructural evolution of each zone.

Fig. 11 shows a cross-section morphology of the microcracks that are developed at the rail-DZ interface. The current microcracks in this zone are now significantly larger after heat treatment than they were before heat treatment (Fig. 7e). Fig. 11 shows the severe oxidation around the microcracks in DZ-1 and the bonding defects at the rail-DZ interface. The cracks and defects, that had already developed, provide accelerated diffusion paths for oxygen and iron, meaning that they expose the adjacent materials to air and consequently facilitate the oxidation to occur there, making it even faster than it is at other potential locations, such as grain boundaries and deformation bands. The oxidation cracks that have propagated in the intergranular boundaries decrease the bonding strength of the grain boundaries by forming a thick oxide film at those bonding defects, thereby producing a considerable degrading effect on the fatigue performance. The chemical compositions of DZ-1 before and after heat treatment are provided in Tables 3 and 4, respectively, and they show a significant increase in the wt.% of oxygen, which explains the acute oxidation that occurred in this zone.

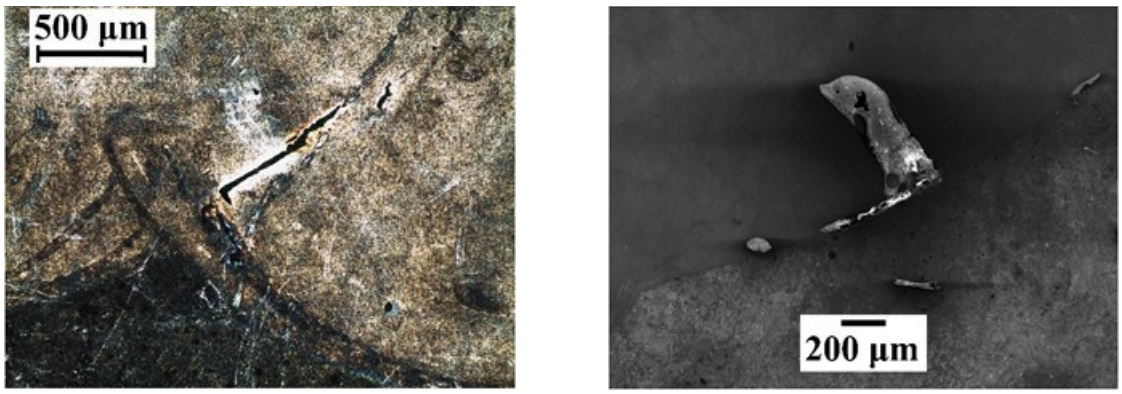

(a) (b)

Fig. 3.11 Close view of the microcracks that are developed in the heat-treated (HT) specimen at the rail-DZ interface through (a) OM and (b) SEM morphology.

A general comparison of Figs. 6e-j with Figs. 9e-j shows that the heat treatment has transformed the heterogeneous, coarse microstructure of the DZ into a homogeneous, fine-grain structure. During the heat treatment of stainless steels, oxide inclusions have a determinant role in forming the steel microstructure by participating as nucleation sites for solidification and phase transformation. It was reported by Takano et al. [18] that heat treatment changes the composition of oxide inclusions in stainless steel, which is highly dependent on the concentration of Mn, Si, and Cr. They showed that the leading cause of the fine grain structure in heat-treated austenitic stainless steel is the dissolution of the coarse $MnO\text{-}SiO_2$ inclusions and the precipitation of fine $MnO\text{-}Cr_2O_3$ inclusions during heat treatment. They also concluded that this transition occurs only if the initial Si content is sufficiently low, i.e., < 0.3 wt.%, otherwise the oxide inclusions remain as $MnO\text{-}SiO_2$. Referring to Table 3, the initial values of the wt.% of Si before heat treatment in all

of the deposition layers were kept equal to or below the boundary value of 0.3 except for DZ-1 in which the Si content exceeded 0.3% by a small amount. This fact describes the fine grain structure of the DZ of the HT sample, where the precipitated $MnO\text{-}Cr_2O_3$ inclusions have suppressed the common grain-coarsening effect of heat treatment. Regarding the phase distribution, despite the visible overall balance between the light-etched austenite and the dark-etched δ-ferrite in the DZ micrographs (Figs. 9e-j), tracing from Fig. 9e to 9j shows a gradual intensification of the light lands of austenite. Ren et al. [19] concluded that $MnO\text{-}Cr_2O_3$ inclusions have a strong pinning effect on the austenite grain boundaries in 304 stainless steel. The descending trend of the wt.% of Si from DZ-1 up to DZ-6 in the AB specimen (Table 3) yields an ascending trend of $MnO\text{-}Cr_2O_3$ inclusions along the same path for the HT sample. More $MnO\text{-}Cr_2O_3$ contributes to pinning more austenite grain boundaries, which ultimately contributes to the higher austenite volume fraction after heat treatment. Table 4 also shows that, when moving from DZ-1 to DZ-6, the Cr and Si ferritizers decrease, but the austenizing elements of Ni and N generally increase. The gradual transition from a balanced dark-light microstructure in DZ-1 to a primary light microstructure in DZ-6 also is visible in the SEM micrographs in Figs. 10e-j. Explanation of the intensification of the austenite also can be made based on the pseudo-binary diagram in Fig. 8, in which the solution treatment temperature (1150°C) lies in the autenization area and allows space for austenite expansion. However, the high percentage of ferritizers and $MnO\text{-}SiO_2$ inclusions in some areas do not allow the austenite to grow extensively. It also is important to note that the solution treatment at temperatures above 700°C for long periods will allow sigma to fully transform to δ-ferrite. Thus, one can say that the brittle sigma phase almost completely disappeared in the HT specimen. Comparing the SEM macrograph of the AB sample (Fig. 7b) to the SEM macrograph of the HT sample (Fig. 10b) illustrates how heat treatment could help transform a porous, imbalanced DZ into a consistent microstructure with a meager fraction of micropores. As was discussed earlier, reheating helps relieve a considerable fraction of the micropores. Therefore, the isothermal tempering step contributes to a rearranged recrystallization in which a great amount of the micropores are disappeared. In summary, the DZ of the HT sample primarily contains austenite and δ-ferrite, and the sigma phase is completely dissolved. Although the two constitutive phases are fairly in balance in DZ-1, the volume fraction of austenite increases gradually when moving towards the upper layers from DZ-1 to DZ-6. Heat treatment, as expected, generally could transform the DZ from a porous medium into a solidified, impermeable region by removing a significant fraction of the existing micropores. Even so, the existing microcracks in DZ-1 are intensified after heat treatment, which can have an adverse effect on the fatigue performance of the repaired rail.

Comparing Figs. 6a and 6b to Figs. 9a and 9b show that there is no discernible HAZ in the HT sample, neither with the naked eye (Fig. 9a) nor when using a microscope (Fig. 9b); it is literally split into two regions of rail and DZ, without any transition region in between. The related OM and SEM micrographs of the former location of HAZ in Figs. 9d and 10d, respectively, show a microstructure that is quite close to that of the HT rail zone (Figs. 9c and 10c). However, in HAZ compared to the rail zone, it clearly can be distinguished that the volume fraction of the deep-dark martensite has decreased and that the volume fraction of the semi-dark austenite has increased. Besides, the light-etched bainite is obviously more condensed in HAZ than it is in the rail region. Precipitated carbide particles throughout the bainitic matrix also are visible in Fig. 10d. Comparing the chemical composition of the HAZ of the HT sample (Table 4) with that of the AB sample (Table 3) shows that the leading ferritizing elements of Cr and Si have decreased, but the

austenizing Ni, C, and N have increased as a result of the heat treatment. Hence, this fact indicates why the primary ferrite HAZ (Fig. 6d) is switched to a bainitic structure that contains a massive amount of austenite (Fig. 9d). Regarding the grain size, the heat treatment has noticeably coarsened the grain structure of the HAZ. The aggregation of micropores also is apparent in this zone (Fig. 10d) as was the case in the rail zone. The reasons for this were discussed earlier when the HT rail area was analyzed.

3.2. Heavy rail

3.2.1. SAW-repaired heavy rail

Optical Microscope (OM) captures from the etched specimen, that is extracted from the repaired rail, are shown in Fig. 12. In Fig. 12a, the etched specimen is divided into three areas of weld, heat-affected zone (HAZ), and rail. It is seen in Fig. 12b that the weld area contains four layers with different compositions/orientations in microstructure. A closer look into the microstructure of the fourth, third, second, and first weld layers are shown in Figs. 12c, 12d, 12e, and 12f, respectively. Close-up OM captures from the HAZ and rail can be found in Figs. 12h and 12j, respectively. The interfaces between weld and HAZ and between HAZ and rail are contained in Figs. 12g and 12i, respectively. The distribution of the chemical elements throughout the examined areas in Fig. 12 are given in Table 5.

Table 10 Chemical composition (wt.%) of different areas of the repaired rail

Area	Fe	C	Cr	Mn	Mo	Si
Layer 4	Bal.	0.067 ± 0.007	0.32 ± 0.05	1.25 ± 0.20	0.82 ± 0.03	3.42 ± 0.40
Layer 3	Bal.	0.028 ± 0.007	0.39 ± 0.05	1.93 ± 0.20	0.80 ± 0.03	3.26 ± 0.40
Layer 2	Bal.	0.016 ± 0.007	0.41 ± 0.05	2.55 ± 0.20	0.73 ± 0.03	3.12 ± 0.40
Layer 1	Bal.	0.017 ± 0.007	0.47 ± 0.05	2.19 ± 0.20	0.73 ± 0.03	2.94 ± 0.40
HAZ	Bal.	0.23 ± 0.06	0.12 ± 0.01	1.01 ± 0.20	0.03 ± 0.01	0.53 ± 0.40
Rail	Bal.	0.80 ± 0.06	0.03 ± 0.01	0.23 ± 0.03	-	0.04 ± 0.01

A dendritic thin lamellar pearlite microstructure is detectable for the rail in Fig. 12j. The rail microstructure obviously contains coarse, light islands of pro-eutectoid ferrite and dark-etched, dendritic pearlite lamellae that are randomly oriented. Sporadic signs of dissipated carbides are also traceable over the pearlitic-ferritic matrix.

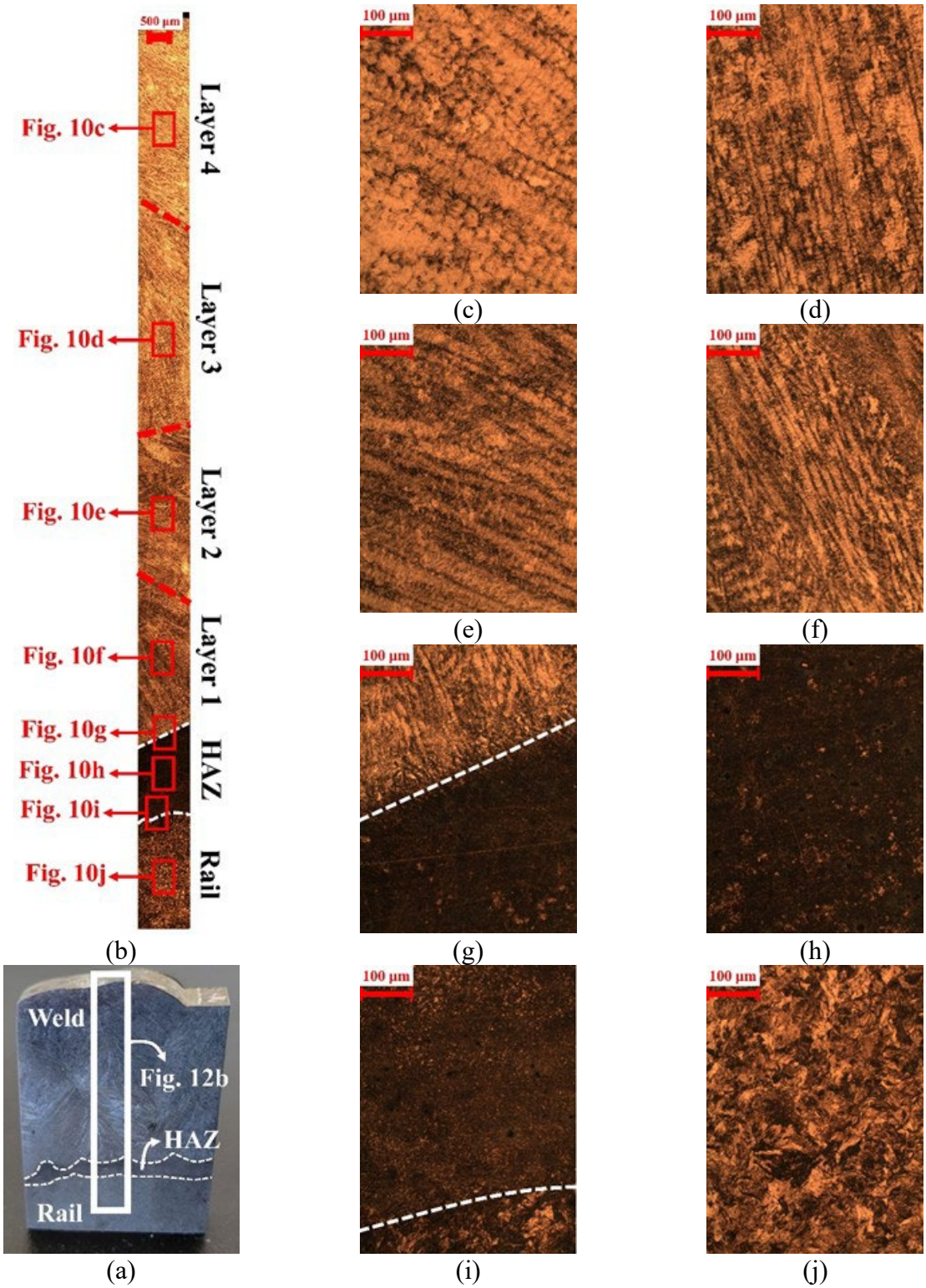

Fig. 3.12 (a) An etched specimen extracted from the head of the repaired rail, (b) A thorough OM capture from the entire weld zone with the four layers deposited, the heat-affected zone (HAZ), and the rail; closer OM shots are taken from (c) fourth, (d) third, (e) second, and (f) first weld layers, (g) weld-HAZ interface, (h) HAZ, (i) HAZ-rail interface, and (j) rail.

Per Fe-Cr phase diagram shown in Fig. 13, the utilized Lincore 40-S weld wire with around 0.5 weight percentage (wt.%) of chromium (referring to Sec. 2.1.2, Table 3) has a mixture of BCC phases containing Fe-rich (BCC) and Cr-rich (BCC') alloy compounds at room temperature. The general BCC phase of the weld material is observed and approved during the XRD analysis, as will be presented in the Residual Stress Measurement chapter, i.e., Chapter 5. A linked investigation of the Fe-Cr phase diagram in Fig. 13 and the chemical distribution in Table 5 offers the fact that for the four weld layers, with a Cr-wt.% interval of 0.32 to 0.47, there is no chance of austenite (γ) formation. The γ loop falls between 0 to 0.12 wt.% of Cr content, which is not contained in the interval of current case study. Hence, it is guaranteed that none of the distinguished phases in the OM morphology represent any austenite. A close inspection of the weld layers in Figs. 12c to 12f suggests three discernible regions, primarily categorized based on their brightness appearances. The light region represents the Alpha-ferrite (α-Fe) phase, the dark network stands for the acicular Alpha-chromium (α-Cr) phase, and the brittle sigma (σ) phase is appeared as a semi-dark zone. A general rule of thumb that can be attributed to the Fe-Cr phase diagram is that as the Cr-wt.% increases from 0 to 1, a light-etched to dark-etched transition occurs; the austenite with the lightest appearance in a HCL-etched carbon steel nucleates at $0 \leq$ Cr-wt.% < 0.12, then, at Cr-wt.% ≥ 0.12, a combined α-Fe + α-Cr phase forms which starts with the dominancy of the light-etched α-Fe at Cr-wt.% = 12 and smoothly transforms to a dark-etched, α-Cr-dominant compound as the Cr-wt.% leans towards 1. Table 5 shows a declined flow of Cr-wt.% from Layer 1 to Layer 4. As the first layer is welded on the railhead surface – with the liquidus weld drops at 1600-1700°C and the preheated railhead surface at 200-300°C – the weld materials start to experience an initially fast cooling procedure down to 500-700°C; a temperature range in between with closer tendency to the railhead temperature as this is a bigger bulk material. It then remains at that temperature interval for a while. Anyway, once the second layer is started to weld on top of the first layer, Layer 1 is reheated and has a chance for long exposure at a higher temperature range, i.e., 700-1000°C. In the meantime, Layer 2, with a higher initial substrate temperature at the time of starting deposition, i.e., 500-700°C, also remains at elevated temperatures around 700-1000°C until the third layer starts to get welded on top of it. This trend proves the fact that the top layers are exposed to higher ranges of temperature, i.e., higher than 500-800°C. Based on Fig. 13, for the utilized Fe-Cr weld alloy where Cr-wt.% is measured to be in the 0.32-0.47 range, long exposures to 500-800°C gives enough time for a α→σ transition. The longer the exposure time, the higher fraction of α would have the opportunity for transforming to the brittle σ. Besides, higher wt.% of Cr, i.e., closer to 0.47, leads to higher chance of complete α→σ transition at 500-800°C, while lower Cr-wt.%, i.e., closer to 0.32, yields to partial α→σ transformation. In other words, higher wt.% of Cr results in higher precipitated σ, but lower Cr-wt.% gives lower fraction of the brittle σ phase in the final microstructure. This fact clearly explains why the fraction of the semi-dark σ area decreases as we move from Layer 1 (Fig. 12f), to Layer 2 (Fig. 12e), to Layer 3 (Fig. 12d), and to Layer 4 (Fig. 12c). Layer 1 with higher reheating opportunities had longer available time to stay at 500-800°C and undertake the α→σ transformation process. As we move to the upper layers, the number of reheating opportunities decreases, the length of the 500-800°C exposure time decreases, hence the chance of α→σ decreases, and therefore lower fraction of brittle σ remains in the final microstructure at room temperature. Another discernible fact is that as the Cr-wt.% decreases from Layer 1 to Layer 4 (see Table 5), the volume fraction of the Cr-rich α, i.e., α-Cr, decreases and that of the Fe-rich α, i.e., α-Fe, increases. Therefore, Layer 1, with the highest Cr-wt.% among the four weld layers, contains the highest dark α-Cr volume fraction (Fig. 12f), and

Layer 4, with the lowest Cr-wt.% among the four weld layers, includes the lowest dark α-Cr volume fraction (Fig. 12c). Another contributor to the increment of the ferrite phase in the upper layers is that the wt.% of the ferrite stabilizers (Mo and Si) have an increasing trend from Layer 1 to Layer 4 (Table 5). This hence describes the increasing of the light-etched α-Fe area from the first layer (Fig. 12f) to the fourth (Fig. 12c).

When layers of materials are welded on the top of a substrate, the sandwiched HAZ, based on the findings of Shen et al. [4], contains a combined mixture of the weld and the substrate materials. On one hand, based on Fig. 12g, as we go down from weld to the HAZ, concentration of α-Cr increases and α-Fe is dissipated throughout the dark α-Cr matrix. It is seen in Table 5 that the ferritizers, i.e., Mo and Si, experience a significant descend from Layer 1 downwards to the HAZ; therefore, in their absence, α-Fe does not have enough stability and easily dissipates in favor of α-Cr. On the other hand, referring to Fig. 12i, moving upward from rail to the HAZ, the dark pearlite has been segregated and moved on to the HAZ, but a minor fraction of the pro-eutectoid ferrite could successfully migrate through to the HAZ. Hence, the core of the HAZ, as observable in Fig. 12h, is majorly consisted of pearlite and α-Cr, with dark appearances, and contains a minor fraction of ferrite with light appearance.

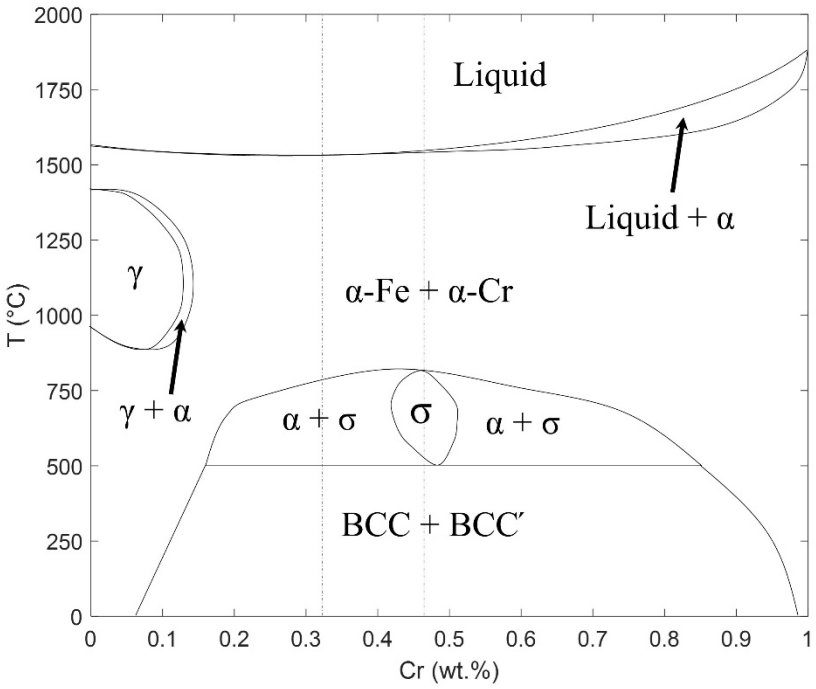

Fig. 3.13 Fe-Cr phase diagram for the Lincore 40-S hard-facing wire used in the SAW process

References for Chapter 3

[1] S. Kou, Welding metallurgy, John Wiley & Sons Inc. (2002) ISBN: 978-0-471-43491-7

[2] S.S. Babu, S.A. David, M.A. Quintana, Modeling microstructure development in self-shielded flux cored arc welds, Weld J. 80 (2001) 91–97.

[3] D. Li, G.Q. Gou, Y. Liu, T.H. Zhu, H. Ji, H. Chen, Effect of Al on microstructure and impact property of surfacing repair layer of rail, Surf. Eng. 28(7) (2012) 548–553. https://doi.org/10.1179/1743294411Y.0000000078.

[4] L. Shen, J. Zhou, X. Ma, X.Z. Lu, J.W. Tu, X. Shang, F. Gao, J.S. Zhang, Microstructure and mechanical properties of hot forging die manufactured by bimetal-layer surfacing technology, J. Mater. Process. Technol. 239 (2017) 147–159. https://doi.org/10.1016/J.JMATPROTEC.2016.08.020.

[5] N. Mori, H. Homma, S. Okita, M. Wakabayashi, Mechanisms of notch toughness improvements in weld metals containing Ti and B, J. Japan Weld. Soc. 50(2) (1980) 174–181. https://doi.org/10.2207/qjjws1943.50.174.

[6] N.A. Fleck, O. Grong, G.R. Edwards, D.K. Matlock, The role of filler metal wire and flux composition in submerged arc weld metal transformation kinetics, Welding (1986) 113s–121s.

[7] N. Fonstein, Advanced high strength sheet steels, Springer (2015) ISBN: 978-3-319-19165-2.

[8] U.P. Singh, B. Roy, S. Jha, S.K. Bhattacharyya, Microstructure and mechanical properties of as rolled high strength bainitic rail steels, Mater. Sci. Technol. 17(1) (2001) 33–38. https://doi.org/10.1179/026708301101509098.

[9] D. López, W. Schreiner, S. de Sánchez, S. Simison, The influence of carbon steelmicrostructure on corrosion layers: an XPS and SEM characterization, Appl. Surf. Sci. 207(1–4) (2003) 69–85. https://doi.org/10.1016/S0169-4332(02)01218-7.

[10] M. Santofimia, L. Zhao, J. Sietsma, Microstructural evolution of a low-carbon steel during application of quenching and partitioning heat treatments after partial austenitization, Metall. Mater. Trans. A 40(46) (2008) 46–57. https://doi.org/10.1007/s11661-008-9701-4.

[11] J.W. Fu, Y.S. Yang, J.J. Guo, J.C. Ma, W.H. Tong, Microstructure evolution in AISI 304 stainless steel during near rapid directional solidification, Mater. Sci. Technol. 25 (8) (2009) 1013–1016. https://doi.org/10.1179/174328408X317093.

[12] T.B. Massalski, A.J. Parkins, J. Jaklovski, Extension of solid solubility during massive transformation, Metall. Mater. Trans. B 3 (1975) 687–694. https://doi.org/10.1007/BF02642752.

[13] M.O. Malone, Sigma and 885°F embrittlement of chromium-nickel stainless steel weld metals, Weld. J. 46 (6) (1967) 241–253.

[14] E. Foroozmehr, R. Kovacevic, Thermokinetic modeling of phase transformation in the laser powder deposition process, Metall. Mater. Trans. A 40 (8) (2009) 1935–1943. https://doi.org/10.1007/s11661-009-9870-9.

[15] N. Suutala, T. Moisio, Use of chromium and nickel equivalents in considering solidification phenomena in austenitic stainless steels, Solidification Technology in the Foundry and Casthouse (1983) 310–314.

[16] G. Pacary, M. Moline, J.C. Lippold, A diagram for predicting the weld-solidification-cracking susceptibility of pulsed-laser welds in austenitic stainless steels, Edison Welding Institute, Research brief (1990) B9008.

[17] D. López, W. Schreiner, S. de Sánchez, S. Simison, The influence of carbon steel

microstructure on corrosion layers: an XPS and SEM characterization, Appl. Surf. Sci. 207(1–4) (2003) 69–85. https://doi.org/10.1016/S0169-4332(02)01218-7.
[18] K. Takano, R. Nakao, S. Fukumoto, T. Tsuchiyama, S. Takaki, Grain size control by oxide dispersion in austenitic stainless steel, Tetsu to Hagane – J. Iron Steel Inst. Jpn. 89(5) (2003) 616–622. https://doi.org/10.2355/tetsutohagane1955.89.5_616.
[19] Y. Ren, L. Zhang, P.C. Pistorius, Transformation of oxide inclusions in type 304 stainless steels during heat treatment, Metall. Mater. Trans. B 48(5) (2017) 2281–2292. https://doi.org/10.1007/s11663-017-1007-8.

4. CHAPTER 4 HARDNESS MEASUREMENT OF THE REPAIRED RAIL

4.1. Light rail

4.1.1. SAW-repaired light rail

To evaluate hardness distribution at different zones including weld zone (WZ), heat-affected zone (HAZ), and rail, hardness measurement is taken on the cross section of the rail sample along three lines. Major and minor loads of 90 kgf and 10 kgf are incorporated, respectively, for the B-scale Rockwell hardness test in this study. The three aforementioned lines are employed based on AREMA test plan recommendation [1], as shown in Fig. 1a.

The hardness distribution for the as-built (AB) sample along left gauge line (Line 1), right gauge line (Line 2), and the middle line (Line 3) are shown in Fig. 1b. The minimum required hardness given by AREMA for light-duty rails [1] is also depicted as a red dashed line in Figs. 1b to 1d. The different zones of the AB rail are apparent based on the variation of hardness along the corresponding lines. The average hardness for Lines 1, 2, and 3 in the WZ area are 80.4 HRB, 78.5 HRB, and 81.5 HRB respectively. It can be seen that the gauges are slightly harder than the middle section. Similarly, the average measured hardness along Lines 1, 2, and 3 in the HAZ area are 93.1 HRB, 91.2 HRB, and 94.92 HRB, respectively. The unaffected rail substrate shows an average hardness value of 95 HRB. As it is evident in Fig. 1b, the hardness in the WZ increases gradually from top of the AB railhead down to the WZ/HAZ interface. Sec. 3.1.1, Fig. 1 shows a descending trend of austenite from WZ1 downwards to WZ3, which justifies the rising trend of hardness from top of the weld zone down to the WZ/HAZ interface. Sec. 3.1.1, Fig. 1 also presents the increase of pearlite volume fraction fromWZ2 to WZ3, which again confirms the higher hardness value in WZ3. It can be observed from Sec. 3.1.1., Fig. 1 that the HAZ has a considerable finer grain structure compared to both the WZ and the rail. This fact along with the great density of carbide precipitations in this zone makes the HAZ the hardest zone among all the areas of the AB sample as shown in Fig. 1b. The coarse-grain pearlitic-ferritic microstructure of the rail zone with moderate mass of carbides gives a medium hardness value for this region. It is clearly observable in Fig. 1b that the overall hardness of the AB rail is below the minimum AREMA requirement.

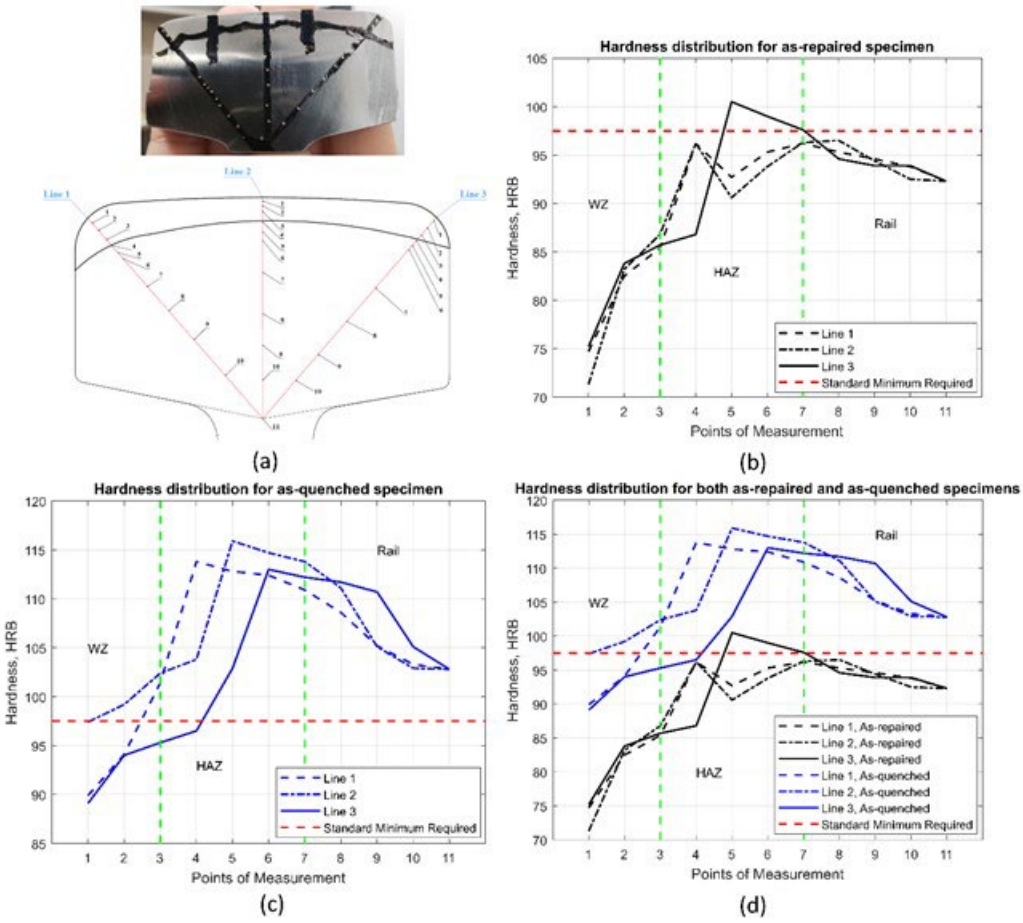

Fig. 4.1 (a) Hardness test plan showing the lines along which hardness is measured on the demonstrated points; (b) hardness distribution for the as-built (AB) sample; (c) hardness distribution for the as-quenched (AQ) sample; (d) putting both the AB and AQ hardness distribution results together (the red dashed line represents the minimum acceptable hardness for light-duty rail, assigned according to AREMA's standards [1]).

Fig. 1c illustrates hardness distribution of the AQ specimen. The average hardness in the WZ area varies from 95.1 HRB to 99.6 HRB, and then to 92.8 HRB for Lines 1, 2 and 3, respectively. With regard to the HAZ, the hardness is measured as 110.3 HRB, 110.1 HRB, and 103.9 HRB for Lines 1, 2, and 3, respectively. The average hardness of the rail is increased to 106 HRB. Therefore, heating up the AB rail sample to 1100 °C and water-quenching causes a noticeable increase in hardness in all areas of the sample (about 26%).

Comparing the AB and AQ samples zone-by-zone, it can be observed that residual austenite in WZ1 in the AB sample (Sec. 3.1.1., Fig. 1c) has disappeared and a massive amount of carbides are precipitated in this region (Sec. 3.1.1, Figs. 4c and 5c). The same observation can be attributed to WZ2. In addition, the ferrite volume fraction has been remarkably increased in WZ2 in the AQ sample (Sec. 3.1.1, Fig. 4d) compared to the AB sample (Sec. 3.1.1, Fig. 1d). The removal of austenite, the exceptional increase in carbide particles, and the growth in pearlite volume fraction are the major contributors of increasing hardness in WZ1 and WZ2 as a result of quenching. A

transformation from coarse-grain (Sec. 3.1.1, Fig. 1e) to a fine-grain microstructure (Sec. 3.1.1, Fig. 4e) plus carbide precipitation and additional pearlite nucleation in WZ3 (Sec. 3.1.1, Figs. 4e and 5e) made this zone harder after quenching. Regarding HAZ, the nucleation of martensite in this area after quenching (Sec. 3.1.1, Figs. 4f and 5f) that did not exist in the same area in the AB sample (Sec. 3.1.1, Fig. 1f) and the growth of carbide precipitations in this area after quenching (Sec. 3.1.1, Fig. 5f) rather than before quenching (Sec. 3.1.1, Fig. 2f) justifies the excessive increase of hardness in this zone. The same justification for hardness raise in HAZ can be applied for the rail zone.

The achieved hardness for the AQ sample is still below the minimum required hardness which is equal to 97.5 HRB and is illustrated in a dashed red line in Fig. 6d, where all the results of the quenched and non-quenched samples are put together for comparison purposes. To improve the hardness, the current weld wire can be substituted with a homemade one containing more carbon content. The average hardness at the gauges was lower than the middle zone before quenching, but then increased to higher than that of the middle zone. This can be caused by the faster cooling rate at the gauges during the quenching process due to the greater area of exposure.

There is an inversed correlation between hardness and wear rate: higher hardness gives lower wear rate [2,3]. Although increasing hardness desirably reduces the wear rate, superior hardness leads to brittleness and cracking. Initiation of martensitic phase in the microstructure of the deposited surface brings crack propagation in virtue of the brittle nature of martensite micro-constituent compared to any other materials with the same carbon content [4,5]. In this way, despite the fact that a homemade high-carbon flux-cored arc wire using SAW process for rail repair is encouraged, it is not recommended to use martensitic wire. The other concern is the increasing of pore concentration in the microstructure which could cause crack initiation and early failure. To mitigate this problem, tempering or quenching and processing (Q&P) are recommended. Nonetheless, it should be noted that these processes can lead to a decreased hardness and make the rail more susceptible to wear.

4.1.2. LPD-repaired light rail

Hardness is evaluated from the topmost deposited layer in the deposition zone (DZ) which is the sixth deposition layer (DZ-6) downwards to a depth of 7 mm in a way to cover all of the studied zones, including DZ, HAZ, and rail. Figs. 2a and 2b, respectively, show the measured hardness distribution for the as-built (AB) and heat-treated (HT) samples. The hardness of each zone is measured nine times at nine different sampled locations of the repaired rail, and the presented values in Fig. 2 are the average measured hardness at each zone. The red dashed line in Fig. 2 shows the minimum required hardness for standard U.S. light rails, 97 HRB, as assigned by AREMA [1].

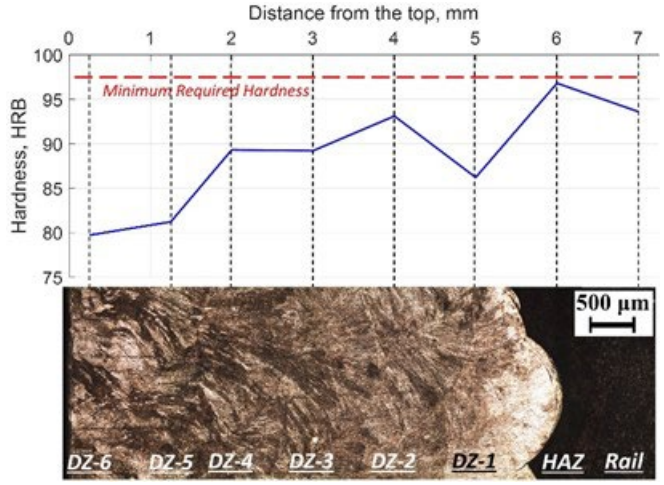

(a)

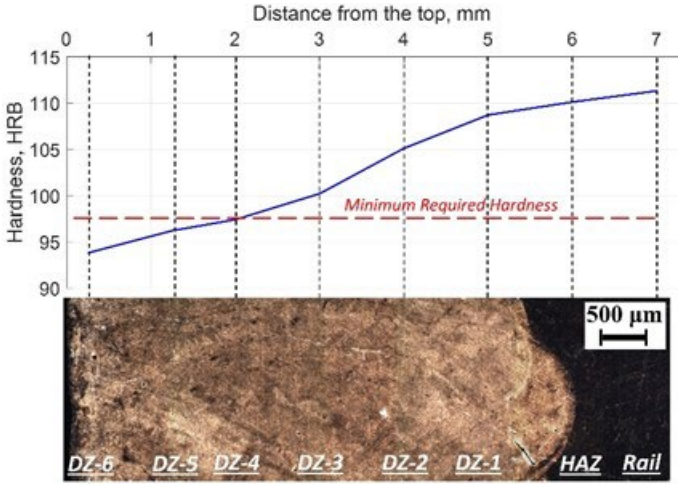

(b)

Fig. 4.2 Hardness distribution: (a) in the as-built (AB) rail; (b) in the heat-treated (HT) rail. The red dashed lines represent the minimum required hardness for standard U.S. light rails assigned by AREMA [1].

Fig. 2a clearly shows that the hardness of the AB sample is thoroughly below the minimum requirement. The minimum hardness (~80 HRB) occurs in DZ-6 and DZ-5, which have a primary austenite microstructure. Based on Fig. 2a, going from DZ-5 to DZ-4, the hardness is increased dramatically, from 80 to around 90 HRB (about a 12.5% increase), which, for the most part, can be attributed to the transition of the microstructure from primary austenite (Sec. 3.1.2, Fig. 6i) to primary ferrite (Sec. 3.1.2, Fig. 6h). The intrusion of the brittle sigma phase in DZ-4 is the second determining factor for such a considerable increment. The hardness continues to increase from DZ-4 to DZ-2 due to the increase of the sigma volume fraction along this path (Sec. 3.1.2, Fig. 6h to 6g to 6f). Although sigma also continues to increase from DZ-2 (Sec. 3.1.2, Fig. 6f) to DZ-1 (Sec. 3.1.2, Fig. 6e), the primary microstructure switches back from ferrite to austenite, which has

a more decisive effect on the value of hardness than the effect of sigma growth. This ultimately results in a 6% reduction of hardness from 93 HRB in DZ-2 to 87 HRB in DZ-1. The austenite-to-ferrite changeover and also the increase in the value of sigma from DZ-5 to DZ-4 both contributed to the increased hardness. But, from DZ-2 to DZ-1, while the ferrite-to-austenite transition reduces the hardness somewhat, the sigma volume fraction increment tries to increase the hardness, although not as strong as the hardness reducer parameter. Therefore, the decrease in the hardness from DZ-2 to DZ-1 is not as sharp as the increase in the hardness from DZ-5 to DZ-4. The maximum hardness is reached at HAZ, where an alteration occurs from primary austenite at DZ-1 to a fine pearlitic-ferritic network at HAZ, so the hardness increases from 87 to 96 HRB. Fig. 2a shows that there is no significant difference between the hardness of the rail zone and the hardness of HAZ. Both of them consist of a ferrite-pearlite network (Sec. 3.1.2, Figs. 6c and 6d), but the rail has a coarse-grain microstructure and consequently has a relatively lower hardness than the fine-grain HAZ.

The hardness distribution of the HT sample in Fig. 2b shows how effectively the employed heat treatment increased the hardness throughout the repaired rail. The hardness values generally are shifted to higher amounts than the minimum required, except for the two upper deposition layers of DZ-5 and DZ-6. The major reason for such an enhancement of hardness is the evolution from a coarse, inhomogeneous grain structure (Sec. 3.1.2, Figs. 6e-j) to a fine, homogenous structure (Sec. 3.1.2, Figs. 9e-j). All of the HT deposition layers have an austenite-ferrite microstructure. A clear conclusion from Fig. 2b is that there is an inverse correlation between the volume fraction of austenite and the hardness values; DZ-6 with the highest austenite volume fraction (Sec. 3.1.2, Fig. 9j) has the lowest hardness of 94 HRB, and DZ-1, with the minimum volume fraction of austenite (Sec. 3.1.2, Fig. 9e) has the maximum hardness, i.e., 108 HRB, among the deposition layers. In more general terms, the gradual deterioration of austenite from DZ-6 downwards to DZ-1 has led to a steady increase in hardness along the same path. Another affirmation of the homogenizing effect of heat treatment is the uniform distribution of hardness between DZ-1, HAZ, and the rail zone in the HT sample in Fig. 2b without any sign of harsh fluctuations such that occurred for the AB sample in Fig. 2a. HAZ and rail zone in the HT specimen are slightly harder than DZ because of the martensitic microstructure (Sec. 3.1.2, Figs. 9c and 9d) and the precipitated carbides (Sec. 3.1.2, Figs. 10c and 10d).

There is an inverse relationship between hardness and wear rate, which means that the higher the hardness becomes, the lower the wear rate becomes. However, excessive hardness will result in brittleness, which increases the cracking susceptibility. Therefore, the existence of martensite in the final rail microstructure is banned by AREMA standards because of the brittle characteristic of this constituent, which would result in the early initiation and propagation of cracks. The promising result of the current case study is that the deposition materials on the top of the rail are free of martensite. Also, although the hardness of the upper deposition layers is slightly lower than the minimum required (~2%), the overall hardness of the deposition materials is at an acceptable level. The heat treatment could deliver a fine grain structure in the deposition area with a minimum concentration of micropores. Even so, the HT substrate has two adverse characteristics, i.e., 1) its martensitic microstructure (Sec. 3.1.2, Fig. 9c) and 2) a considerable accumulation of coarse micropores (Sec. 3.1.2, Fig. 10c). Although the rail substrate will not be in direct tribological contact with the wheels of the train and, hence, is not a primary matter of concern, a porous, brittle microstructure is significantly susceptible to early cracking under dynamic train loads. Aside from

all of these concerns, the major concern about the final product is the presence of detrimental cracks at the rail-deposition interface. Propagation of these cracks under dynamic loads will lead to premature failure and delamination of the deposited steel.

To conclude, the ultimate outputs of LPD repairing the standard 75-lb U.S. light rail using the austenitic 304L stainless steel seem promising regarding the microstructure and hardness properties. However, the developed martensite in the rail substrate and the initiated cracks at the rail-deposition interface are adverse occurrences. Prevention of the nucleation of martensite in the rail material can be achieved by isolating the rail substrate so that it is not heated during the post-heat treatment of the repaired rail. The crack initiation at the rail-deposition interface can be alleviated or eliminated by preheating the head of the worn rail as the LPD substrate. Evaluation of the recommended pre- and post-processing requires additional experimental studies to ultimately achieve a promising LPD rail repair process with minimum defects in the final product.

4.2. Heavy rail

4.2.1. SAW-repaired heavy rail

Per AREMA regulations [1], distribution of hardness along the three lines, shown in Fig. 3a, should be maximum at the surface of the railhead, i.e., points 1, 11, and 25 in Fig. 3a, and then undergo a smooth declination towards the minimum hardness at the root of the railhead, i.e., point 39 in Fig. 3a.

Fig. 3 gives the hardness distribution along the left gauge, middle, and right gauge of the repaired railhead, i.e., Lines 1, 2, and 3, respectively, in Figs. 3b, 3c, and 3d, respectively. The minimum required hardness assigned by AREMA [1] for heavy 136RE rails, which is equal to 32 HRC, is shown as a horizontal dash-dot line is all the graphs. The vertical dashed line in each graph locates the rail-weld interface. Therefore, the areas at the left side of the vertical dashed lines in Figs. 3b, 3c, and 3d represent the weld area, and the areas at the right stand for the rail area.

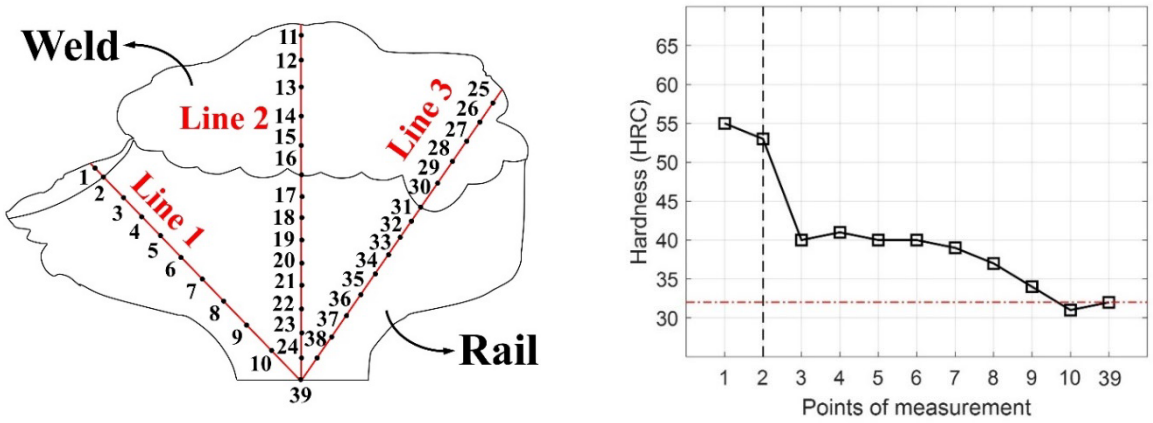

(a) (b)

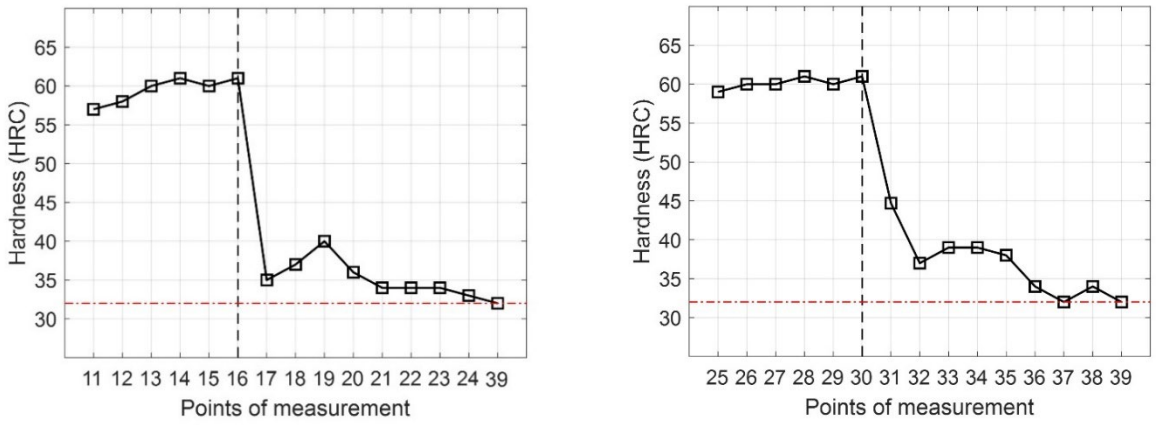

(c) (d)

Fig. 4.3 Hardness distribution on the head of the repaired rail showing the (a) hardness test plan and hardness distribution along (b) Line 1 (c) Line 2, and (d) Line 3; the vertical dashed line in all of the graphs located the rail-weld interface and the horizontal red dash-dot line shows the minimum acceptable hardness based on AREMA standards [1].

It is evident in Figs. 3b-d that the average measured hardness at the weld zone along Lines 1, 2, and 3 are 54, 59.5, and 60 HRC, respectively. The mean hardness measured in the rail section along Lines 1, 2, and 3 are 37, 35, and 36 HRC, respectively. Therefore, the overall hardness in the weld area is estimated as 58 HRC, and that of the rail area is 36 HRC. The results then imply that the hardness results meet the standard AREMA requirement in a way that the maximum occurs at the head and minimum occurs at the root of the repaired railhead, and the hardness of the repaired rail in almost all the regions is higher than the minimum required 32 HRC. However, it fails to meet the AREMA standards in the matter of a smooth declination from the maximum at the head to the minimum at the root; as the results tell and the graphs show in Figs. 3b-d, a sharp, step decrease of hardness happens at the rail-weld interface, moving from the weld area to the rail zone.

As it was shown and discussed in Sec. 3.2.1, the hardest phase present in the weld material is the brittle σ phase. Although the sigma phase can significantly contribute to increasing the hardness and, unlike martensite, is not against AREMA regulations to possess part of the railhead microstructure, it substantially affects the material ductility by increasing the brittleness, which raises the chance of premature cracking and failure of the rail under dynamic wheel-rail load. Therefore, while the quite higher hardness of the weld material than the minimum required (about 80% higher) seems satisfying, it might make the deposited weld too brittle and hence require some post-heat-treatment (e.g. tempering) to alleviate the hardness down to some values closer to the minimum 32 HRC. In this way, while the hardness still meets the minimum standards, the material becomes more ductile and decreases the chance of early cracking and premature failure. Another contributor phase to a high hardness in the weld zone is the α-Fe phase. It was discussed in Sec. 3.2.1 that as we move from lower weld layers close to the rail to upper weld layers at the top surface of the repaired rail, the volume fraction of σ decreases and that of the α-Fe increases. It can be then inferred that as one of the hardness-increment-contributors, i.e., σ, decreases in the upper layers, the other contributor, i.e., α-Fe, increases in volume fraction. This hence explains the almost constant, high hardness in the whole weld area, as visible in Fig. 3; the hardness of the weld zone remains between 55 to 60 HRC and no considerable fluctuation occurs.

As the hard α-Fe and the brittle σ phases disappear in the HAZ while the mild-hardness α-Cr increases, the hardness suddenly descends from 55-60 HRC to around 40 HRC. Thereafter, in the rail area with the standard pearlitic-ferritic phase, the hardness values match the standard expected values between 32 to 42 HRC, converging to 32 HRC at the root of the repaired rail (Fig. 3).

Thus, a proper choice of heat treatment, such as tempering, can dissolve the brittle σ phase and help towards augmentation of the ferrite phase in the weld zone. This microstructural transformation not only could make a consistent hardness distribution all over the repaired railhead, but it also could aid the hardness of the weld material to reduce to the standard 32-40 HRC interval.

4.2.2. LPD-repaired heavy rail

To evaluate hardness distribution at different zones including deposition zone, HAZ, and rail, hardness measurement is taken on the cross section of the AB sample along three lines. Major and minor loads of 90 kgf and 10 kgf are incorporated, respectively, for the B-scale Rockwell hardness test. The three aforementioned lines are employed based on AREMA test plan recommendation [1], as shown in Fig. 4a. The horizontal red dashed line in Figs. 4b, c, and d shows the minimum required hardness for standard U.S. heavy rails, 107 HRB, as assigned by AREMA [1]. The rail-deposition interface is located using a vertical green line in Figs. 4b, c, and d.

The average hardness for Lines 1, 2, and 3 in the deposition zone are 100 HRB, 99 HRB, and 102 HRB, respectively. It can be seen that the hardness of all of the areas of the deposited materials is considerably lower than the minimum required, i.e., 107 HRB. This is not a satisfactory result, and the repaired rail will definitely undergo a premature failure under the train load. In this way, this LPD-repaired heavy rail will certainly need a post-heat-treatment to increase the hardness at the deposition zone. Since the same 304L stainless steel that was used for LPD-repairing the light rail is used for the heavy rail as well, the same heat treatment will also be employed for increasing the hardness here. The heat-treatment process and measuring the results is under investigation at this time.

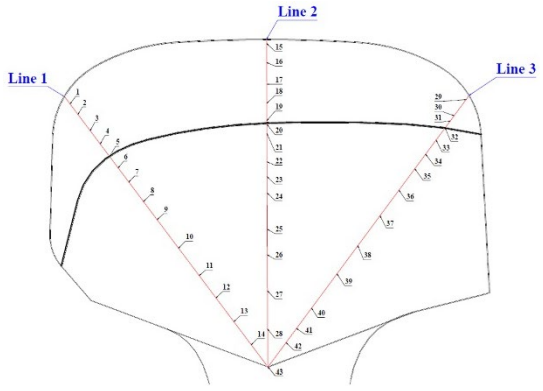

(a)

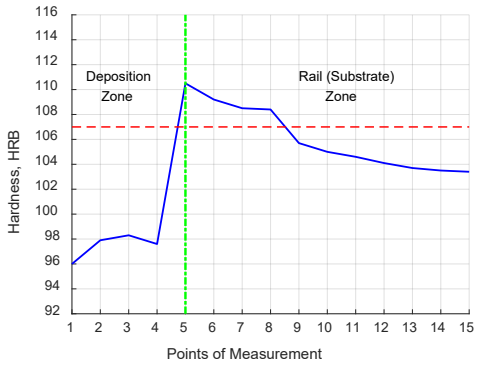

(b)

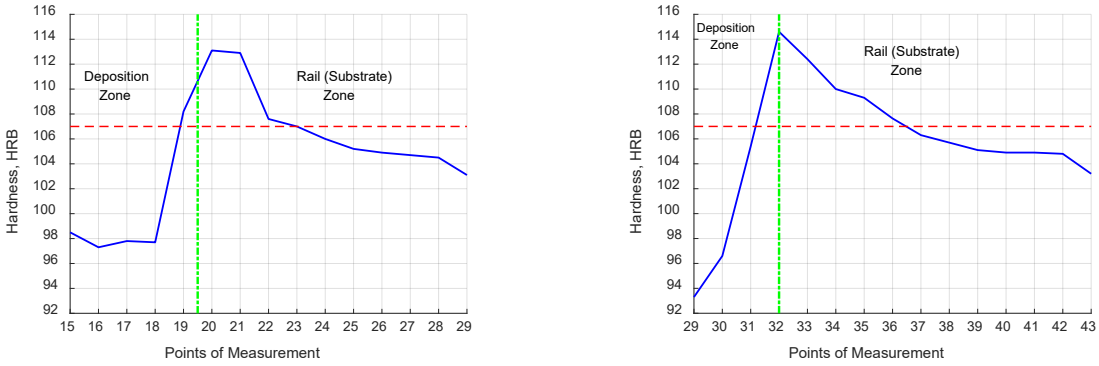

Fig. 4.4 Hardness test results from the as-built (AB) LPD-repaired heavy rail; (a) schematic map of the points and lines on which the hardness is measured; (b) hardness distribution along line 1, (c) line 2, and (d) line 3; the horizontal red dashed line represents the minimum acceptable hardness for heavy rails, assigned according to AREMA's standards [1], and the vertical green line represents the location of the rail-deposition interface.

References for Chapter 4

[1] AREMA Manual for Railway Engineering, Chapter 4: Rail, American Railway Engineering and Maintenance-of-way Association (2020).

[2] Y. Jin, M. Ishida, A. Namura, Experimental simulation and prediction of wear of wheel flange and rail gauge corner, Wear 271 (2010) 259–267. https://doi.org/10.1016/j.wear.2010.10.032.

[3] U. Tayfun, B. Witold, G. İbrahim, Wear and friction of composites of an epoxy with boron containing wastes, Polímeros 25 (2015). https://doi.org/10.1590/0104-1428.1780.

[4] W.D.Jr. Callister, Materials science and engineering: an introduction, 6th Edition, JohnWiley & Sons, Inc. (2002) ISBN 978-0-471-13576-0.

[5] G. Lacroix, T. Pardoen, P.J. Jacques, The fracture toughness of TRIP-assisted multiphase steels, Acta Mater. 56(15) (2008) 3900–3913. https://doi.org/10.1016/J.ACTAMAT.2008.04.035.

5. Chapter 5 RESIDUAL STRESS MEASUREMENT OF THE REPAIRED RAIL

5.1. Light rail

5.1.1. LPD-repaired light rail

In this section, the measured residual stresses will be presented based upon the coordinate system shown in Fig. 1. The dashed lines in Fig. 1 along x and z directions are seated at the rail-deposition interface. The origin is located at the center of the railhead surface; y = 0 plane intersects with the rail-deposition interface, and the top surface of the deposition part is located at y = 4 mm plane.

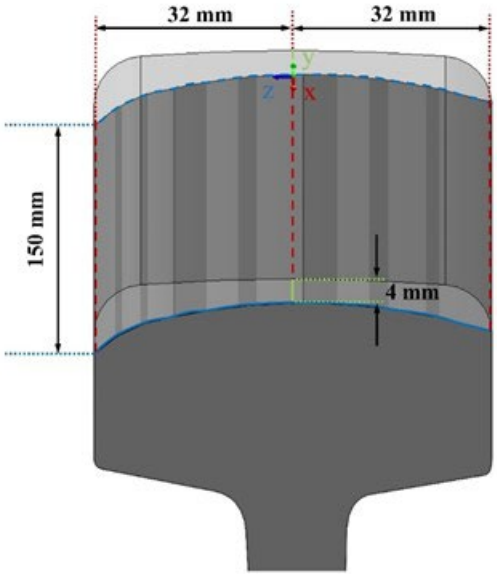

Fig. 5.1 Coordinate system upon which the results are presented for the LPD-repaired light rail.

The measurement of the residual stresses is conducted via XRD stress measurement technique. The running parameters of the XRD stress measurement setup are described in Sec. 2.3. To determine the proper 2θ angle for stress measurement, phase scan analysis is carried out to acquire the diffraction peak patterns of both the deposition and rail materials. The resulting diffraction peak patterns of the 304L deposition steel and C-Mn rail are shown in Figs. 2a and 2b, respectively. It is preferred to measure the residual stresses at high 2θ values, because the applied minor changes to the d-spacing, as a result of strain, are measured more precisely at higher angle range of 2θ [1]. Therefore, the FCC (3 3 1) peak at 2θ = 117.5° (Fig. 2a) for the deposition area and the BCC (2 2 2) peak at 2θ = 137.1° (Fig. 2b) for the rail area is picked for measuring the stress using the $\sin^2\psi$ method. The angular rotation of ψ angle for each stress measurement is started from ψ = 0°, and successive ψ offsets are added in a way to cover the $0° \leq \psi \leq 45°$ range with 5 equal intervals and a total number of 6 points of ψ. The 2θ measurement range for the deposition zone is from 115.1° to 119.9° and for the rail zone is from 135.1° to 139.1°. Sliding gravity technique is used for peak evaluation, and data correction is performed for background, absorption, and Lorentz polarization. The 2θ scans are operated with 0.02 increment, and a counting accumulation of 0.8 s/step is

incorporated.

In order to verify the XRD stress measurement accuracy, horizontal line profiles are taken from the specimen at its different stages, i.e., as-built (AB), as-polished (AP), and as-etched 1 (AE1). In the depicted profiles in Fig. 3, the horizontal dashed lines are the location of the median plane. As it can be seen in Fig. 3, the AB sample has a high roughness with around +/- 50 μm height/depth of the peaks/pits. For the AP sample, the distance of the peaks/pits from the median plane is considerably decreased to +/- 0.8 μm, which indicates a much smoother surface of the sample at the AP stage. The captured line profile from the AE1 sample shows almost the same roughness pattern and magnitude as that of the AP sample.

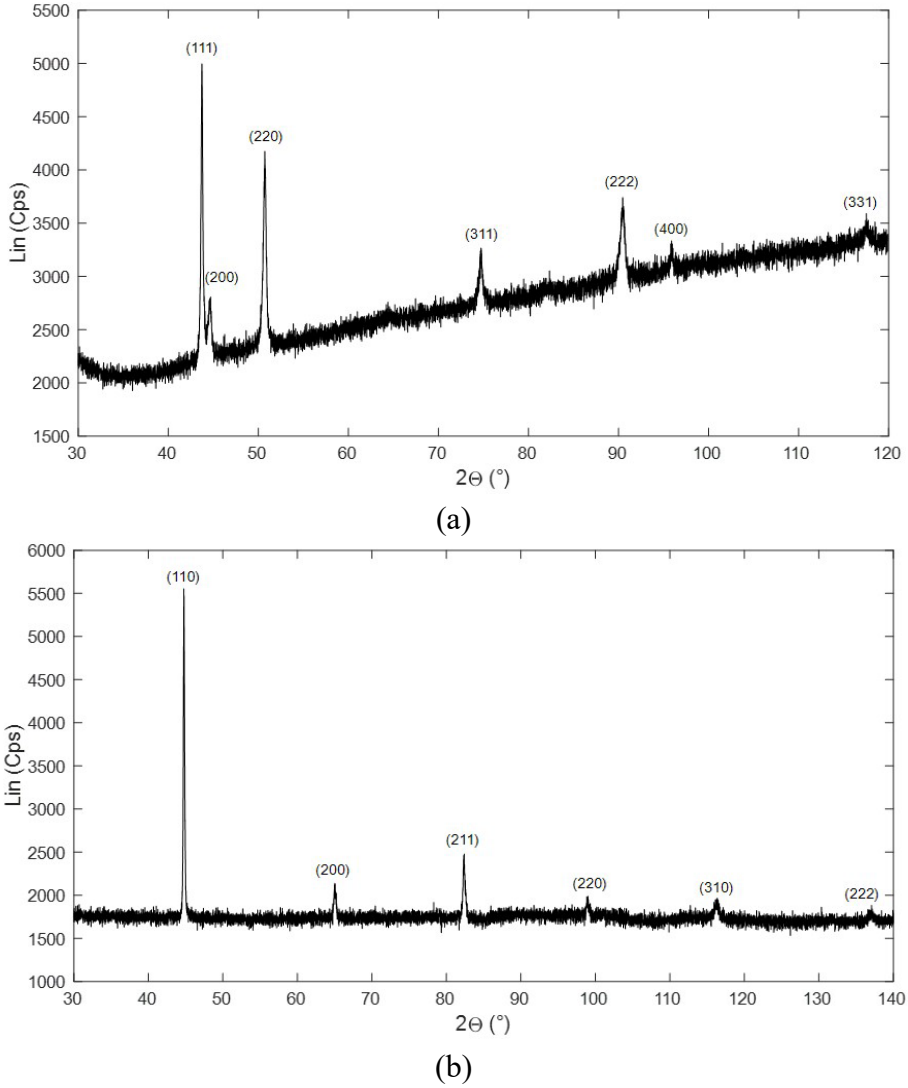

Fig. 5.2 Diffraction Peak Pattern through the full range of 2θ for (a) 304L deposition steel and (b) C-Mn light rail.

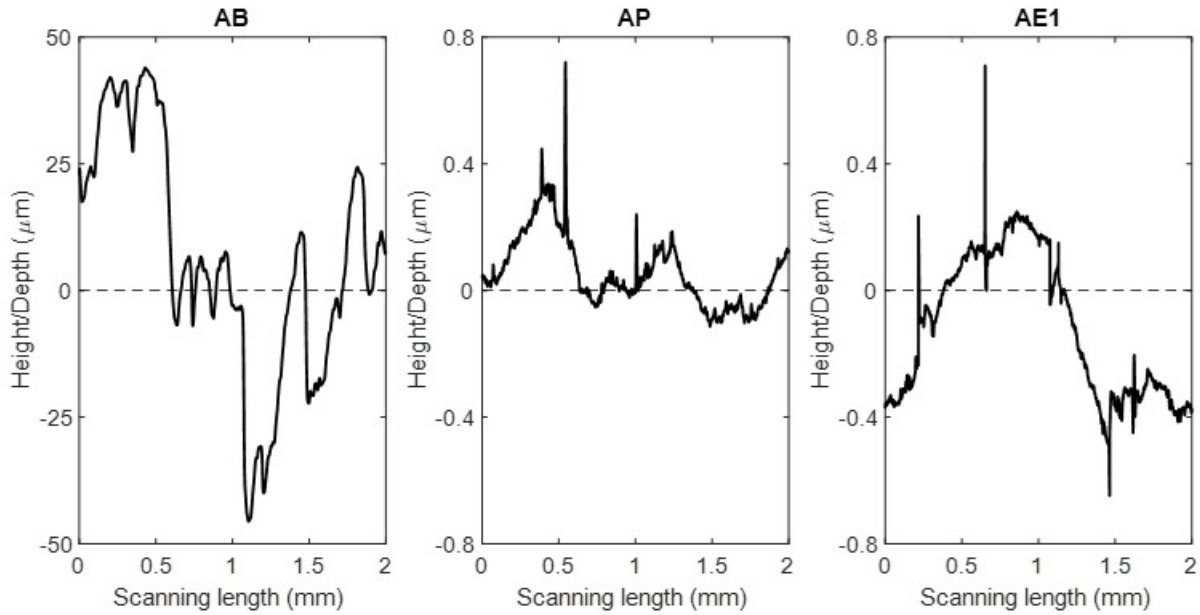

Fig. 5.3 Horizontal line profile from the surface of the repaired rail specimen at three different stages of as-built (AB), as-polished (AP), and as-etched 1 (AE1).

In conjunction with the line profile acquisition, residual stress of the specimen at its different stages, i.e., AB, AP, and AE1, is measured using XRD to ascertain that all of the measurement errors associated with the rough surface and the relaxed residual stresses on the surface as a consequence of polishing are eliminated. The measurement is continued to carry out on the further etched samples, i.e., AE2, AE3, AE4, and AE5. All of the measurements are conducted at the (x,y,z) = (20,3,13) mm (refer to Fig. 1 for configuration of the coordination system). The measurement results are shown in Fig. 4. It is also worth mentioning that mechanical polishing removed 750-μm thickness of the specimen materials, and every step of etching removed 50 μm of the specimen thickness. Fig. 4 shows the considerable effect of polishing on the measured stress values. For a CuKα radiation into the stainless steel, the X-ray beam penetration depth is about 5μm [2,3]. Therefore, for the rough AB sample with +/- 50 μm peaks/pits (Fig. 3 AB) where the surface contains spikes to a level of about 10 times higher than the X-ray penetration depth, interruption of the X-ray beam by those spikes will lead the XRD measurement to yield lower stress values than the actual. While it visually seems that consecutive layer removal through etching does not act as effectively as the polishing did in stabilizing the measured stress, there is about 8–16% difference in the measured stresses between the AP and the AE5 samples. According to Figs. 4a, 4b, and 4c, the σ_l, σ_t, and σ_n values keep on modifying until the fourth, third, and fourth steps of etching, respectively. Hence, it is concluded that after mechanical polishing and five steps of chemical etching, the acquired XRD stress profile is accurate enough, and all of the existing errors mentioned earlier are now eliminated. In this way, the AE5 specimen will be used for the rest of the XRD stress measurements.

Each of the longitudinal and transversal residual stresses is measured at four different points along x and z directions, respectively, at the rail-deposition interface. Normal residual stress measurement is taken along y direction at two points in the deposition zone, i.e., y = 1 mm and y = 3 mm, and two points in the rail zone, i.e., y = -3 mm and y = -5 mm (refer to Fig. 1 for

configuration of the coordinate system). The inter-planar spacing, d, versus $\sin^2\psi$ values is plotted for all the measuring points and is given in Fig. 5. The employed elastic constants for 304L deposition steel are E = 190 GPa and ν = 0.3, and those for C-Mn rail are E = 203 GPa and ν = 0.3. Evaluation of stress amounts is carried out using the assigned elastic constants along with the gradient of the curve fitting line from the d-$\sin^2\psi$ plots in Fig. 5. The resulting stress is given by the following equation [1]:

$$\sigma = m\left(\frac{E}{\nu + 1}\right) \tag{1}$$

where m is the gradient of the curve fitting line of the d-$\sin^2\psi$ plot. As it can be seen in Fig. 5c for y = -3 mm, the curve fitting line of this plot has a descending gradient, which gives a negative value to m and subsequently gives a negative (compressive) stress. All the measured stresses from the $\sin^2\psi$ analysis are given in Table 1.

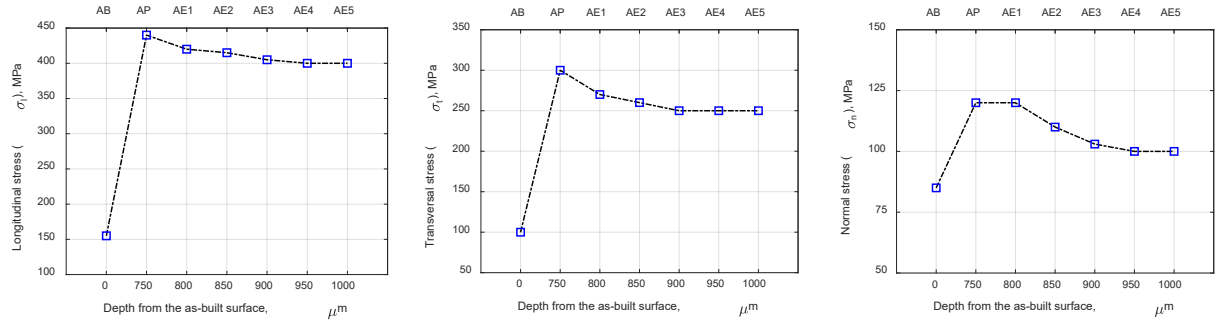

Fig. 5.4 The measured (a) longitudinal, σ_l, (b) transversal, σ_t, and (b) normal, σ_n, residual stresses via XRD at point (x,y,z) = (20,3,13) (See Fig. 1 for configuration of the coordination system) for different stages of sample preparation, i.e., as-built (AB), as-polished (AP), and five etching steps (AE1 to AE5).

Table 11 Measured residual stress values at different locations of the as-etched 5 (AE5) LPD-repaired rail sample (Refer to Fig. 1 for configuration of the coordinate system).

Location (x,y,z) (mm)	**σ_l (MPa)**	**Location (x,y,z) (mm)**	**σ_t (MPa)**	**Location (x,y,z) (mm)**	**σ_n (MPa)**
(20,0,0)	400	(0,0,-24)	200	(0,3,0)	96
(55,0,0)	320	(0,0,-12)	240	(0,1,0)	91
(95,0,0)	380	(0,0,12)	250	(0,-3,0)	-25
(130,0,0)	420	(0,0,24)	248	(0,-5,0)	12

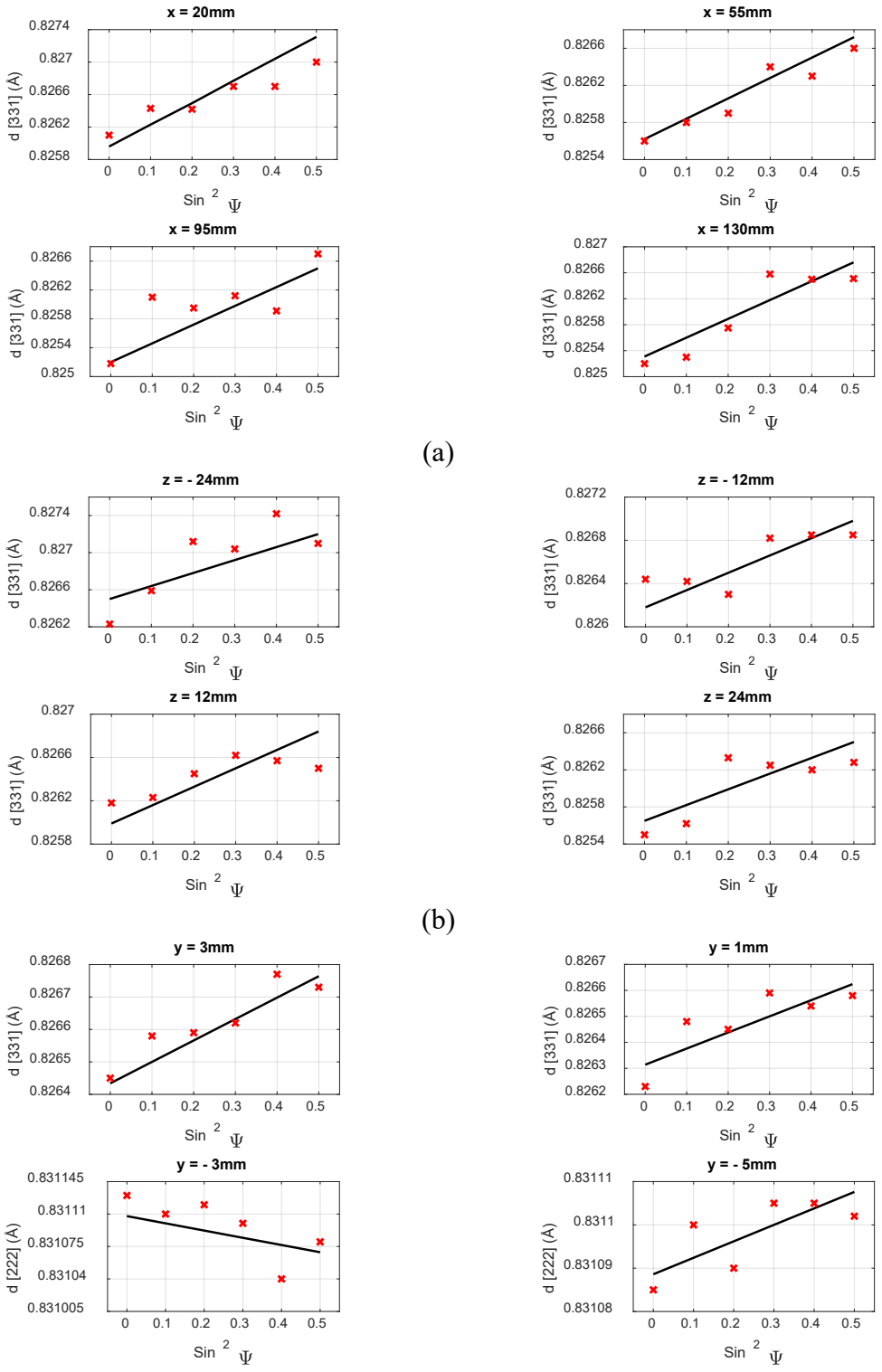

Fig. 5.5 Obtained plots of inter-planar spacing, d, versus $\sin^2\psi$ from XRD measurement of (a) σ_l at (z, y) = (0, 0), (b) σ_t along rail-deposition interface at x = 0 plane, and (c) σ_n at (x, z) = (0, 0). Refer to Fig. 1 for configuration of the reference coordination system.

5.2. Heavy rail

5.2.1. SAW-repaired heavy rail

Just as presented in Sec. 5.1.1, surface roughness of the sample is measured to make sure that it is less than 5 μm, i.e., X-ray penetration depth. This process will not be described here again.

A typical XRD phase scan analysis from the weld and rail materials are given in Figs. 6a and 6b, respectively. As it is intended to obtain a precise measurement of strain owing to lattice spacing variations, the residual stresses are recommended to be measured at the highest possible diffraction angles as long as it does not considerably affect the measurement accuracy [1].

In this way, stress in the weld section, i.e., at points 1 to 5 as per Sec. 2.3, Fig. 5c, is measured at the BCC (3 1 0) diffraction peak, i.e., diffraction angle (2θ) of 115.1° referring to Fig. 6a. Measurement of residual stresses in the rail section at points a and b in Sec. 2.3, Fig. 5c is also conducted at the diffraction peak of BCC (3 1 0) which, based on Fig. 6b, is located at the diffraction angle of 116.2°.

$Sin^2\psi$ method is utilized for stress calculation. Starting from $\psi=0°$ and stepwise adding of five equal offsets up to $\psi=45°$, a total of six ψ points are taken into account. The assigned range of diffraction angle for the XRD measurements is $114° \leq 2\theta \leq 118°$ with a stepwise increment of 0.02, where an 0.8 second per step of counting accumulation is employed. Sliding gravity is used for the peak evaluation, and data correction for Lorentz-polarization background and absorption is undertaken.

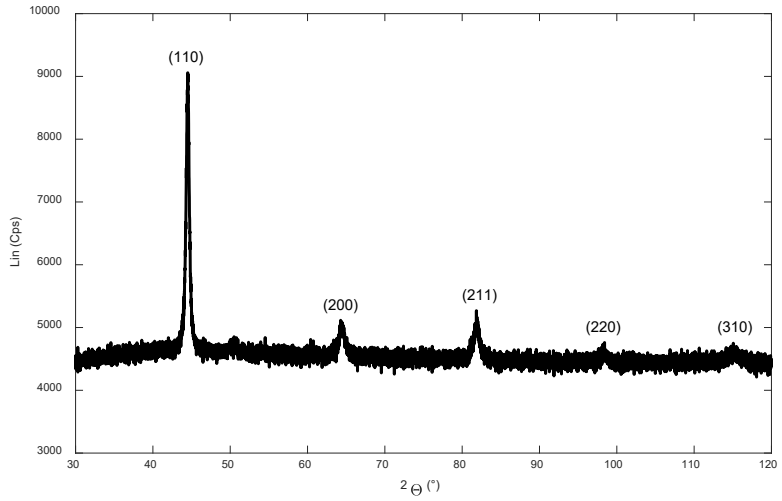

(a)

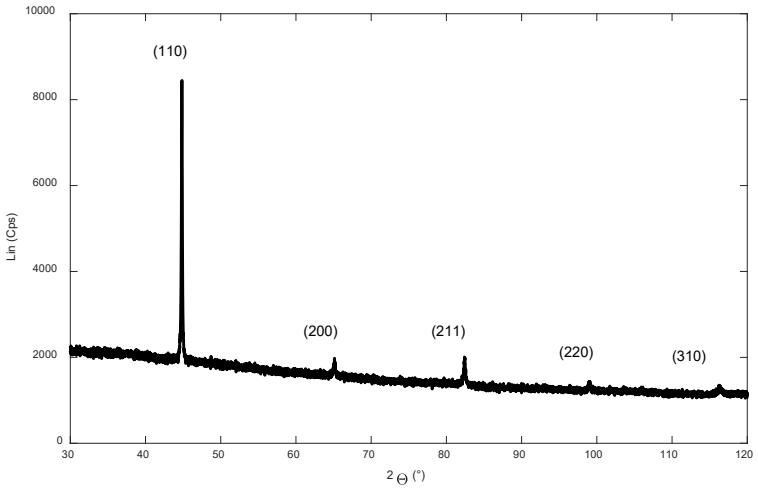

(b)

Fig. 5.6 XRD phase scan analysis at the (a) weld section, and (b) rail section of the repaired rail.

To ensure the validity of the measured residual stresses using XRD, where no additional residual stresses would affect the results, the Polished sample is etched in several steps until the measured stress is stabilized and any further layer removal would not result in any sensible changes in the measured stresses.

Per Sec. 2.3, Fig. 5c, spot 1 (shown in red) is picked as the base point at which stress measurement is performed at different stages of the specimen. The different stages of the specimen include the As-built stage (indicated as A-B in Fig. 7), Polished (indicated as P in Fig. 7), and Etched. After polishing, the sample is etched for 5 times, indicated as E-1 after first time of etching in Fig. 7, E-2 after second time of etching, and so on. The Depth parameter in Fig. 7 represents the distance of the current surface of the specimen from the base surface in the As-built condition. Polishing removed 750 μm from the As-built surface, and each step of etching removes another 50-μm layer from the specimen surface.

The measured in-plane longitudinal and transversal stresses, i.e., S_{xx} and S_{yy} (refer to Sec. 2.3, Fig. 5 to configure the x and y coordination), are shown in Figs. 7a and 7b, respectively. It is evident that polishing could cause a shifting around 45-50% in the measured stress value. The reason of such an intensive increase in the measured stress can be attributed to, first, removing the interrupting surface spikes and letting the X-ray beams to penetrate enough to the surface and measure the existing residual stresses instead of scattering around, and second, the extra residual stresses on the surface induced during the polishing process. To remove that extra portion of the residual stresses, i.e., the portion applied through polishing, the sample is etched.

Fig. 7 shows that five steps of etching could decrease the measured S_{xx} and S_{yy} by 7% and 20%, respectively. The difference between the measured stress value in the P and E-5 stages in Fig. 7 technically stands for the induced residual stresses due to polishing that are now removed in the E-5 specimen. In can be interpreted from Figs. 7a and 7b that there is no difference between the measured stress in the E-4 and E-5 stages for both the S_{xx} and S_{yy}. Hence, the E-5 specimen is used

hereafter for measuring stress at the rest of the spots shown in Sec. 2.3, Fig. 5c.

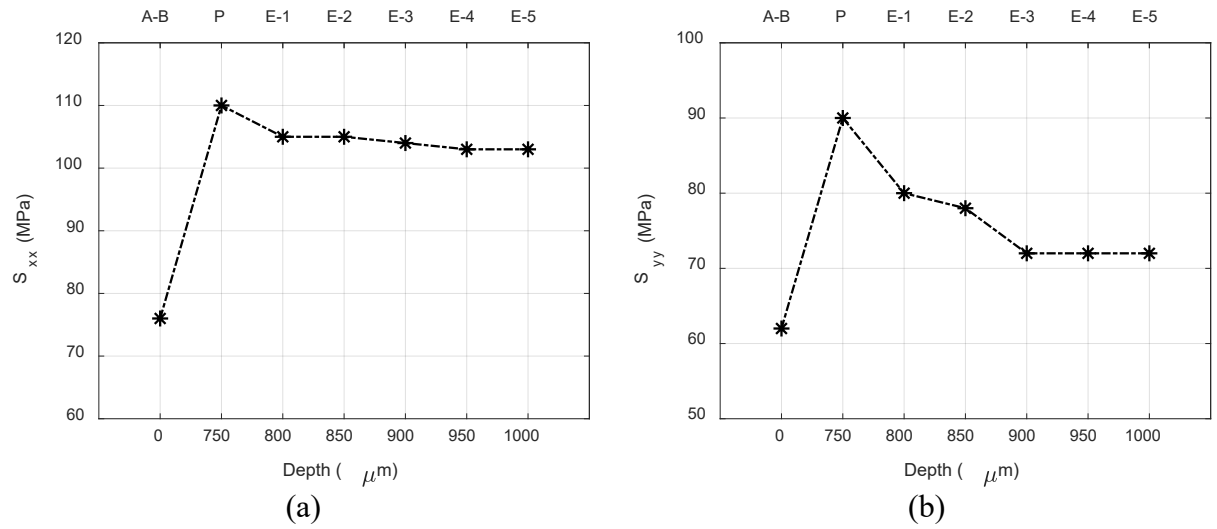

Fig. 5.7 Measured residual stresses using XRD method at spot 1 (shown in red in Sec. 2.3, Fig. 5c) along the (a) longitudinal and (b) transversal directions at different stages of the specimen; As-built (A-B), Polished (P) and first to fifth time of etching (E-1 to E-5).

Longitudinal and transversal residual stresses, i.e., S_{xx} and S_{yy}, are measured on the E-5 specimen at all the spots shown in Sec. 2.3, Fig. 5c and the results are given in Fig. 8. The lower x axis shows the distance of each spot from spot 5 (based on Sec. 2.3, Fig. 5c), and the upper x axis marks the corresponding spot number. It should be noted that spots 1 to 5 are located in the weld zone, with spot 5 the farthest and spot 1 the closest spot to the rail-weld interface, and spots a and b are in the rail zone, where spot b is the closer spot to the rail-weld interface. From the graphs shown in Fig. 8, the rail-weld interface falls somewhere between 16 to 20 mm from spot 5, i.e., between spots 1 and b.

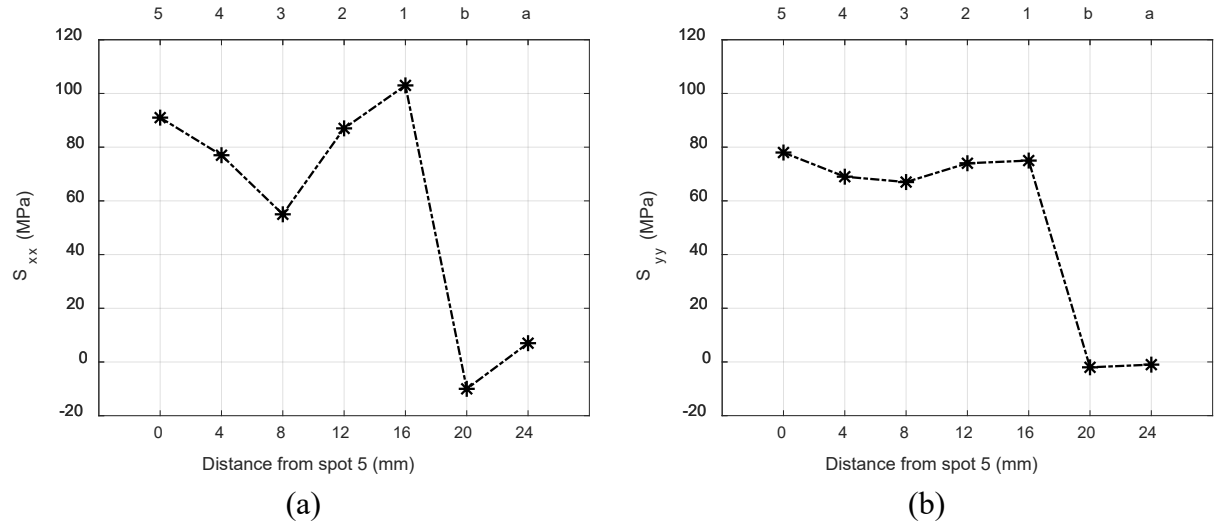

Fig. 5.8 Measured (a) longitudinal and (b) transversal residual stresses using XRD on the E-5 specimen at all the spots shown in Sec. 2.3, Fig. 5c; the upper *x* axis shows the spot numbers and the lower *x* axis shows their distance from spot 5.

According to Fig. 8a, the weld zone carries only tensile S_{xx} with the maximum values of 91 and 103 MPa located at spots 5 and 1, respectively, which represent the top surface of the weld and the area near the rail-weld interface, respectively. The minimum tensile S_{xx} of 55 MPa in the weld area is found in the middle section at spot 3. A tensile-to-compressive transition of stress happens at the rail-weld interface, i.e., from spot 1 to b, where the maximum tensile S_{xx} of 103 MPa in the weld section transforms to maximum compressive S_{xx} of 10 MPa in the rail section. It is seen that S_{xx} in the lower areas of the rail, i.e., point a, switches back to tensile, but stays at low and relatively negligible values.

Regarding the transversal stress (S_{yy}) in Fig. 8b, almost the same pattern can be figured out. The maximum tensile S_{yy} values of 78 and 75 MPa in the weld materials is found at spots 5 and 1, respectively. A compressive stress of 2 MPa is located at spot b, which is in the rail area close to the rail-weld interface. A near-zero S_{yy} happens in lower areas of the rail at spot a.

At the time of starting the SAW process, on one hand, a sudden temperature rise happens which leads to a rapid expansion of the rail surface. On the other hand, the deposited weld layer tends to shrink as a result of fast cooling through convection with the air and conduction with the bulk rail substrate. The collision of these two phenomena concludes to an applied tensile stress from rail to weld (found in spot 1 in Fig. 8) and an applied compressive stress from weld to rail (found in spot b in Fig. 8). After depositing the first weld layer, the substrate is already at a high temperature and depositing the subsequent layers will not experience a high tensile stress due to expansion-shrinkage interactions as much as the first layer did. This explains the lower tensile stresses in the middle layers, i.e., spots 2 to 4. However, the last weld layer, i.e., the top layer, cools down faster than the lower layers as a result to direct exposure to the air. Besides, unlike the lower weld layers, the top layer does not have a chance of relieving a portion of its residual stress by getting reheated owing to depositing a new layer on the top. That is why the tensile stress grows again in the upper areas of the weld, i.e., spot 5.

5.2.2. LPD-repaired heavy rail

The measured results are presented based upon the coordinate system and the assigned points shown in Sec. 2.3, Fig. 5. The XRD measurement points are illustrated in Sec. 2.3, Fig. 5c. Measurements at point 1, that is shown as a red point in Sec. 2.3, Fig. 5c, are conducted before and after every single step of sample development to ensure that the contributing errors owing to the surface roughness and externally induced residual stresses are eliminated. Stress measurement at other given points (white points in Sec. 2.3, Fig. 5c) are performed on the ultimately finished specimen, i.e., after all the polishing and chemical etching steps.

Surface roughness measurement is conducted here to ensure the measurement accuracy. However, since the results and the measurement process are quite the same as what was presented in Sec. 5.1.1, the descriptions are not repeated here.

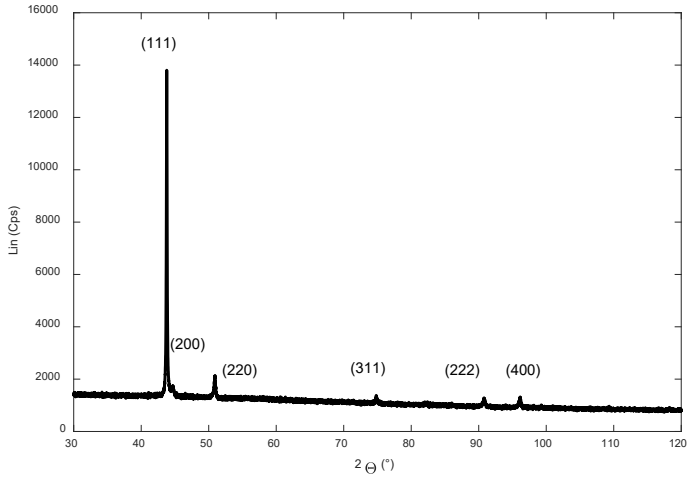

(a)

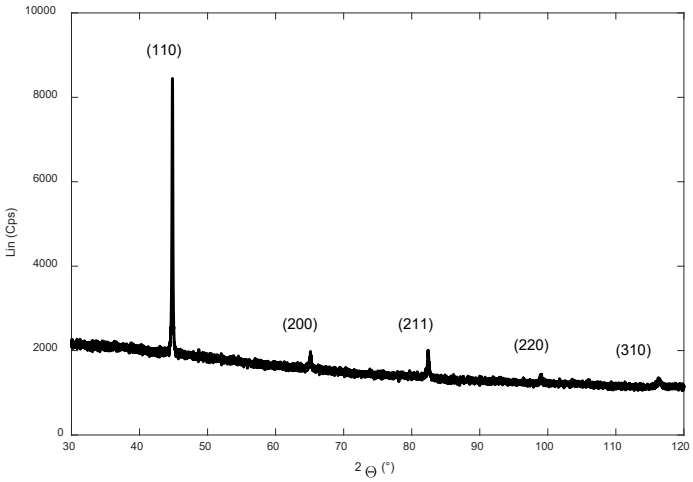

(b)

Fig. 5.9 Diffraction Peak Pattern through the full range of 2θ for (a) 304L deposition steel and (b) heavy rail.

Figs. 9a and 9b show a general phase scan analysis of the deposition and rail materials, respectively. In order to gain accurate strain values due to minor changes in lattice spacing, it is preferred to measure residual stresses at high diffraction angles to capture those slight variations [1]. Thus, XRD stress measurement at points 1, 2, 3, 4, and 5, that are located in the deposition area (see Fig. 5c), is carried out at the diffraction angle of $2\theta = 96.2°$ where, referring to Fig. 9a, FCC (4 0 0) diffraction peak occurs. Residual stresses at the rail zone, i.e., points a, b, and c in Sec. 2.3, Fig. 5c, are evaluated at the diffraction angle of $2\theta = 116.2°$ corresponding to BCC (3 1 0) peak in Fig. 9b. Stress measurement at these points is performed using $\sin^2\psi$ method. A total number of six points of ψ are employed at each measurement point, starting from $\psi = 0°$ followed by successive adding of ψ offsets up to $\psi = 45°$ with five equal intervals. The incorporated diffraction angle measurement range in the deposition area is $94.2° \leq 2\theta \leq 98.2°$ and in the rail area is $114.6° \leq 2\theta \leq 117.8°$, with a 0.02 increment of 2θ and a counting accumulation of 0.8 seconds per step. Peak evaluation is conducted using sliding gravity method, and data correction

is used for Lorentz-polarization, background, and absorption.

Measurement verification is also conducted just like what was done for the LPD-repaired light rail in Sec. 5.1.1 and hence, will not be described here again. It is just worth noting that the AE5 specimen will be used for the stress measurement.

The measured σ_{xx} and σ_{zz} stress components at different measuring locations, i.e., the depicted points in Fig. 5c, are shown in Fig. 10. All of the presented measurements are performed on the AE5 specimen. As it was mentioned earlier in Section 2.2.3, a total number of five layers are deposited on the worn head of the heavy rail. Accordingly, residual stresses at the first, second, third, fourth, and fifth deposition layers are measured by XRD profiling at points 1, 2, 3, 4, and 5 (as shown in Sec. 2.3, Fig. 5c), located at 2 mm, 6 mm, 10 mm, 14 mm, and 18 mm below the top surface of the deposition materials, respectively. Residual stress evaluation continues down to the rail zone at points c, b, and a (as shown in Sec. 2.3, Fig. 5c) that are located at 22 mm, 26 mm, and 30 mm below the top surface of the deposition materials, respectively. The measuring points along with their corresponding distance from the deposition top surface are given in Fig. 10 as the upper x-axis and lower x-axis components, respectively.

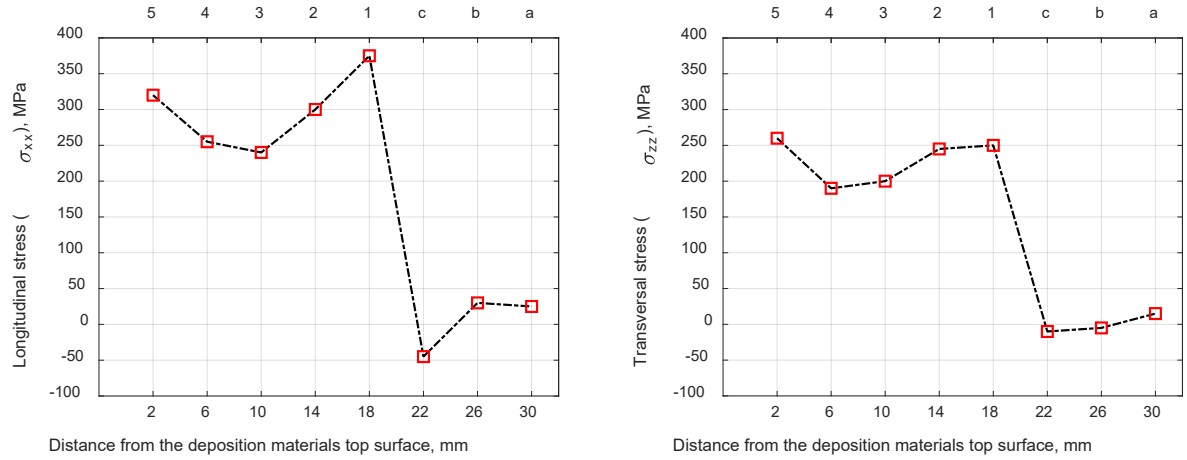

(a) (b)

Fig. 5.10 The XRD measured (a) longitudinal (σ_{xx}) and (b) transversal (σ_{zz}) residual stress distribution in the repaired rail. the upper x-axis denotes the corresponding measuring point (refer to Sec. 2.3, Fig. 5c for configuration of the points).

Regarding the longitudinal stress (σ_{xx}) distribution in Fig. 10a, the maximum tensile stress of 375 MPa occurs at the first deposition layer (point 1). The topmost deposition layer (point 5) carries the second-maximum residual stress, i.e., 320 MPa. The deposition layer carrying the minimum tensile stress of 240 MPa is the third layer (point 3). Maximum compressive stress of 45 MPa can be found in the rail zone at point c.

Speaking of the distribution of transversal residual stresses (σ_{zz}) in Fig. 10b, maximum tensile stress of 260 MPa is found at the fifth deposition layer (point 5), and the second maximum tensile of 250 MPa happens at the first deposition layer (point 1). Minimum tensile stress in the deposition zone is around 190 MPa in the fourth deposition layer (point 4). In the rail zone, the nearest point

to the rail-deposition interface (point c) carries the maximum compressive stress of 10 MPa.

According to Fig. 10, both stress components (σ_{xx} and σ_{zz}) undergo almost similar stress distribution pattern. Maximum stress values occur at the first and fifth deposition layers (points 1 and 5). The third and fourth deposition layers (points 3 and 4) contain minimum residual stresses in the deposition zone. Moving from point 1 in the deposition zone down to point c in the rail zone, the maximum tensile residual stress transforms to maximum compressive stress in the rail zone. The area between point 1 and point c, where the rail-deposition layer is also located, may be called the heat-affected zone. The maximum compressive stress takes place in point c, and then the residual stresses decay to near-zero values in points b and a.

The given residual stress distribution in Fig. 10 shows that the maximum tensile stresses happen in the first and last deposition layers, i.e., points 1 and 5, respectively. Lower tensile stresses are found at the middle layers (points 2, 3, and 4). A maximum compressive stress can be discovered in the rail zone near the rail-deposition interface (point c).

The LPD process starts with no bed preheating, meaning that the railhead as the LPD substrate is at the room temperature at the start of depositing the first deposition layer. This fact, on one hand, causes the rail to start a fast expansion during the deposition of the first layer as a result of an accelerated temperature rise, and on the other hand, makes the first deposition layer to undergo a rapid shrinkage since the rail acts as a giant, cold substrate that absorbs a large amount of the induced heat from the LPD process. Hence, the rapid expansion and shrinkage of the rail and deposition steel, respectively, along with the fact that the high-carbon rail has a higher yield strength and higher thermal expansion coefficient than the austenitic deposition materials [4,5], ultimately makes the rail to apply a high tensile stress to the deposition layer to freeze its fast shrinkage. This explains the high tensile stress at the first deposition layer (point 1). The deposition layer also applies back a minor compressive load to harness the thermal expansion of the rail. This causes a low compressive stress to be applied to the railhead, as can be seen in point c in Fig. 10.

The second layer deposits on a high-temperature bed, where the bed for this layer is the worn rail and the first layer that is already deposited. Hence, second layer will not experience a huge thermal shock as the first layer did. Also, there is not any thermal expansion and yield strength mismatch between this layer and the first deposited layer, since both of them are of the same material. These evidences, which can be given for the third and fourth layers as well, justify the lower residual stress in theses layers (points 2, 3, and 4) compared to the first layer (point 1).

The topmost deposition layer, i.e., fifth layer, will not be reheated as a result of depositing a further layer on top of it. This causes this layer to cool down much faster than the lower layers. All of the lower layers are reheated at least once as a result of depositing a new layer on the top. This reheating will cause them to cool down much slower than the top layer. Also, all of the lower layers are bounded by high-temperature materials on both sides, but the top layer is exposed to the ambient air on its upper side and starts losing heat rapidly to the environment through both convection and radiation. The other advantage of reheating for the lower layers is that it will cause a part of their residual stresses to get relieved, but the last deposition layer does not have this opportunity to relieve a part of its residual stresses. Relying on the presented reasons, the top deposition layer (point 5) has higher residual stresses than the lower layers, especially the middle

layers (points 2, 3, and 4).

The 304L stainless steel that is used as the deposition material has a room-temperature yield strength of around 215 MPa. According to Fig. 10, it is seen that almost all of the deposition layers have exceeded the material yield strength, i.e., 215 MPa. This means a great risk of early cracking and failure of the deposition steel under the dynamic load of train. In order to ease off the residual stresses, preheating the railhead before LPD repairing and also reheating the whole deposition area after LPD repairing are recommended. The pre- and post-heating methods are currently under investigation.

References for Chapter 5

[1] M.E. Fitzpatrick, A.T. Fry, P. Holdway, F.A. Kandil, J. Shackleton, L. Suominen, Determination of residual stresses by X-ray diffraction, National Physical Laboratory (2002) Measurement good practice guide no. 52.

[2] M. Ghasri-Khouzani, H. Peng, R. Rogge, R. Attardo, P. Ostiguy, J. Neidig, R. Billo, D. Hoelzle, M.R. Shankar, Experimental measurement of residual stress and distortion in additively manufactured stainless steel components with various dimensions, Mater. Sci. Eng. A 707 (2017) 689–700. https://doi.org/10.1016/j.msea.2017.09.108.

[3] V.V. Lider, X-Ray diffraction topography methods, Phys. Solid State 63 (2021) 189–214. https://doi.org/10.1016/j.msea.2017.09.108.

[4] ASM Handbook, Properties and selection: irons, steels, and high-performance alloys, in: Elevated-temperature properties of stainless steels, ASM International 1 (1990) 930-949. https://doi.org/10.31399/asm.hb.v01.a0001048.

[5] G. Li, H. Lyu, L. Huang, X. Wang, 5 - Properties of high-strength steels at and after elevated temperature, In: Behavior and design of high-strength constructional steel, Woodhead Publishing (2021) 153-204. https://doi.org/10.1016/B978-0-08-102931-2.00005-X.